2015

A novel approach for the study of near conformal theories for electroweak symmetry breaking

BOSTON UNIVERSITY

GRADUATE SCHOOL OF ARTS AND SCIENCES

Dissertation

A NOVEL APPROACH FOR THE STUDY OF NEAR CONFORMAL THEORIES FOR ELECTROWEAK SYMMETRY BREAKING

by

EVAN WEINBERG

B.S., Rensselaer Polytechnic Institute, 2011
M.S., Rensselaer Polytechnic Institute, 2012

Submitted in partial fulfillment of the
requirements for the degree of
Doctor of Philosophy
2015

Approved by

First Reader

Claudio Rebbi, Ph.D.
Professor of Physics

Second Reader

Richard Brower, Ph.D.
Professor of Physics

Acknowledgments

It is impossible to thank everyone who has supported me in the past three years while I've completed my Ph.D., but I know for sure that it was all possible because of the unconditional support I have been given. To those who I have forgotten, I am sorry, and thank you.

I would first like to thank my major advisors, Claudio Rebbi and Rich Brower, who have always guided and assisted me over the past three years. Beyond supplying a wealth of academic advice, direction, and experience, they were a pillar of support when research and my personal life sometimes became overwhelming. While the process of learning and improving never stops, I like to think I have become a better scientist over the past three years, and that is in large part because of them. I am especially grateful that I will get to continue working with them when I begin my postdoctoral position at Boston University after graduating.

Alongside my advisors, I would like to thank the entire High Energy theory group here at Boston University for their support and guidance. I am grateful to Martin Schmaltz for his personal support and for giving me a basis in modern phenomenology, Ami Katz for a never ending patience in answering questions I had while taking his quantum field theory and conformal field theory classes and for offering me the opportunity to grade said classes, Andy Cohen for many useful lunchtime conversations about new publications in the realm of not only physics, but in the news and in economics, Ken Lane for being a resource on composite theories and for offering me the opportunity to grade quantum mechanics, and a special thanks to Sheldon Glashow for offering me the opportunity to travel to Japan for the 2015 lattice conference with his own funds. Of course, it's important to not be young and alone in a physics department, and Gustavo Tavares, Yiming Xu, Michael Chernicoff, Manuel Buen Abad Najar, and Luke Pritchett have been wonderful friends in the HET department.

I would like to specially note the three members of my dissertation committee beyond

my advisors: Ami Katz, Kevin Black, and Claudio Chamon, for their time and their support of my research.

I have been grateful to in a sense have had four advisors over the course of my Ph.D. Oliver Witzel, a previous postdoctoral researcher who was at BU for the first two years of my time in the program, has always been supportive but constructively critical of the research and analysis I perform. I would also like to thank Anna Hasenfratz from the University of Colorado, Boulder, for taking a great interest in me as a student and for offering fresh ideas and ever useful guidance.

I have been lucky to not just be part of one collaboration, but two over the course of my Ph.D. work. The Lattice Strong Dynamics collaboration welcomed me early in my graduate studies, giving me the opportunity to be involved, however tangentially, in a multitude of projects over the past three years. I would especially like to give thanks to Pavlos Vranas at Lawrence Livermore National Lab for supporting two visits to the lab over the past three years, and to Enrico Rinaldi, a postdoctoral researcher at Livermore, because their efforts and support helped me write the measurement code for the 4+8 and a separate 8 flavor project.

Returning back to Boston University, I would like to thank the Physics Front Office staff for their administrative and also friendly support while in the physics department. Special thanks goes to Mirtha Cabello, Winna Sommers, and Despina Bokios.

I would like to acknowledge research funding from Rich Brower's NSF grant and the BU High Energy Theory group's DOE grant for the first and second halves of my graduate work, respectively. I also acknowledge use of computing resources at Fermilab, LLNL, and MGHPCC, which have made all of my work possible.

Of course, none of this would be possible were it not for my parents, James and Helene Weinberg. Thank you for imparting a wonderful curiosity for the world in me from a young age, supporting me all of these years, and ultimately being my number one fans. This one's for you, mom and dad.

A NOVEL APPROACH FOR THE STUDY OF NEAR CONFORMAL THEORIES FOR ELECTROWEAK SYMMETRY BREAKING

(Order No.)

EVAN WEINBERG

Boston University Graduate School of Arts and Sciences, 2015

Major Professor: Claudio Rebbi, Professor of Physics

ABSTRACT

The discovery of a light scalar at the Large Hadron Collider is in basic agreement with the predictions of an elementary Higgs in the Standard Model (SM). Nonetheless, a light, fundamental scalar is difficult to accommodate in the SM because quantum corrections suggest its mass should be much higher than the scale of electroweak symmetry breaking (EWSB). A natural possibility is to replace the Higgs by a strongly coupled composite. Composite dynamics also gives a natural explanation to the origin of EWSB.

Phenomenologically viable composite models of EWSB are constrained by experiment to feature approximate scale invariance. This behavior may follow from near conformal dynamics. At present, lattice gauge theory (LGT) provides the only quantitative method to study near conformal composite Higgs dynamics in a fully consistent strongly coupled relativistic quantum field theory.

As a novel approach to the question of finding and studying near conformal theories, I will apply LGT to the study of a generalization of Quantum ChromoDynamics (QCD) with four chiral fermion flavors plus eight flavors of finite, tunable mass. By continuously varying the mass of the eight heavy flavors, I can tune between the four flavor chirally broken theory, which exhibits features similar to QCD, and the twelve flavor theory, which is known to have a conformal fixed point. This is the "4+8 Model" for directly studying near-conformal behavior.

In this dissertation, I will review modern composite phenomenology, followed by outlining a study of the 4+8 Model over a range of heavy flavor masses. As a check of near-conformal behavior, I will measure the scale dependent coupling with the method of the Wilson Flow. After verifying the existence of controllable, approximate scale invariance, I will measure the low energy particle spectrum of the 4+8 Model. This includes a Higgs-like light composite scalar. Throughout this dissertation I will make reference to LGT measurement code I wrote and contributed to the software package FUEL.

Contents

List of Tables

List of Figures

1 Compositeness and the 4+8 Model

1.1 The Standard Model and Compositeness

With the discovery of the Higgs Boson at the Large Hadron Collider (LHC) [1, 2], the particle spectrum of the Standard Model is complete. The full picture for particle physics is not complete, however: there are several questions not answered by the Standard Model (SM) such as the origin of dark matter, neutrino masses and mixing, the flavor problem, or the matter-antimatter asymmetry in the universe [3]. Another problem faced by the Standard Model without extensions is that a theory with a self-interacting scalar is most likely not self consistent. The quadratic divergence in the mass renormalization requires a substantial fine tuning. Irrespective of the fine tunning problem, perturbative arguments based on unitarity as well as non-perturbative lattice calculations suggest that as the cutoff of the theory is removed, the self coupling of the scalar goes to zero [4, 5]. Thus, the SM must be an effective field theory description of particle physics generated out of new higher-scale dynamics. This higher-scale dynamics may also prescribe a mechanism for electroweak symmetry breaking (EWSB).

There are many models that attempt to explain the Higgs and EWSB, though the majority can be organized into three general classes: supersymmetric [6, 7], Little Higgs [8–10], and composite, which will be the focus of my dissertation. Composite dynamics is natural and appealing as it is already realized in nature. A non-relativistic example is the BCS theory of superconductivity where electrons bind to form composite bosonic Cooper pairs. These pairs can undergo Bose-Einstein condensation, leading to the phenomena of superconductivity [11]. An example of a relativistic theory is Quantum ChromoDynamics (QCD), the theory of quarks and gluons, which confines due to strong dynamics for low energies $\lesssim 1$ GeV and produces composite nucleon and pion states [12]. It is not unreasonable to assume that a new strongly coupled sector could be responsible for EWSB.

The idea of a strongly coupled composite theory as a completion for the SM had its

earliest origin as Technicolor models [13–16]. Technicolor models postulated the existence of a new strongly coupled, confining, and chiral gauge-fermion sector, with EWSB being triggered by the strong dynamics. The electroweak vacuum expectation value (vev) of the SM, denoted $v = 246$ GeV, is analogous to the expansion parameter f_π of the low energy effective theory of QCD. Further, the scale of Technicolor interactions, Λ_{TC}, is analogous to the scale of QCD interactions, Λ_{QCD}. However, in contrast with a modern composite model, many Technicolor models intentionally did not include a light scalar particle.

The discovery of the Higgs boson does not invalidate the lessons that can be learned from Technicolor models. Instead, the requirement of a light, narrow scalar adds new constraints. Any additional state predicted by the new composite dynamics must be sufficiently heavy compared to the Higgs to have escaped detection thus far at the LHC. In QCD, the lightest scalar resonance is the $\sigma(500)$, at mass of 70% of the mass of the next lightest meson, the $\rho(770)$. Further, the width of the $\sigma(500)$ is one-half its mass [17]. Both of these behaviors are in stark contrast to the measured behavior of the Higgs Boson, implying that a new strongly-coupled composite theory must be *unlike* QCD.

Our new theory also needs to satisfy existing dynamical constraints on composite models of EWSB motivated by flavor physics extensions to Technicolor known as Extended Technicolor. We need a composite theory that displays walking behavior, defined as a long intermediate range of scales where the strength of interactions is approximately constant [18]. Our theory also needs to feature a large mass anomalous dimension [19]. We will not discuss the phenomenological motivations for these constraints in this dissertation. A good review of the motivation for existing dynamical constraints can be found, for example, in [20]. The important observation is that QCD does not satisfy these constraints either.

We assert that a gauge-fermion theory unlike QCD could feature the necessary behavior. To gain qualitative information about general gauge-fermion theories, we consider the β function of the gauge coupling, g. The β function by definition describes the dependence of the gauge coupling with energy scale. At two loop order in the gauge coupling, we find [21, 22]

$$\beta(g) = \frac{dg}{d\log\mu} = -\beta_0 g^3 - \beta_1 g^5 + \mathcal{O}(g^7), \tag{1.1}$$

$$\beta_0 = \frac{1}{(4\pi)^2}\left[\frac{11}{3}C_2(A) - \frac{4}{3}T_R N_f\right], \tag{1.2}$$

$$\beta_1 = \frac{1}{(4\pi)^4}\left[\frac{34}{3}C_2(A)^2 - \frac{20}{3}C_2(A)T_R N_f - 4C_2(R)T_R N_f\right], \tag{1.3}$$

where N_c is the number of colors given by the gauge group, N_f is the number of fermions transforming under a given representation of the gauge group, T_R is the normalization of the gauge group generators, $C_2(R)$ is the quadratic Casimir for the representation of the fermions, and $C_2(A)$ is the quadratic Casimir in the adjoint representation. To simplify discussion, we will assume that our fermions transform as the fundamental representation of the gauge group, giving the result

$$\beta(g) = -\left[\frac{11}{3}N_c - \frac{2}{3}N_f\right]\frac{g^3}{(4\pi)^2} - \left[\frac{34}{3}N_c^2 - \left(\frac{13}{3}N_c - \frac{1}{N_c}\right)N_f\right]\frac{g^5}{(4\pi)^4}. \tag{1.4}$$

For a fixed but otherwise general N_c, the leading coefficient, β_0, is positive for a small number of chiral fermions. For a weak coupling constant, where we trust this perturbative result, the β function predicts that the gauge coupling goes to zero at high energies (the ultraviolet). This phenomena is known as asymptotic freedom and is essential for a self-consistent quantum field theory. For a sufficiently large number of fermions, β_0 changes sign and asymptotic freedom is lost. Without asymptotic freedom, the gauge coupling must be taken to zero as the cutoff of the theory is removed. This is identical to the situation for a self-interacting scalar.

There is an intermediate region in N_f where β_0 is positive but the second order term, β_1, is negative. Such a β function, if exact, predicts the existence of a conformal invariant fixed point at low energy (the infrared) where the gauge coupling approaches a finite value $g_*^2 = -\frac{\beta_0}{\beta_1}$ and the β function vanishes. The region of parameter space in N_f and N_c where there is an infrared fixed point in the full non-perturbative theory defines the "conformal window." The top of the conformal window, defined as the curve in N_f and N_c above

which asymptotic freedom is lost, is perturbatively well defined. In contrast, at the bottom of the conformal window perturbation theory can no longer be trusted. The transition to confining behavior can only be found as the result of a strongly coupled calculation.

It is important to know where the strongly coupled edge of the conformal window lies. A *near-conformal theory*, defined as a confining gauge-fermion theory close to the conformal window, could feature walking behavior. To find the edge of the conformal window, we must have a first principles method to solve the strongly coupled problem of discriminating conformal versus confining behavior for a general gauge-fermion theory. The leading non-perturbative method of choice is lattice gauge theory (LGT) where the continuum theory is regularized onto a finite volume four-dimensional space-time lattice with the lattice spacing, denoted a, as a UV regulator [12]. A lattice formulation of a gauge-fermion theory renders the path integral finite so it can be studied using high performance computing resources. The details of the computational study of a gauge-fermion theory with a lattice regulator is deferred to section 1.3.

LGT has many decades of success making post-dictions, and more recently predictions, about QCD [23]. More recently, it has been used in an attempt to discriminate between conformal and confining behavior in general gauge-fermion theories [24–27]. Techniques have been developed to study the scale dependence of the gauge coupling, measure the mass anomalous dimension, and investigate the low energy particle spectrum including the would-be Higgs 0^{++} state on the lattice.

The traditional, expensive approach to finding the onset of the conformal window and study near-conformal dynamics is to pick a fixed gauge group, in general $SU(N_c)$, and a given fermion representation, and explore the integer parameter space of N_f chiral fermions until hints of conformal behavior are found. This approach is filled with a myriad of issues. It is difficult to directly study a theory of massless fermions on the lattice so a small mass term is added as an infrared regulator. A theory with massive fermions by construction cannot be conformal so a careful extrapolation to the chiral limit must be performed to discriminate between confining and mass-deformed conformal behavior [28–35]. Some LGT

studies suggest that near-conformal theories may look conformal for some range of fermion masses [36, 37]. We can confidently discriminate between conformal versus non-conformal behavior only at sufficiently chiral fermion masses and large physical volumes, which can come with a prohibitively expensive cost [25].

Despite these difficulties, LGT studies have determined the fate of one theory, the $SU(2)$ gauge theory with 2 fermions transforming in the adjoint representation, to be conformal [38, 39]. Its mass anomalous dimension has also been measured [26, 40], and its spectrum has been studied in the mass-deformed regime where it features a light scalar state [26]. Unfortunately, the $SU(2)$ gauge theory with 2 adjoint fermions is not phenomenologically viable without further model-building work because it is conformal and has a rather small anomalous dimension [41].

Considerable progress has been made on other theories. There is increasing evidence for an infrared conformal fixed point (IRFP) and a light scalar in $SU(3)$ with 12 fundamental fermions [28–35]. There is also evidence for chiral symmetry breaking and a relatively low mass scalar in $SU(3)$ with 8 fundamental fermions [36] and $SU(3)$ with 2 sextet fermions [37]. The Lattice Strong Dynamics (LSD) collaboration has done considerable work studying $SU(3)$ with 8 [42] and 10 [43] fermions, as well as $SU(2)$ with 6 fermions [44]. In parallel to my dissertation work, I have been a member of the LSD collaboration and contributed to further studies $SU(3)$ 8 fermion theory. For my dissertation, however, I am only discussing work on a model that the LSD collaboration is not studying.

The lattice has shown that near-conformal theories and mass-deformed conformal theories with light scalars do exist. It is not yet known if there is a model that will satisfy all phenomenological and experimental constraints. For example, a composite theory needs to produce the correct number of Goldstone bosons to describe the $W^{\pm}$ and Z bosons, but not more. This restricts a viable theory to have exactly $N_f = 2$ chiral fermions. A theory with $N_f > 2$ fermions could still be viable, but it must feature some mechanism to decouple $N_f - 2$ fermions at energies above the EWSB scale. This gives us the correct number of Goldstone bosons and may still feature the correct near-conformal, walking dynamics if the

decoupling scale and the EWSB scale are relatively close. Unfortunately, even if a light 0^{++} exists in the full N_f chiral fermion theory, there is no *a priori* guarantee that a relatively light 0^{++} exists after decoupling.

As a backdrop to this dissertation, we pose the following question: is a light scalar a general feature of near-conformal dynamics? If so, what dynamical mechanism describes this feature? To answer this question, we need a better method to find and study near-conformal theories. In the following section, we will propose a model which takes a conformal theory with N_f fermions and decouples N_h fermions, leaving $N_\ell = N - N_h$ fermions. In light of our previous discussion, it would be ideal to leave $N_\ell = 2$ fermions. Due to our choice of a lattice fermion formulation, it is easier to use four fermions for our initial study.

As a feature of our model, we can continuously vary the range of slow running by varying the explicit scale of decoupling. In the following chapters, we will describe a non-perturbative lattice study of this model and present results on the running of the gauge coupling, as well as of the low-energy particle spectrum which we find features a light 0^{++} in correlation with the length of a slow running regime. We will conclude with remarks on future studies which can begin to probe the dynamical mechanism producing the light scalar state.

1.2 Introduction to the 4+8 Model

Traditional studies of candidates for near-conformal gauge-fermion theories focus on models with a fixed number N of degenerate, chiral fermions in a fixed representation of the gauge group $SU(N_c)$. In this study, we will take the novel approach of breaking the mass degeneracy, keeping N_ℓ fermions chiral and giving $N_h \equiv N - N_\ell$ a degenerate, finite mass which serves as a continuously tunable free parameter. N is chosen such that the $SU(N_c)$ theory with N chiral fermions is conformal, and N_ℓ is chosen such that $SU(N_c)$ with only N_ℓ chiral fermions is confining and asymptotically free. This defines the more general $N_\ell + N_h$ model.

In this dissertation, we specialize to the $SU(3)$ gauge group and the fundamental representation. We take $N = 12$, as $SU(3)$ with twelve fermions is widely believed to be

conformal, and $N_\ell = 4$, as $SU(3)$ with four fermions is known to be chirally broken and QCD-like. This gives $N_h = 8$. This gives the 4+8 model. As a remark, the choice of multiples of four fermions is not a coincidence, but a consequence of our lattice fermion discretization. This will be discussed in section 1.3.

The Lagrangian for the 4+8 model is

$$\mathcal{L} = \frac{1}{4g^2} F^a_{\mu\nu} F^a_{\mu\nu} + \sum_{i=1}^{12} \bar{\psi}_i \not{D} \psi_i + \sum_{h=1}^{8} m_h \bar{\psi}_h \psi_h, \tag{1.5}$$

where

- $\frac{1}{4g^2} F^a_{\mu\nu} F^a_{\mu\nu}$ is the Yang-Mills action density for $SU(3)$,
- $\sum_{i=1}^{12} \bar{\psi}_i \not{D} \psi_i$ is the gauge covariant kinetic term for all 12 fermion fields,
- $\sum_{h=1}^{8} m_h \bar{\psi}_h \psi_h$ is the mass term for the 8 heavy fermions.

To assist the lattice study of the 4+8 model, we add a small (relative to m_h) mass m_ℓ for the 4 light fermions and later take the light fermion chiral limit.

To understand the expected behavior as a function of m_h, we first consider two limiting behaviors. In the $m_h \to \infty$ limit, the heavy fermions decouple from the dynamics [45, 46] and we have the $SU(3)$ 4 fermion confining theory, while in the $m_h \to m_\ell \approx 0$ limit we have the $SU(3)$ 12 fermion conformal theory. In each of these limits, there are no free parameters due to the dynamics. Irrespective of the gauge coupling in the ultraviolet, the 4 fermion theory will flow to the trivial, confining fixed point in the infrared, while the 12 fermion theory will flow to the conformal infrared fixed point.

We sketch the renormalization group flow of the 4+8 model for a finite m_h in Figure 1.1. We that the mass, as a relevant parameter, will flow to infinity in the infrared for any finite bare value in the ultraviolet. For a relatively large bare value, the heavy fermions are effectively decoupled and the theory runs like the 4 fermion theory. As the bare value of m_h drops, the gauge coupling will initially be attracted to the 12 fermion infrared fixed point

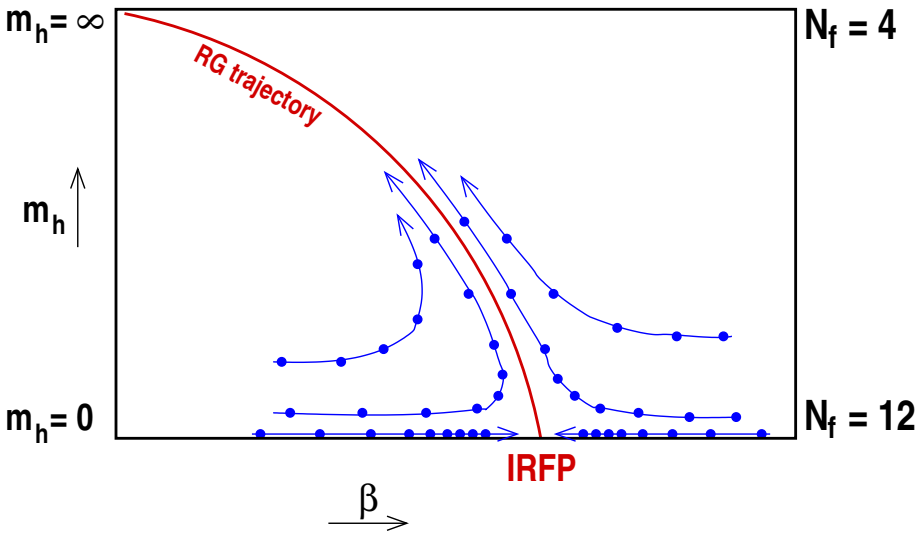

Figure 1.1. Sketch of running of the heavy mass as a function of energy scale. A sketch of the running of the heavy fermion mass and the gauge coupling as a function of energy scale, μ. We note that, for any finite value of the heavy fermion mass m_h, the theory runs to strong coupling (confinement) in the infrared.

(IRFP) before running to the confining fixed point. This period of attraction before running to confinement can become arbitrarily large as m_h continues to drop. During this period of attraction to the IRFP, the gauge coupling evolves minimally with a change of scale. This satisfies the definition of *walking behavior*. Without the free, continuous parameter m_h, there is no guarantee that we could find a theory with the phenomenologically "correct" range of walking behavior.

In its current form, the 4+8 model is not intended to be a complete theory of EWSB. For example, four chiral fermions does not produce the correct number of Goldstone bosons, and the mass anomalous dimension of the twelve fermion conformal theory is not large enough [47] to satisfy phenomenological constraints on composite EWSB. Due to the large number of fermions, we do not expect our model to satisfy experimental constraints on the S parameter [48]. These issues can be addressed by replacing the 4+8 model by a more general $N_\ell + N_h$ model. The 4+8 model serves as a testing ground to first verify that we can continuously tune the range of walking behavior, as we will discuss in chapter 2, and then study the effect of walking on the scalar spectrum, as we will discuss in chapter 4.

First, we must describe using a lattice regulator to perform non-perturbative studies of the 4+8 model.

1.3 Gauge-Fermion Theories and Lattice Studies

The most successful first principles method to non-perturbatively study a four dimensional relativistic quantum field theory is to perform a lattice study. In performing a lattice study, we reformulate a general quantum field theory as a Euclidean statistical model [49–51] and impose a regular space-time lattice as a UV regulator. These choices make our theory suitable for numerical study on high performance computing resources.

As a consequence of using a lattice regulator, the continuum action is replaced by an appropriate lattice action. The UV regulator is explicit in the lattice action as the lattice spacing a. The simplest example of imposing a lattice regulator on a continuum theory is the free scalar field. The continuum action can be written

$$\mathcal{S} = \int d^4x \frac{1}{2} \left(\partial_\mu \phi(x)\right)^2 . \tag{1.6}$$

On the other hand, the lattice action is given as

$$\mathcal{S}_{\text{lat}} = a^4 \sum_x \sum_i \frac{1}{2} \left(\frac{\phi_{x+\hat{i}} - \phi_x}{a} \right)^2 . \tag{1.7}$$

The lattice action reduces to the continuum action by taking the limit as $a \to 0$ and converting the sum to an integral by an appropriate convention. Unfortunately, naïvely writing a lattice action with the proper continuum limit does not guarantee that a study of the lattice action reproduces the correct continuum dynamics. It is more correct to study the lattice propagator (for both the free and the interacting case) and ensure it reduces properly to the continuum limit.

In the continuum, the free action gives the momentum-space propagator

$$G_F(p) = \frac{1}{\sum_i p_i^2}, \tag{1.8}$$

while the lattice regularized result is

$$G_{F,\text{lat}} = \frac{a^2}{\sum_i 4\sin^2\left(\frac{ap_i}{2}\right)}. \tag{1.9}$$

In the $a \to 0$ limit, we find

$$\lim_{a\to 0} G_{F,\text{lat}}(p) = \frac{1}{\sum_i p_i^2} + \mathcal{O}\left(a^2\right) = G_F(p). \tag{1.10}$$

The expressions for the two propagators agree. Further, the lattice propagator for a free lattice scalar corresponds to only one free scalar in the continuum. This observation can be confirmed by noting the propagator only contains one pole within the Brillouin zone $\left[-\frac{\pi}{a}, \frac{\pi}{a}\right]$. The free scalar is the unique four dimensional case where the translation between the continuum and the lattice is this simple. With this basic picture of discretization in mind, we can move on to the more subtle discretization of gauge and fermion fields.

The discretization of a gauge theory on the lattice which has informed all subsequent numerical calculations was produced by Wilson in the pioneering paper [12]. For convenience we specialize to the $SU(3)$ gauge group, though the construction generalizes to any Lie group. Gauge fields, which take values within the algebra of the $SU(3)$ group, are packaged into members of the $SU(3)$ group which live on the links connecting lattice sites. These members of the group are known as gauge links. The gauge link can be related to the continuum gauge field via with the conventional relation between the algebra and the group of

$$U_\mu(x) = e^{iaA_\mu(x)}. \tag{1.11}$$

In our convention, $U_\mu(x)$ and $A_\mu(x)$ denote a gauge link and gauge field, respectively, originating at the coordinate x and pointing in the $\hat{\mu}$ direction. In the limit as $a \to 0$, the gauge link reduces to the gauge field plus an irrelevant additive constant. Under a gauge transformation, the gauge links behave as

$$U_\mu(x) \to e^{ia\chi(x)} U_\mu(x) \left(e^{ia\chi(x+\hat{\mu})}\right)^\dagger, \tag{1.12}$$

where $\chi(x)$ is the algebra valued gauge transformation. This definition implies that gauge invariant objects are built out of closed paths of gauge links. The simplest possible closed path is a 1 by 1 square plaquette defined by

$$U^{plaq}_{\mu\nu}(x) = U_\mu(x) U_\nu(x+\hat{\mu}) U^\dagger_\mu(x-\hat{\nu}) U^\dagger_\nu(x). \tag{1.13}$$

In the continuum limit, the plaquette reduces as

$$\lim_{a\to 0} U^{plaq}_{\mu\nu}(x) \approx 1 + F^c_{\mu\nu} F^c_{\mu\nu}(x) + \mathcal{O}(a^2), \tag{1.14}$$

where the sum over color c is implicit but the sum over μ, ν is *not*. By summing over all directions and over all of space-time, we recover the continuum Yang-Mills action.

With a lattice action, we are free to choose one of many different discrete actions which reduce in the continuum limit to the correct action. For studies of near-conformal models, it is advantageous to use an improved action action containing both a fundamental and adjoint plaquette term. The bare coupling of each term is related by $\beta_a = -0.25\beta_f$, for the adjoint and fundamental terms, respectively, as a fixed convention defined in [52]. In practice, this improved action suppresses a strong coupling lattice phase transition which would otherwise interfere with studies in the strong coupling regime [29, 32, 53].

Next we discuss discretizing the fermion action. A naïve discretization of the fermion action in the spirit of Eqn. 1.6 and 1.7 will not reproduce a single fermion state in the continuum limit. Instead, each copy of the fermion action produces 2^d lattice fermions,

with d referring to the space-time dimension. This is the so-called doubling problem: in four dimensions, a single naïve fermion action gives 16 fermions in the continuum. The no-go theorem of Nielson and Ninomiya proved that it is impossible to have lattice fermions which are unitary, strictly local, satisfy a chiral symmetry on the lattice, and free of doublers [54]. Any choice of a fermion discretization must make a compromise on one or more of these properties.

In a very broad sense, there are three types of fermion discretizations:

- Wilson fermions [12], which solve the doubling problem by introducing an irrelevant term that explicitly breaks chiral symmetry but decouples all but one fermion in the continuum limit.

- Domain wall [55] or Overlap fermions [56], which satisfy a discrete lattice chiral symmetry encoded by the Ginsparg-Wilson relation [57, 58]. In the continuum limit, the Ginsparg-Wilson relation reproduces the continuum chiral symmetry. While theoretically useful, both domain wall and overlap fermions are not strictly local. As a consequence, both formulations are numerically expensive.

- Kogut-Susskind, or "staggered" fermions [59], which do not remove the doubling problem but reduce the additional fermion species to 4, not 16, for four dimensional theories. A single species of staggered fermion contains four fermion "tastes" which reduce to 4 Dirac fermions in the continuum limit. While not eliminating the doubling problem, staggered fermions are numerically inexpensive and feature an exact lattice chiral symmetry.

For this study we make use of staggered fermions. This fermion discretization is beneficial because it features an exact lattice symmetry while being numerically inexpensive compared to other discretizations.

We remark that our choice of $N_\ell = 4$ and $N_h = 8$ is motivated by our choice to use staggered fermions. In addition, we saved time starting our study of the 4+8 model by basing our non-perturbative studies on the 12 fermion work described in [32].

A classic treatment of staggered fermions can be found in [59]. In brief, staggered fermions result from an attempt to spin-diagonalize the Dirac matrix by a transformation of the form

$$\psi(x) = T(x)\chi(x), \tag{1.15}$$

$$\bar{\psi}(x) = \bar{\chi}(x)T^{\dagger}(x), \tag{1.16}$$

.

where $T(x)$ is a possibly coordinate dependent, unitary 4×4 matrix which satisfies

$$T^{\dagger}(x)\gamma_{\mu}T(x+\hat{\mu}) = \eta_{\mu}(x)\mathbb{I}, \tag{1.17}$$

where $\eta_{\mu}(x)$ is a complex number. In four dimensions, this can be achieved by

$$T(x) = \gamma_x^{x_x}\gamma_y^{x_y}\gamma_z^{x_z}\gamma_t^{x_t}, \tag{1.18}$$

where x_x, ..., x_t are integers indexing the lattice coordinates in each dimension. This definition satisfies a shift-by-two translation invariance instead of the traditional shift-by-one invariance. As a byproduct, staggered fermions distribute fermion degrees of freedom over a 2^4 hypercube of lattice sites. As a consequence of this distribution, staggered fermions have a less clean Dirac algebra structure than Wilson or domain wall fermions. It is possible to construct staggered fermions by a more *ad hoc* but perhaps intuitive prescription which, as a by product, gives a "dictionary" to convert the continuum Dirac algebra to the lattice staggered algebra. We present this derivation in appendix A.1.

Using the definition of staggered γ matrices from the appendix, we can translate the naïve action into the staggered action:

$$S = a^4 \sum_{x,\mu} \frac{1}{2a} \left(\bar{\psi}_x \gamma_\mu \psi_{x+\hat{\mu}} - \bar{\psi}_{x+\hat{\mu}} \gamma_\mu \psi_x \right) + a^4 \sum_x m \bar{\psi}_x \psi_x$$
$$\to a^4 \sum_\mu \frac{1}{2a} \sum_{x \equiv n, \alpha} \eta_\mu(x) \left[\bar{\chi}(x) \chi(x+\hat{\mu}) - \bar{\chi}(x+\hat{\mu}) \chi(x) \right] + a^4 \sum_{x \equiv n, \alpha} m \bar{\chi}(x) \chi(x). \quad (1.19)$$

The symbol η_μ absorbs the phase factors introduced by the staggered definition of the gamma matrices. Explicitly, η_μ is defined by

$$\eta_x(x) = 1 \qquad \eta_y(x) = (-1)^{x_x}$$
$$\eta_z(x) = (-1)^{x_x + x_y} \qquad \eta_t(x) = (-1)^{x_x + x_y + x_z}. \quad (1.20)$$

The naïve action and the staggered action are not equal. They feature a different continuum limit featuring a different number of states. In four dimensions, a single staggered fermion corresponds to four Dirac fermions in the continuum limit. Before taking the continuum limit, these four fermions are referred to as "tastes." In the case of the free staggered fermion, the four tastes respect an $SU(4)$ symmetry known as taste symmetry with the same algebraic structure as the Dirac spinor algebra.

As mentioned previously, staggered fermions feature an exact lattice chiral symmetry. One consequence of the exact lattice chiral symmetry is that the staggered Dirac matrix satisfies a phase hermiticity, analogous to the γ_5 hermiticity of the continuum Dirac matrix.

The free staggered action can be promoted to an interacting gauge-fermion action by replacing finite differences by covariant shifts, giving

$$S[U] = a^4 \sum_\mu \frac{1}{2a} \sum_{x \equiv n, \alpha} \eta_\mu(x) \left[\bar{\chi}(x) U_\mu(x) \chi(x+\hat{\mu}) - \bar{\chi}(x+\hat{\mu}) U_\mu^\dagger(x) \chi(x) \right]$$
$$+ a^4 \sum_{x \equiv n, \alpha} m \bar{\chi}(x) \chi(x). \quad (1.21)$$

In practice, interacting staggered fermions do not exactly respect the free field taste symmetry described above. This is because lattice gauge fields satisfy a shift-by-one translational invariance in contrast to the shift-by-two invariance of staggered fermions. The

observation that gauge fields are not smooth over the staggered fermion hypercube results in the phenomena of taste splitting, where staggered states with the same spin structure but different taste structure are not degenerate until the continuum limit is taken. We address this issue by replacing the gauge links in the staggered Dirac matrix by nHYP smeared gauge links [60]. The act of nHYP smearing smooths each gauge link with respect to its neighbors, better approximating continuous fields and reducing taste breaking effects. Smeared gauge links respect the same symmetries as the original links and therefore have a safe continuum limit.

This combined choice of gauge and fermion actions is not new but has been tested in other non-perturbative studies of near-conformal theories and has provided numerically stable simulations [32, 53]. We are now ready to discuss generating statistical ensembles of the 4+8 model for subsequent measurements.

1.4 Ensemble Generation and Measurements

We can motivate numerically sampling gauge-fermion theories agnostic to the number of fermion species or to being in the continuum or on the lattice. We begin by noting our lattice action

$$\mathcal{Z} = \int [dA_\mu d\bar{\psi}_i d\psi_i] e^{-\frac{1}{g^2}F^2 - \bar{\psi}_i \not{D} \psi_i - m_\ell \bar{\psi}_\ell \psi_\ell - m_h \bar{\psi}_h \psi_h}. \tag{1.22}$$

We cannot represent fermionic Grassmann (anti-commuting) degrees of freedom on a computer. This issue can be sidestepped by performing the Grassmann integral over the fermion degrees of freedom, giving the result

$$\mathcal{Z} = \int [dA_\mu] \det(D^\dagger D + m_h^2)^{N_h/2} \det(D^\dagger D + m_\ell^2)^{N_\ell/2} \, e^{-\frac{1}{g^2}F^2}. \tag{1.23}$$

After performing the Grassmann integral, we see that we can study the physics of our gauge-fermion system by sampling the gauge action weighted by an appropriate factor of

fermion determinants. It is still very difficult to sample the fermion determinant. Instead, we can introduce fictitious boson degrees of freedom, known as *pseudofermions*, whose path integral can be performed exactly and gives the same factors of the fermion determinant. The pseudofermion action is given by the inverse of the Dirac matrix. While there is no known method to locally sample this pseudofermion action, it is possible to perform a global evolution of the gauge and pseudofermion fields.

The preferred method to sample the non-local gauge-pseudofermion action is the Hybrid Monte Carlo (HMC) algorithm [61]. The HMC algorithm proceeds by performing a molecular dynamics evolution of the gauge and pseudofermion fields. A molecular dynamics evolution begins by introducing a partner momentum field for the gauge and pseudofermion fields according to a normal distribution. The fields and partner momenta are numerically evolved according to the Hamiltonian equations of motion along a fictitious "time" dimension for a fixed unit of time known as a molecular dynamics time unit (MDTU). At the end of this evolution, a Metropolis accept/reject step is performed which enforces detailed balance in the HMC algorithm.

As a feature of the HMC algorithm, the evolution of the gauge and pseudofermion fields does not have to be exact. In fact, inexact evolution due to numerically integrating Hamilton's equations is a feature of the HMC algorithm because it allows the overall action to fluctuate. This encodes the quantum fluctuations of our four dimensional theory into the evolution.

The numerical values of only the gauge fields are saved with a predefined frequency. We will demonstrate later that it is possible to study any quantity, gauge or fermionic, by performing measurements only against the gauge fields. Each saved set of gauge links is called a *configuration*, and a collection of configurations is known as an *ensemble*. The length of an ensemble is often quoted in units of MDTU, as noted in Table 1.1.

For numerical simulation of the 4+8 model, we perform an HMC evolution through the existing software program QHMC within the software package FUEL [62]. For numerical efficiency, we precondition the HMC evolution with a Hasenbusch mass factor [52].

After generating an ensemble, we can compute expectation values of various gauge and fermion observables. As a pure gauge example, we consider the Yang-Mills action density:

$$\begin{aligned}\langle F_{\mu\nu}F_{\mu\nu}\rangle &= \frac{1}{\mathcal{Z}}\int [dA_\mu d\bar{\psi}d\psi] F_{\mu\nu}F_{\mu\nu}\ e^{-\frac{1}{g^2}F^2 - \bar{\psi}_i \not{D}\psi_i - m_\ell \bar{\psi}_\ell \psi_\ell - m_h \bar{\psi}_h \psi_h} \\ &= \frac{1}{\mathcal{Z}}\int [dA_\mu]\ F_{\mu\nu}F_{\mu\nu}\ \det(D^\dagger D + m_h^2)^{N_h/2}\ \det(D^\dagger D + m_\ell^2)^{N_\ell/2}\ e^{-\frac{1}{g^2}F^2} \\ &= \frac{1}{\mathcal{Z}}\int [dA_\mu]\ F_{\mu\nu}F_{\mu\nu}\ W[A]. \end{aligned} \tag{1.24}$$

In going from the first line of Eqn. 1.24 to the second, we have integrated out the fermion fields. In going from the second line to the third line, we have defined a concise notation for the weight of the gauge-only path integral,

$$W[A] \equiv \det(D^\dagger D + m_h^2)^{N_h/2}\ \det(D^\dagger D + m_\ell^2)^{N_\ell/2}\ e^{-\frac{1}{g^2}F^2}. \tag{1.25}$$

The benefit of the HMC algorithm is it generates gauge fields via importance sampling. In practice, this allows us to measure an expectation value by

$$\langle F_{\mu\nu}F_{\mu\nu}\rangle_{ens} = \frac{1}{N_{cfg}}\sum_{i=1}^{N_{cfg}} \left(F_{\mu\nu}F_{\mu\nu}\right)_i, \tag{1.26}$$

where i indexes the independent configurations from 1 to N_{cfg}, the total number of configurations,[1] and $\left(F_{\mu\nu}F_{\mu\nu}\right)_i$ indicates the result of measuring the Yang-Mills action density on each configuration. We expect the result of Eqn. 1.26 to deviate from the exact answer as $\frac{1}{\sqrt{N_{cfg}}}$.

Next, we will discuss measurements of fermionic observables.[2] For simplicity, in this section we will consider Dirac fermions and defer discussion of staggered fermion observables to section 3.1. As an example, we will measure the two-point correlation function of the light

[1] Since these measurements are performed along a continuous HMC, we need to explicitly check that each measurement is independent by checking for autocorrelations. This is discussed in section 4.2.

[2] As a note, we will henceforth be dropping the subscript ℓ when referring to the light fermions. If we are considering the heavy fermions, there will still be an explicit h subscript.

flavor isomultiplet pseudoscalar bilinear, $\bar{\psi}(x)\gamma_5\lambda_i\psi(x)$. We use λ_i to denote a generalized Gell-Mann matrix for N_ℓ fermion isospin. We can compute this expectation value by

$$\begin{aligned}&\langle\bar{\psi}(0)\gamma_5\lambda_i\psi(0)\bar{\psi}(x)\gamma_5\lambda_i\psi(x)\rangle\\ =&\frac{1}{\mathcal{Z}}\int[dAd\bar{\psi}d\psi]\bar{\psi}(0)\gamma_5\lambda_i\psi(0)\ \bar{\psi}(x)\gamma_5\lambda_i\psi(x)e^{-\frac{1}{g^2}F^2-\bar{\psi}_i\not{D}\psi_i-m_\ell\bar{\psi}_\ell\psi_\ell-m_h\bar{\psi}_h\psi_h}.\end{aligned}\tag{1.27}$$

We perform the fermionic integral by enumerating all fermion contractions.

$$\begin{aligned}&\langle\bar{\psi}(0)\gamma_5\lambda_i\psi(0)\bar{\psi}(x)\gamma_5\lambda_i\psi(x)\rangle\\ =&\frac{1}{\mathcal{Z}}\int[dAd\bar{\psi}d\psi]\left\{\overbrace{\bar{\psi}(0)\gamma_5\lambda_i\underbrace{\psi(0)\ \bar{\psi}(x)}\gamma_5\lambda_i\psi}(x)-\overbrace{\bar{\psi}(0)\gamma_5\lambda_i\psi}(0)\ \overbrace{\bar{\psi}(x)\gamma_5\lambda_i\psi}(x)\right\}\times\\ &e^{-\frac{1}{g^2}F^2-\bar{\psi}_i\not{D}\psi_i-m_\ell\bar{\psi}_\ell\psi_\ell-m_h\bar{\psi}_h\psi_h}.\end{aligned}\tag{1.28}$$

There are two contractions. The first is the "quark-line connected" contraction, where each fermion is paired to an anti-fermion at a different space-time location. The second is a "quark-line disconnected" contraction, where each fermion is paired to the anti-fermion at the same location. In this case, the quark-line disconnected contraction vanishes due to the tracelessness of the isospin generators.

For notational convenience, we define the propagator from an anti-quark at location x to a quark at location y by

$$G_F(x;y)\equiv\overbrace{\bar{\psi}(x)\psi}(y),\tag{1.29}$$

where G_F is in reference to the **G**reen's function for the **f**ermion. Formally, it is the inverse of the Dirac matrix $\not{D}-m_\ell$.[3] For conciseness, we suppress all spin and color indices, and leave the dependence on gauge fields implicit.

Performing the fermion path integral, we find

[3]The heavy fermion propagator will be notated G_F^h.

$$\langle\bar{\psi}(0)\gamma_5\lambda_i\psi(0)\bar{\psi}(x)\gamma_5\lambda_i\psi(x)\rangle = \frac{1}{\mathcal{Z}}\int[dA]\ \mathrm{Tr}\left[\gamma_5\lambda_i G_F(x,0)\gamma_5\lambda_i G_F(0,x)\right] W[A]. \quad (1.30)$$

The trace refers to summing over spin, color, and isospin degrees of freedom. This expression can be simplified via the γ_5 hermiticity of the fermion propagator

$$\langle\bar{\psi}(0)\gamma_5\lambda_i\psi(0)\bar{\psi}(x)\gamma_5\lambda_i\psi(x)\rangle = \frac{1}{\mathcal{Z}}\int[dA]\ \mathrm{Tr}\left[\lambda_i\lambda_i\right]|G_F(0,x)|^2\ W[A].$$

In an abuse of notation, the magnitude squared encodes a trace over spin and color.

In general, any fermionic observable will be a function of the fermion Green's function which can be sampled against an ensemble of gauge field configurations.

The required measurements of gauge observables and fermion observables will be discussed in more depth in sections 2.3 and 3.1. These measurements are performed using the software package QHMC via code I have written myself and contributed back to the project [62]. Some measurements are performed in a separate program Qlua [63].

1.5 State of the Study: Generated 4+8 Ensembles

To perform our study of the 4+8 model, we have studied 32 different combinations of am_ℓ and am_h at several different choices of volumes for a total of 42 statistical ensembles to date. These are summarized in Figure 1.2 and Table 1.1. In all cases we use the bare gauge coupling $\beta_f = 4.0$. We use four values of am_h to monitor the effect of the heavy fermion mass on the running coupling and the light fermion spectrum. Due to difficulties studying massless fermions, we instead sample multiple values of the light fermion mass am_ℓ. As appropriate, we will later discuss taking the light fermion chiral limit.

Our studies are bounded by the onset of finite volume effects and discretization effects. For lighter values of the light fermion mass, m_ℓ, the Compton wavelength of the corresponding Goldstone boson increases, and without a sufficient lattice volume the Goldstone boson becomes squeezed. This contaminates the low energy behavior of our studies with

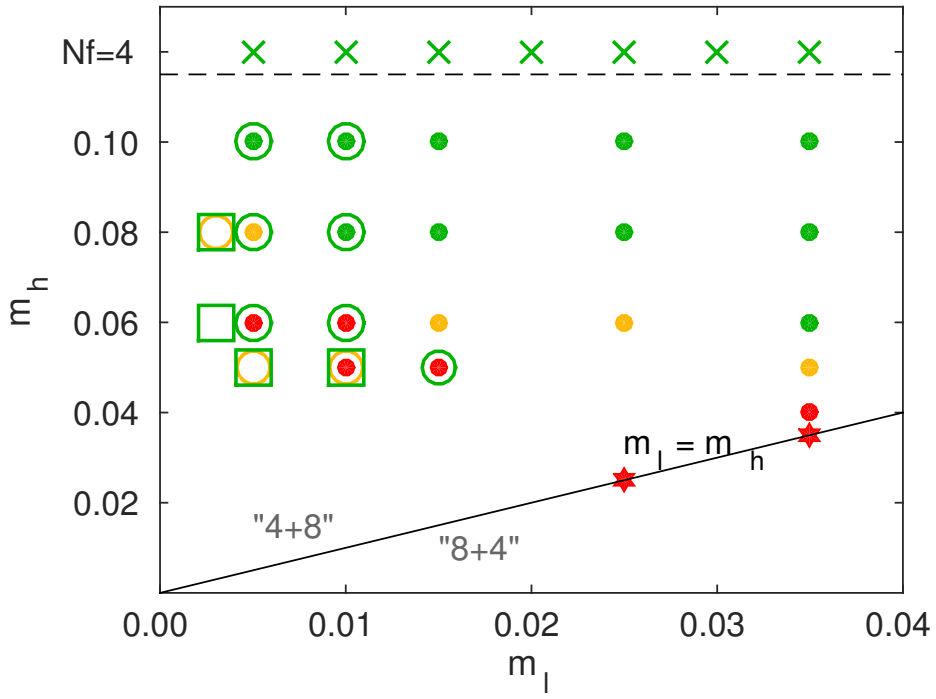

Figure 1.2. Infographic showing all ensembles studied. This infographic shows all ensembles which we have studied as part of the 4+8 model study. The shape corresponds to the volumes studied, with filled circles corresponding to $24^3 \times 48$, open circles corresponding to $32^3 \times 64$, and open squares corresponding to either $36^3 \times 64$ or $48^3 \times 96$. Exceptions to this convention are $\times$ symbols corresponding, to $24^3 \times 48$ volume 4 flavor studies of the lattice scale, and star symbols, corresponding to $24^3 \times 48$ volume 12 flavor studies. The colors are chosen to caution for finite size effects, being likely negligible for green, but more and more important as the color goes to orange then to red. Decisions on finite volume effects are made based on the Wilson flow scale, as discussed in section 2.5, or the Goldstone pion mass, as discussed in section 4.6.

finite volume effects. The only method to counteract this effect is larger lattice volumes which comes with a corresponding increase in numerical cost. The heavy fermion mass contributes to finite volume effects as well. For a fixed number of lattice sites (such as $24^3 \times 48$), the lattice spacing and therefore the physical volume shrinks as m_h shrinks. We defer an explanation of measuring the lattice spacing until section 2.5. In general, smaller values of both m_ℓ and m_h are bounded by the introduction of finite volume effects.

On the other hand, we are limited from taking am_ℓ or am_h too large due to cutoff effects. By taking am_h too large the heavy fermions decouple from the dynamics and there is little difference between studying the 4+8 model and studying the pure 4 fermion theory.

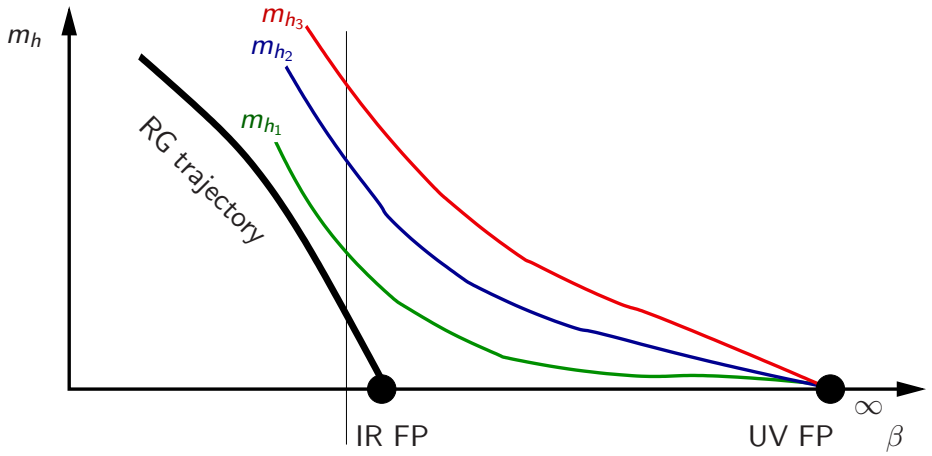

Figure 1.3. A sketch of taking the continuum limit of the 4+8 model. This sketch gives a heuristic idea of how to take the continuum limit. For a given choice of the bare coupling β, different colored curves correspond a choice of bare am_h which give equivalent infrared behavior up to lattice spacing effects. By taking $\beta \to \infty$ while $am_h \to 0$, we can take the continuum limit.

If we take m_ℓ too large, it becomes numerically difficult to extract spectral quantities as discussed in section 4.3.

It is within these bounds that we have studied the 4+8 model thus far. Before delving into the study of the gauge coupling, we will briefly digress to discuss potential future work: taking the continuum limit of the 4+8 model.

1.6 Future Work: Taking the Continuum Limit

Before discussing the continuum limit of the 4+8 model, we consider the continuum limit of the 4 fermion theory. As we will discuss in section 2.1, the continuum limit is taken by holding some physical quantity fixed while letting the lattice spacing $a \to 0$. In terms of bare parameters, this corresponds to taking the bare inverse gauge coupling β to infinity. For a sufficiently large volume, any value of β gives the correct infrared results. Even a relatively large value for β, corresponding to a small g^2 *in the ultraviolet*, will produce the correct dynamics which has g^2 run and trigger confinement in the infrared.

In the 4+8 model, the basic premise is the same, except there is one additional parameter after taking the light fermion chiral limit. This extra parameter is the heavy fermion

mass, m_h. The sketch in Figure 1.3 attempts to capture how the heavy fermion mass and the coupling renormalize together. It is important to note that both axes of the sketch correspond to bare, non-renormalized values for β and m_h.

We currently start at one β value, 4.0, indicated by the thin vertical line, and three bare heavy masses $am_h = 0.060, 0.080, 0.100$. The three curves $m_{h_1}, m_{h_2}, m_{h_3}$ schematically correspond to lines of constant physics in the parameter space of β and am_h, up to discretization effects. By knowing this curve, we could study the same IR physics at different values of the lattice spacing by studying the theory at different values of β. It would then be possible extrapolate to the continuum limit as $\beta \to \infty$.

am_h	am_ℓ	L	T	# MDTU	$M_\pi L$	$L/\sqrt{8\tilde{t}_0}$
0.050	0.005	48	96	1321	5.47	6.50
0.050	0.005	32	64	10101	3.64	4.48
0.050	0.010	48	96	1061	5.95	9.40
0.050	0.010	32	64	10051	3.93	6.30
0.050	0.010	24	48	10101	2.90	4.99
0.050	0.015	32	64	10051	4.22	7.90
0.050	0.015	24	48	10001	3.10	6.01
0.060	0.003	48	96	1381	6.03	5.22
0.060	0.005	32	64	15071	4.17	4.60
0.060	0.005	24	48	10001	3.05	3.91
0.060	0.010	32	64	15001	4.47	6.57
0.060	0.010	24	48	20001	3.36	5.03
0.060	0.015	24	48	40701	3.56	6.19
0.060	0.025	24	48	20151	3.92	8.19
0.080	0.003	36	64	20282	5.74	4.32
0.080	0.003	32	64	10051	5.12	3.88
0.080	0.005	32	64	20031	5.26	4.96
0.080	0.005	24	48	20051	3.93	3.84
0.080	0.010	32	64	10101	5.61	7.07
0.080	0.010	24	48	40021	4.20	5.34
0.080	0.015	24	48	40161	4.44	6.59
0.080	0.025	24	48	20101	4.84	8.67
0.100	0.005	32	64	1521	6.49	5.32
0.100	0.005	24	48	10051	4.86	4.04
0.100	0.010	32	64	1561	6.85	7.56
0.100	0.010	24	48	20001	5.14	5.69
0.100	0.015	24	48	10001	5.39	7.00
0.100	0.025	24	48	10101	5.88	9.15
0.040	0.035	24	48	10081	3.32	9.36
0.050	0.035	24	48	10591	3.78	9.64
0.060	0.035	24	48	10531	4.25	9.91
0.080	0.035	24	48	10201	5.23	10.45
0.100	0.035	24	48	10261	6.34	10.95

Table 1.1. An overview table listing all ensembles and finite volume effects A listing of all 4+8 model ensembles noted in Figure 1.2. The listed values for $M_\pi L$ and $L/\sqrt{8\tilde{t}_0}$ are used to quantify finite volume effects as discussed in section 4.6 and section 2.5, respectively.

2 Scale Setting and the Running Coupling

2.1 Scale Setting: Motivation

As mentioned earlier, our non-perturbative study of the 4+8 model prescribes using a finite space-time lattice as a UV regulator. As a consequence, most naïve measurements of physical quantities are contaminated by an explicit cutoff dependence. Some type of scale setting needs to be performed before taking a meaningful continuum limit.

A familiar example of scale setting is calculating one-loop scattering amplitudes in the 4 dimensional ϕ^4 theory.[1] Before scale setting, the one-loop amplitude for $\phi\phi$ scattering has an explicit cutoff dependence, and if the cutoff is removed the amplitude becomes divergent. However, by fixing the scattering amplitude to agree with an experimental result at a given scale via the counterterm prescription, this explicit cutoff dependence is removed. Most importantly, by performing this scale setting once for the $\phi\phi$ scattering amplitude, all other naïvely divergent amplitudes are consistently rendered convergent.

On the lattice, a similar process needs to occur: physical quantities need to be constructed that are independent of the lattice spacing. The measurement of a spectral quantity is a dimensionless measurement on the lattice: it is not the dimensionful mass m that is being measured, but the dimensionless combination am. This combination trivially goes to zero as the lattice spacing, a, is taken to zero. However, a ratio of masses measured on the lattice will not vanish in general as the explicit lattice spacing dependence cancels. There still remains an implicit lattice spacing dependence which can be removed by taking a continuum limit as discussed in section 1.6.

There is a question as to what physical quantity to hold fixed on the lattice. Two historically convenient choices are the string tension, which is the constant force term between a quark and an anti-quark due to confinement [64, 65], or the mass of a stable baryon mass.

For discussion, we will focus on using a baryon for scale setting. In the case of QCD, it is

[1] Of course, ignoring the fact that it suffers from the triviality problem.

common to use the mass of the Ω baryon as it is stable with respect to strong interactions and less noisy than the nucleon. The Ω has a mass of 1.672 GeV. We can use this experimental result compute the mass of other states on the lattice. For example, we can look at the ratio of the bare rho meson mass, aM_ρ, to the bare mass of the Ω baryon, aM_Ω, to predict the mass of the ρ meson.

While the string tension or the mass of a baryon have useful physical intuitions, their lattice measurements are plagued with statistical and systematic issues. Recently, the method of the Yang-Mills gradient flow, or Wilson flow, has become the method of choice. Unlike the string tension or the baryon mass, the statistical errors from the gradient flow are low and no asymptotic fits need to be performed which keeps all errors from scale setting subdominant. It is important that the errors from scale setting are small when we are comparing lattice measurements to precision measurements from experiment.

Perhaps most appealingly, the gradient flow has a formulation both in the continuum, which can be studied via perturbation theory, and on the lattice, which allows a fully non-perturbative treatment. As we will describe in subsequent sections, this makes the gradient flow suitable for scale setting and for defining a renormalized coupling. We will apply this method to the study of the running coupling of the 4+8 model. As an afterthought, the application of the Wilson flow to lattice topology will be discussed.

2.2 Continuum Definition of the Gradient Flow

In the continuum, the gradient flow of a non-Abelian Yang-Mills field $A_\mu(x)$ is defined by the flow equations [66]:

$$\begin{aligned} \partial_t B_\mu &= D_\nu G_{\mu\nu}, & B_\mu(x, t=0) &= A_\mu(x) \\ G_{\mu\nu} &= \partial_\mu B_\nu - \partial_\nu B_\mu + [B_\mu, B_\nu], & D_\mu &= \partial_\mu + [B_\mu, \cdot] \end{aligned} \tag{2.1}$$

As an important note, in the context of gradient flow the variable t has nothing to do with Euclidean time. The use of t to parameterize the length of gradient flow evolution is

a convention originating in [66].

The gradient flow continuously transforms the gauge fields at flow time $t = 0$ to a classical minimum of the Yang-Mills action in the limit as $t \to \infty$. In passing, we note that the flow time t has units of length squared. It is possible to prove that the gradient flow is also a renormalized flow that does not introduce any new divergences in the Yang-Mills theory.

At leading order in perturbation theory, the flowed fields B_μ are defined by equation (2.7) and (2.8) in [66], which can be condensed as:

$$\partial_t B_\mu(t,x) - \partial_\nu \partial_\nu B_\mu = 0. \tag{2.2}$$

In the Euclidean theory, this can be recognized as a 4+1 dimensional diffusion equation where the gradient flow time t takes the role of diffusion time. As noted in equations (2.11) and (2.12) of [66], the diffusion equation for positive times $t > 0$ can be solved by heat kernel methods in terms of the initial fields,

$$B_\mu(t,x) = \int \frac{d^4y}{(4\pi t)^2} e^{-\frac{(y-x)^2}{4t}} A_\mu(y). \tag{2.3}$$

In a qualitative sense, we can see that the gradient flow smooths the gauge field by looking at Eqn. 2.3. For small values of the flow time t, the gradient flow smooths the gauge field over local features of the original gauge field A_μ. As t increases, the gauge flow is smoothed over a larger and larger region. A useful quantification of the size of this region is the root-mean-squared radius of the heat kernel:

$$\begin{aligned} \langle r^2 \rangle &= \frac{1}{(4\pi t)^2} \int d^4y \; r^2 e^{-\frac{r^2}{4t}} \\ &= 8t \to \\ \sqrt{\langle r^2 \rangle} &= \sqrt{8t}. \end{aligned} \tag{2.4}$$

This gives a good intuition for the gradient flow: flowing the fields out to a flow time t is equivalent to smoothing the fields over a *physical distance scale* of $\sqrt{8t}$.

As an example of applying gradient flow to the continuum Yang-Mills case, [66] studies the Yang-Mills action density along the flow, defined as

$$\langle E \rangle = \frac{1}{4} G^a_{\mu\nu} G_{\mu\nu}. \tag{2.5}$$

At one-loop order, $\langle E \rangle$ can be expanded in the renormalized coupling via the $\overline{\text{MS}}$ scheme for finite Wilson flow time, given by equations (2.32) in [66] as

$$\langle E \rangle = \frac{3(N_c^2 - 1)g^2}{128\pi^2 t^2} \left\{ 1 + \bar{c}_1(t) g^2 + \mathcal{O}(g^4) \right\}, \tag{2.6}$$

where $\bar{c}_1(t)$ has a logarithmic dependence on t. We can see that $\langle E \rangle$ is a finite, *renormalized* quantity for $t > 0$. This means it can be used to set a physical scale, similar to the string tension or the baryon mass. Unlike the string tension or the baryon mass, it is convenient that $\langle E \rangle$ and its explicit t dependence are easily accessible from perturbation theory. We will return to the benefit of explicit t dependence with the discussion of the gradient flow on the lattice.

2.3 Lattice Definition of the Gradient Flow

Unlike in the continuum where there is a unique Yang-Mills action, there are many possible lattice discretizations of the Yang-Mills action that are equivalent in the continuum limit. Similarly, it is possible to define different lattice discretizations of the gradient flow from any suitable lattice action. A fully non-perturbative definition of the lattice gradient flow is given for an arbitrary gauge discretization in equation (1.4) of [66] by

$$\partial_t U_\mu(t, x) = -g_0^2 \left\{ \partial_{x,\mu} S_W(U) \right\} U_\mu(t, x), \tag{2.7}$$

where $S_W(U)$ refers to the discretized gauge action and $\partial_{x,\mu}$ refers to an $SU(3)$ Lie derivative. Both for discussion and also in implementation, we will use the simple plaquette gauge action. A more thorough overview of choices of different improved actions, as well as other choices with respect to scale setting and non-perturbative improvement, can be found in [67].

Using the plaquette action as described in section 1.3, Eqn. 2.7 can be written as

$$\begin{aligned} \partial_t U_\mu(t,x) &= X_\mu(U) U_\mu(t,x), \\ X_\mu(t,x) &= \mathcal{P}_A \left[\sum_{\pm\nu\neq\mu} U_\nu(t,x) U_\mu(t,x+\hat{\nu}) U_\nu^\dagger(t,x+\hat{\mu}) U_\mu^\dagger(t,x) \right], \end{aligned} \tag{2.8}$$

where $\mathcal{P}_A$ is the projector onto traceless, anti-Hermitian matrices (the $SU(3)$ algebra).

For any given gauge configuration, we can numerically integrate Eqn. 2.8. As outlined in Appendix C of [66], it is standard practice to integrate the flow equation with a fourth-order Runge-Kutta scheme which preserves the $SU(3)$ group structure of the gauge links, even for finite step size. The use of a fourth-order scheme ensures the discretization error from numerical integration is small. This is a first indication of how the gradient flow gives a low-error method for scale setting: the systematic error of generating the flow is by construction small, and is easy to test for and control [68].

Similar to the continuum case, gauge observables such as $\langle E \rangle$ and the topological charge can be measured along the gradient flow with a suitable lattice discretization. We use the $\mathcal{O}(a^2)$-improved clover-leaf definition proposed in [66]. A discussion of other discretizations can be found in [68].

As discussed earlier, $\langle E \rangle$ along the flow defines a renormalized quantity. At a fixed value of t, $\langle E \rangle$ defines a physical quantity at the length squared scale t, or equivalently at an energy scale

$$\mu = \frac{1}{\sqrt{8t}}. \tag{2.9}$$

We can exploit this to define a reference scale t_0 first proposed in [66] as

$$t^2 \langle E \rangle (t)\big|_{t=t_0} = 0.3, \tag{2.10}$$

where the factor of t^2 cancels the naïve scaling dependence of $\langle E \rangle$. We discuss later how the choice of 0.3 is arbitrary so long as the scale t_0 corresponds to a length scale $\sqrt{8t_0}$ sufficiently larger than the lattice spacing.

We can use the Wilson flow length scale $\sqrt{8t_0}$ to compare scales between ensembles similar to how the inverse of the Ω baryon mass can be used in QCD. In making lattice spacing dependence explicit, the bare Wilson flow length scale can be written $\sqrt{8t_0}/a$. We can form physical quantities by multiplying the bare lattice length scale with a bare mass, forming the quantity $\sqrt{8t_0}M_\bullet$. We will make large use of this construction when we compare spectrum masses between different ensembles with different values of m_ℓ and m_h in section 4.6.

2.4 Running Coupling

As an extension to its use for scale setting, the gradient flow can also be used to define a renormalized running coupling [66, 69–71]. We can define the gradient flow running coupling via

$$g^2_{GF}(\mu = \frac{1}{\sqrt{8t}}) = \frac{1}{\mathcal{N}} t^2 \langle E \rangle (t), \tag{2.11}$$

where the normalization factor $\mathcal{N} \equiv 3(N^2-1)/128\pi^2$ agrees with the leading order $\overline{\text{MS}}$ normalization for the perturbative expansion of $\langle E \rangle$ given in Eqn. 2.6 [72]. For conceptual convenience, we will discuss the running coupling in terms of the energy scale μ as defined in Eqn. 2.9. Since $\langle E \rangle$ is proportional to g^2_{GF}, we can equivalently perform scale setting via

$$g^2_{GF}(\mu)\big|_{\mu=\mu_0} = \frac{0.3}{\mathcal{N}}, \tag{2.12}$$

where the factor of $\mathcal{N}$ ensures μ_0 defined here agrees with t_0 in Eqn. 2.10.

This leads to a natural way to study the scale dependent running coupling. After fixing the running coupling at the energy scale μ_0, we can probe the value of the running coupling as a function of the relative scale μ/μ_0. Most importantly, this is a full, non-perturbative result.

This method also prescribes a way to compare the running coupling between different ensembles. This is an important goal for the 4+8 model: we argued from the RG flow in section 1.2 that we expect different running behavior as a function of different m_h values. If we define μ_0 sufficiently far in the IR, where we expect the theory to feature $SU(3)$ 4 fermion chirally broken dynamics independent of m_h, we can study how the running coupling approaches a common infrared from the ultraviolet.

Before discussing the results, we will first discuss a simple method to reduce lattice-spacing dependence of the gradient flow running coupling. This is important because, for a first study, we do not have multiple lattice spacings with which to take a continuum limit. This discussion is largely taken, with added details, from [72].

By noting that the staggered lattice action is expected to produce observables with $\mathcal{O}(a^2)$ discretization errors, we can encode the discretization errors on the gradient flow scale via

$$g^2_{GF}(\mu; a) = g^2_{GF}(\mu; a = 0) + a^2\mathcal{C} + \mathcal{O}(a^3), \tag{2.13}$$

where the term $a^2\mathcal{C}$ represents all leading order corrections. A simple method to address these leading order corrections, denoted the τ-shift, is motivated in [33] by replacing the definition of $g^2_{GF}(\mu)$ in Eqn. 2.11 with

$$\tilde{g}^2_{GF}(\mu; a) = \frac{1}{\mathcal{N}} t^2 \langle E \rangle (t + \tau_0 a^2), \tag{2.14}$$

where the value τ_0 is a small shift in the flow time. We note this correction vanishes as $a \to 0$. In the context of scale setting and the coupling, the tilde is a general convention

denoting a τ-shifted quantity. To see the utility of the τ-shift, we combine Eqn. 2.13 and 2.14 and find

$$\begin{aligned}
\tilde{g}^2_{GF}(\mu; a) &= \frac{1}{\mathcal{N}} t^2 \langle E \rangle (t + \tau_0 a^2) \\
&= \frac{t^2}{\mathcal{N}} \left(\langle E \rangle (t) + \tau_0 a^2 \frac{d \langle E \rangle}{dt}(t) + \mathcal{O}(a^4) \right) \\
&= g^2_{GF}(\mu; a) + \frac{t^2 \tau_0 a^2}{\mathcal{N}} \frac{d \langle E \rangle}{dt}(t) + \mathcal{O}(a^4) \\
&= g^2_{GF}(\mu; a = 0) + a^2 \left(\mathcal{C} + \frac{t^2 \tau_0}{\mathcal{N}} \frac{d \langle E \rangle}{dt}(t) \right) + \mathcal{O}(a^3). \qquad (2.15)
\end{aligned}$$

Looking at the last line, we see that we can cancel $\mathcal{O}(a^2)$ effects with an appropriate definition of τ_0. As a feature of the τ-shift, we can choose τ_0 without knowing $\mathcal{C}$ by considering the following observations:

- The choice of 0.3 in Eqn. 2.10 was arbitrary. We could have just as well have chosen 0.35, or other values, so long as the corresponding scale t_0 is not contaminated by cutoff effects. This defines a generalized scale

$$g^2_{GF}(\mu)\big|_{\mu=\mu_c} = \frac{c}{\mathcal{N}}, \qquad (2.16)$$

  where $c = 0.3$ coincides with the definition in Eqn. 2.12.

- We assume deviations in the running coupling for different values of m_h are cutoff effects. This is in line with our expectation that the far IR behavior of the running coupling is independent of m_h.

- In practice, it is sufficient to pick a consistent τ_0 across different ensembles with similar IR behavior [73, 74]. This avoids the problem of overfitting, i.e., letting each m_h have a unique τ_0.

These observations prescribe a method to pick a single τ_0 value which is used across all ensembles. Using the first observation, instead of only looking at $c = 0.3$, we look at both $c = 0.3$ and $c = 0.35$, with the constraint that the relative scale between the two values of c

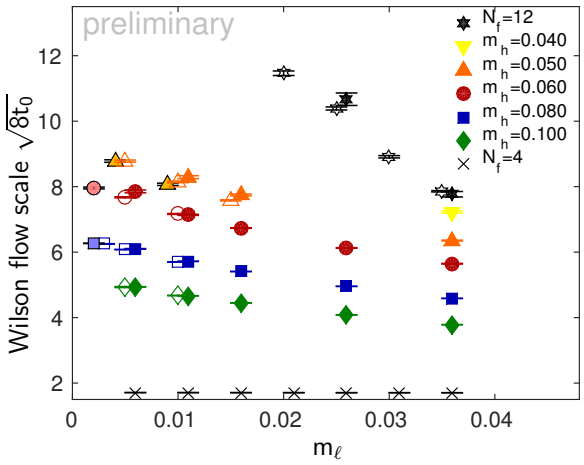

Figure 2.1. Infographic showing the gradient flow scale for all ensembles studied. The gradient flow scale $\sqrt{8\tilde{t}_0}$ for our ensembles as a function of m_ℓ. Different colors and shapes correspond to different values of the heavy fermion mass, m_h. The style of the symbol corresponds to different volumes. Filled symbols without borders correspond to 24^3 spatial volumes. Open symbols correspond to 32^3 volumes. Translucent symbols with black borders correspond to large 36^3 and 48^3 volumes.

be consistent. More specifically, we look for $t_{0.3}/t_{0.35}$ being approximately constant across all values of m_h with a *single* constant value τ_0. We refer to the τ-shift improved scale as $\sqrt{8\tilde{t}_0}$ to distinguish from the unimproved scale $\sqrt{8t_0}$.

There is more discussion to have before showing results with the τ-shift, in particular, a discussion of finite volume effects, as well as taking the $m_\ell \to 0$ limit of the scale and the running coupling before comparing m_h values.

2.5 The Gradient Flow Scale in the 4+8 Model

In Figure 2.1 we show the improved Wilson flow scale for all of our ensembles and volumes. As a reminder, one interpretation of the scale is that a larger $\sqrt{8\tilde{t}_0}$ corresponds to a smaller lattice spacing. There are multiple features and trends to discuss in this figure as a function of m_ℓ, m_h, and the volume.

In general, we see the scale increases with decreasing m_ℓ. Since we need to take the light fermion chiral limit, we only include ensembles with smaller values of m_ℓ where the linear approximation is better justified.

Next, we consider the more physically relevant m_h dependence. For the 4 fermion QCD-like ensembles ($m_h \to \infty$), the scale is roughly independent of m_ℓ. This is typical of QCD simulations where the the scale dependence with the fermion masses is very small [75].

As we lower m_h away from the decoupling limit, the scale begins to increase. The dependence on the light fermion mass also increases as we lower m_h: the effect of quark loops in the gauge field becoming more and more significant.

This culminates in the scale dependence of the mass deformed 12 fermion theory. We first remark that a scale is not meaningful in the chiral limit of a mass deformed conformal theory, by construction, though a scale can be defined away from the chiral limit. By naïve dimensional analysis, we expect the scale $\sqrt{8\tilde{t}_0}$ to diverge non-linearly as $\frac{1}{m_\ell}$.[2] This may be the source of the non-linear variation of $\sqrt{8\tilde{t}_0}$ with m_ℓ as we decrease m_h.

Last, we comment on the finite volume dependence of the Wilson flow scale. By looking at our most light fermion chiral ensembles for our smallest values of m_h, we see that finite volume effects tend to increase the measured value of the scale. As an *ad hoc* observation, values of $\sqrt{8\tilde{t}_0} \lesssim L/5$, where L is the spatial extent of the lattice, tend to be safe from finite volume effects. This bound has intuition in that the length scale defined by $\sqrt{8\tilde{t}_0}$ should be much smaller than the size of the physical volume.

As discussed earlier in section 2.1, we can form physical quantities independent of an explicit cutoff dependence via the combination $\sqrt{8\tilde{t}_0}M$, where M is a bare lattice mass. This is important in the 4+8 model because there is such a strong dependence of the lattice scale as a function of m_ℓ and m_h.

As a convention, we do not propagate errors from scale setting when we form the combination $\sqrt{8\tilde{t}_0}M$. This is for two reasons. First, the error from Wilson flow scale setting is subleading to other effects. More importantly, we are taking the value of $\sqrt{8\tilde{t}_0}$, including errors, as the *definition* of the lattice scale. In this sense, it is not meaningful for it to carry errors.

[2] Realistically, it will scale with the mass anomalous dimension of the 12 fermion theory, but the conceptual picture does not change.

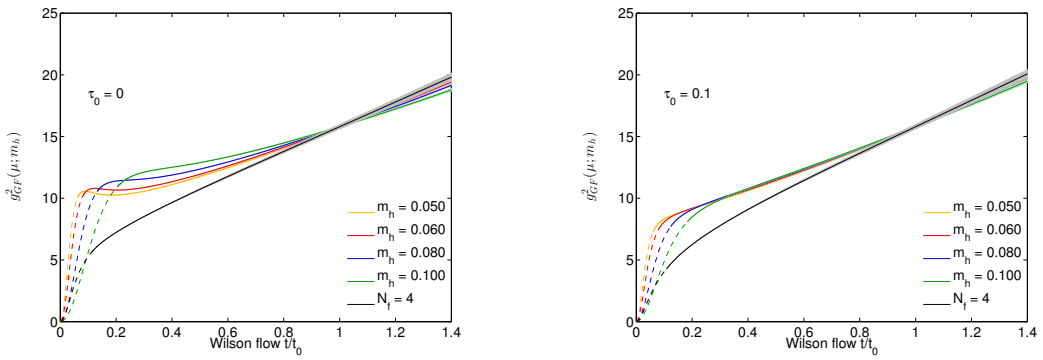

Figure 2.2. The chirally extrapolated value of $t^2 \langle E \rangle$ along the gradient flow. The chirally extrapolated value of $t^2 \langle E \rangle$ along the gradient flow for fixed m_h both without, on the left, and with, on the right, the use of the τ-shift. We note that these are measurements with error bars, however the errors on the measurement are too small to appear on the plot.

2.6 Results on the Wilson Flow Renormalized Coupling

Now that we have discussed scale setting with the Wilson flow, we are prepared to discuss studying the scale dependence of the running coupling of the 4+8 model as a function of the heavy fermion mass.

First, we need to take the light fermion chiral limit for each value of m_h. Recall that the Wilson flow is numerically integrated with respect to the Wilson flow time, t. We use a consistent step size for all ensembles and save $\langle E \rangle$ for each step. This gives us a series of values of $g^2_{GF}(\mu = \frac{1}{\sqrt{8t}}; m_h, m_\ell) = \frac{t^2 \langle E \rangle (t; m_h, m_\ell)}{\mathcal{N}}$ for each discrete value of t, m_ℓ, and m_h. We linearly extrapolate $\langle E \rangle$ in m_ℓ for each value of t and m_h to take the light fermion chiral limit, denoted $g^2_{GF}(\mu; m_h)$.

Once we have $g^2_{GF}(\mu; m_h)$, we can perform scale setting. For comparison, we show this process both with and without a τ-shift in Figure 2.2. On the left hand side, we see the renormalized coupling without a τ-shift. By construction, the different renormalized couplings agree at $t/t_0 = 1$, where t_0 is independently computed for each curve. Less encouragingly, we see that the running couplings fan out for larger values of t/t_0. This makes it difficult to argue that we have matched the different m_h theories in the infrared.

On the right hand side, we apply a small τ shift of 0.1 to each curve. In the neighborhood

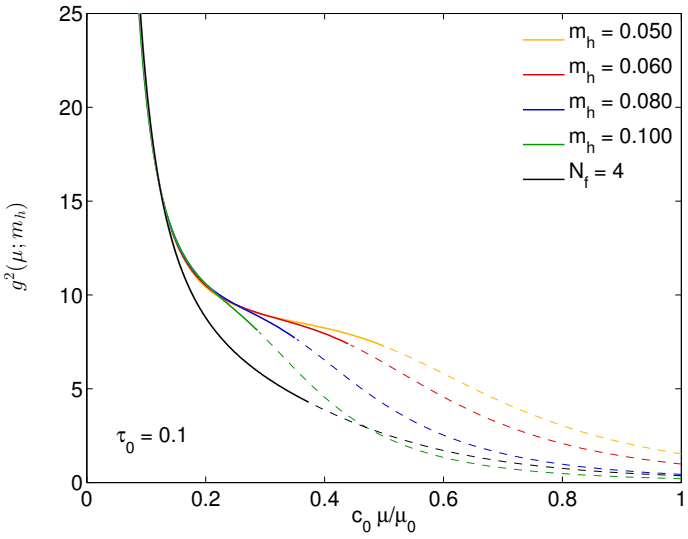

Figure 2.3. The gradient flow renormalized coupling for varying m_h with a τ-shift. The chirally extrapolated value of the Wilson flow renormalized coupling for varying m_h with the use of the τ-shift. The values of μ_0 and $c_0 = \mu_0^{-1}|_{m_h=0.060}$ serve as normalization constants that ensure that the different systems are compared at matching energy scales. The dashed lines denote where cutoff effects may be significant, as they correspond to length scales $\sqrt{8\tilde{t}}$ less than approximately two lattice spacings. We note that these are measurements with error bars, however the errors on the measurement are negligibly small.

of $t/t_0 = 1$, the curves coincide as opposed to fanning out. This is the improving feature of the τ-shift: the curves should coincide in this regime. As a reminder, this constraint is physically self consistent because due to chiral symmetry breaking, the far IR should agree independent of m_h.

For a more intuitive picture, we plot $g^2_{WF}(\mu; m_h)$ again in Figure 2.3 as a function of the normalized energy scale $\mu/\mu_0 = \sqrt{8\tilde{t}_0}/\sqrt{8\tilde{t}}$ with an additional multiplicative constant for convenience of visualization. We show only the τ shifted result using the same small shift of 0.1. There are several features to point out on this figure.

- On the left hand side of the plot, for small values of the energy scale μ, the running couplings for all values of m_h coincide by construction.
- In the limiting case of $m_h \to \infty$, the four fermion case, we see that the renormalized coupling monotonically decreases in slope for increasing energy scale. It is interesting to compare this to measurements of α_S as a function of energy scale in QCD, as

reported in Figure 6 of [76], where we notice a general qualitative similarity. This supports the conjecture that the four fermion theory is confining, asymptotically free, and devoid of any walking behavior.

- As we decrease m_h, a regime emerges where the renormalized coupling does not largely change with scale. We denote this as a shoulder of slow running. The range in μ/μ_0 of slow running increases as m_h continues to decrease. *This is the most physically interesting feature of this figure.* The renormalized coupling decreases again for larger μ. This behavior is typical of asymptotic freedom, however, we make this remark only qualitatively because these are results from length scales comparable to the lattice spacing.

- The dashed lines serve to denote where cutoff effects may become significant as they correspond to length scales $\sqrt{8\tilde{t}}$ less than two lattice spacings.

We must reiterate again the important physical result in Figure 2.3: for finite m_h, a shoulder of slow running appears in the scale dependent running coupling. As we continue to lower m_h, the length of this shoulder increases. This verifies an important conjectured feature of the 4+8 model: there exists a *continuously* tunable regime of slow running as a function of the heavy fermion mass.

As the 12 fermion theory is conformal in the chiral limit, we cannot use this scheme to define a scale dependent renormalized coupling. However, we can attempt to give a qualitative picture for how the 12 fermion gauge coupling would appear on Figure 2.3. We argued that the walking shoulder that develops is due to the 4+8 model featuring near-conformal dynamics. In this regime, we expect the running coupling to be similar to the 12 fermion fixed point coupling as sketched in Figure 1.1. Instead of turning up as μ decreases in the 4+8 model case, the 12 fermion curve would continue with a horizontal slope into the y-axis, indicative of the infrared fixed point.

We note that our running coupling plot does not give the walking coupling over multiple orders of magnitude as required in viable composite models of EWSB. This is a constraint

from computing resources: to measure slow running over many orders of magnitude in a lattice simulation, we need a lattice whose physical volume spans many orders of magnitude, which is computationally intractable. However, we find that the emergence of a small walking shoulder is an exciting proof of concept that walking behavior can be continuously controlled with the 4+8 model.

2.7 Topology

As a brief tangent before moving on to discussions on the light fermion spectrum and its dependence on walking behavior, we will discuss the topological properties of gauge-fermion theories and how to study topology with the Wilson flow.

One feature of the *classical* Yang-Mills theory is the existence of solutions known as instanton [77]. In the quantum version of the Yang-Mills theory, these solutions correspond to topological features of the background gauge field. Via the Atiyah-Singer index theorem, we can relate the number of instantons minus anti-instantons as measured through gauge observables to a fermionic measurement [78–80].

For the purpose of this dissertation, we will focus on the topology defined from pure gauge observables. In the continuum, the topological charge Q can be defined via the following integral of the topological charge density:

$$Q = \frac{g^2}{32\pi^2} \int d^4x \varepsilon_{\mu\nu\rho\sigma} F_{\mu\nu}(x) F_{\rho\sigma}(x). \tag{2.17}$$

Via the aforementioned Atiyah-Singer index theorem, the topological charge is constrained to be an integer in the continuum. On the lattice, however, we have discrete, not smooth fields. By extension, when naïvely measured, the charge when measured and summed over the lattice is not an integer but takes continuous values. It is possible to resolve an integer charge through cooling or smearing methods [81] because such methods smooth the gauge field. While there are many possible methods, all should agree in the continuum limit.

For the study of the 4+8 model, we compute the topology from the smooth fields produced by the Wilson flow [66, 82]. The topological charge operator can be built from the same field-strength tensor construction that is used to measure $\langle E \rangle$. For a minimal additional cost, we instead measure the topological charge with an $\mathcal{O}(a^4)$ improved definition of the field strength tensor as opposed to the original $\mathcal{O}(a^2)$-improved definition [83]. The improved definition features improved convergence to a unique integer along the gradient flow. By convention, we flow out to $t = L^2/32$, corresponding to a length scale $\sqrt{8t}$ of half of the spatial length of the lattice, and measure the topology. However, the exact choice is largely unimportant both on a single configuration and under an ensemble average.

The topology is also a useful indicator of the quality of an HMC evolution. To properly sample the phase space of a Yang-Mills theory, the HMC algorithm needs to "tunnel" between different topological sectors (different integer values of Q). As the lattice spacing is reduced, and by extension the gauge fields get smoother, tunneling becomes more and more difficult. This is because the instantons which correspond to the topology have a finite physical size and, in the continuum limit, are disconnected from configurations without the instanton. On the other hand, the HMC is a local algorithm which smoothly updates fields up to discretization effects and therefore struggles to create finite sized instantons.

Due to the Atiyah-Singer index theorem, near-chiral fermions can also be a problem for tunneling of topology. The index theorem shows that the topological charge is related to zero modes in the chiral Dirac operator. In reference to the definition of the weight of the path integral as defined in Eqn. 1.25, we see that a zero mode in the massless Dirac operator corresponds to a near-zero eigenvalue entering the weight in the determinant in the path integral. For topology to tunnel, the HMC needs to overcome a discontinuous change in a near-zero weighted eigenvalue in the path integral. For systems with a large number of fermions like the 4+8 model, this could in principle be difficult to achieve [43].

In alignment with these issues, the topology is a good indicator of the autocorrelation of measurements along the HMC. If the topology is largely unchanging, it is clear that the phase space of the theory is not being probed well, and as such the global autocorrelation

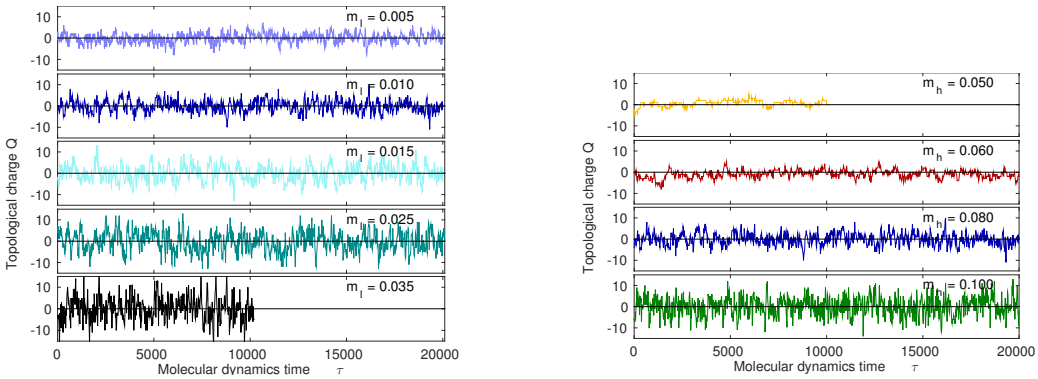

Figure 2.4. The measured topology along the HMC for varying m_ℓ and m_h. Left: The topology along the HMC for a fixed $m_h = 0.080$ and variable m_ℓ on a $24^3 \times 48$ volume. Right: The topology along the HMC for a fixed $m_\ell = 0.010$ and varying m_h on a $24^3 \times 48$ volume.

is large.

We present the value of the topology as a function of the HMC trajectory in Figure 2.4 for fixed heavy fermion mass on the left and fixed light fermion mass on the right. The following discussion of these plots will be largely qualitative.

The left hand plot, which shows the evolution of the topological charge for a fixed $m_h = 0.080$, shows the topology tunneling well along the HMC independent of the value of m_ℓ. By well, we mean that the charge is consistently fluctuating between values and crossing zero. The observation that the *amplitude* of fluctuations is larger for larger values of m_ℓ is a statement about the *width* of the distribution of the topological charge and not of its ability to fluctuate.

The right hand plot, which shows the evolution of the topological charge for a fixed $m_\ell = 0.010$, the situation as a function of the heavy fermion mass is different. For the values $m_h = 0.080, 0.100$, we see that the topology is fluctuating well. This behavior begins to change for $m_h = 0.060$, and there could be some concern on $m_h = 0.050$ where the topology stays largely positive over the range of the HMC shown. The behavior on $m_h = 0.050$ is in contrast to even $m_h = 0.060$, which fluctuates between positive and negative. For systems closer to the 12 fermion conformal theory we are beginning to see behavior reminiscent of many fermion systems.

Overall, the outlook for the topology is optimistic. The topology is not completely frozen on any ensemble. It is only at our most chiral points that we see hints of concerning behavior. This can be greatly contrasted against the behavior in [43], as an example, where topology has completely frozen. For this reason, we are not worried about the consequences of frozen topology in our current studies of the 4+8 model.

3 Spectrum Measurements

3.1 Measuring Fermion Correlation Functions: Theory

To answer some questions about the 4+8 theory, we need to look at the low lying particle spectrum. Despite looking at the Euclidean theory, it is possible to learn about the mass spectrum of the Minkowski theory by looking at Euclidean operator correlation functions.

First, we consider the Minkowski case. Recalling that the Hamiltonian is the generator of real time translations, we note

$$\begin{aligned}\langle \mathcal{O}(0)\mathcal{O}(t)\rangle &= \left\langle 0 \left| \mathcal{O}(0) e^{-iHt} \mathcal{O}(0) e^{iHt} \right| 0 \right\rangle \\ &= \left\langle 0 \left| \mathcal{O}(0) \sum_n \left(|n\rangle\, e^{-iE_n t} \langle n| \right) \mathcal{O}(0) \right| \right\rangle \\ &= \sum_{n_\mathcal{O}} |\langle 0 |\mathcal{O}| n_\mathcal{O}\rangle|^2 e^{-iE_{n_\mathcal{O}} t}, \end{aligned} \tag{3.1}$$

where n indexes all states in the theory, while $n_\mathcal{O}$ indexes all states in the theory with the same quantum numbers as $\mathcal{O}$. The expression $|\langle 0 |\mathcal{O}| n_\mathcal{O}\rangle|^2$ is related to the amplitude for creating a state with the given operator. Examples of this are given in [44, 84].

In Minkowski, this does not seem fruitful. All states are oscillatory with little hope to extract one particular state. In the Euclidean theory, the situation changes. Under a Euclidean rotation, $t \to -it$, and

$$\langle \mathcal{O}(0)\mathcal{O}(t)\rangle = \sum_{n_\mathcal{O}} |\langle 0 |\mathcal{O}| n_\mathcal{O}\rangle|^2 e^{-E_{n_\mathcal{O}} t}. \tag{3.2}$$

For a large Euclidean time separation t, the higher states become exponentially suppressed with respect to the lightest (ground) state:

$$\lim_{t\to\infty} \langle \mathcal{O}(0)\mathcal{O}(t)\rangle = |\langle 0 |\mathcal{O}| n_0\rangle|^2 e^{-E_{n_0} t} + \mathcal{O}(e^{-(E_{n_1} - E_{n_0})t}). \tag{3.3}$$

With a sufficiently large separation in t, we can isolate the lightest state for a given channel.

There is a small complicating factor with staggered fermions because the translational symmetry of the staggered action is a shift-by-two, not -one. For a given operator defined local to a specific t coordinate, known as a timeslice, there is a partner operator that differs in definition by only a phase factor $(-1)^t$ generated by the spin-taste structure $\gamma_4\gamma_5\Gamma_4\Gamma_5$. Thus, when we measure a state with general spin-taste structure $f(\gamma_i)g(\Gamma_i)$ (the "direct channel"), it also couples to partner with spin-taste structure $f(\gamma_i)\gamma_4\gamma_5 g(\Gamma_i)\Gamma_4\Gamma_5$. It is impossible to disentangle these two states in a measurement with a given operator (though it is possible to algebraically suppress one of the states, as discussed in appendix C.2). A general meson operator correlation function thus has the form

$$C_{\mathcal{O}}(t) = \left(\sum_n a_n e^{-E_n^a t}\right) + \left(\sum_n b_n (-1)^t e^{-E_n^b t}\right) \tag{3.4}$$

There is one exception to this: the spin-taste structure $\gamma_5\Gamma_5$ does not have a parity partner. This is because its parity partner, $\gamma_4\Gamma_4$, has the quantum number of the charge of the conserved staggered vector current.

As a visual example of a correlator without a parity partner versus one with a parity partner, we refer to Figure 3.1. We note these correlators are plotted on a log scale due to the assumed exponential functional form. In red, we have the $\gamma_5\Gamma_5$ state which does not feature an oscillating partner. We see that there is some curvature for smaller values of t, but for larger values of t the correlator lies on a straight line. In this regime, we argue that excited states have died out. The curvature at the center exists because, due to the periodic boundary conditions, the correlation function decays in both directions wrapping about the lattice. This gives a correlator with a hyperbolic cosine functional form.

In blue, we have the $\gamma_3\gamma_4\Gamma_1\gamma_5$ vector meson with its parity partner $\gamma_3\gamma_5\Gamma_1\Gamma_4$ axial vector meson. This correlator features an exponential decay, similar to the pseudoscalar, but also an oscillating state. Since the oscillations are more prevalent at small t, we expect the

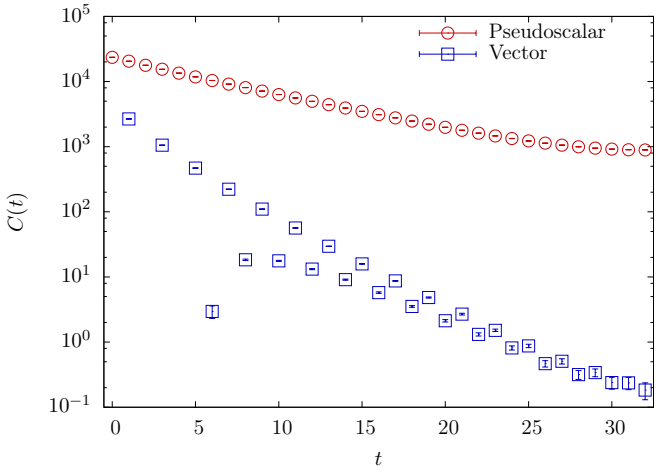

Figure 3.1. An example of a correlator with and without an oscillating term. As an example of a correlator without an oscillating term, the $\gamma_5\Gamma_5$ Goldstone pseudoscalar as measured with a wall source (see section 3.3) in red. In contrast, a correlator with an oscillating term, the $\gamma_3\gamma_4\Gamma_1\gamma_5$ vector meson with parity partner $\gamma_3\gamma_5\Gamma_1\Gamma_4$ axial vector meson, is plotted in blue. This example is from 1000 measurements on the $36^3 \times 64$, $m_\ell = 0.003$, $m_h = 0.080$ ensemble.

partner axial vector to be heavier than the vector meson. We also note that the vector meson is heavier than the Goldstone since it decays more steeply. This is reasonable: the Goldstone should be one of, if not the lightest state.

As a test case for constructing correlation functions, let us consider the Goldstone boson of staggered fermions, which has a $\gamma_5\Gamma_5$ spin-taste structure, and an isomultiplet structure. For conciseness, we will leave out the isospin generators when writing the operator. We know from our discussion in section 1.4 that when we consider the isomultiplet, the quark-line disconnected term always vanishes. We will also suppress color indices.

Using the identifications defined in section 1.3, we write

$$\begin{aligned} \mathcal{O}_\pi(x_\mu) &= \bar{\psi}(x_\mu)\gamma_5\Gamma_5\psi(x_\mu) \\ &\to \sum_\alpha \bar{\chi}(2n+\alpha)\epsilon(\alpha)\chi(2n+\alpha) \end{aligned} \tag{3.5}$$

Our operator has a definite spin-taste structure but no well defined momentum. To restrict ourselves to the zero momentum state, we sum over all hypercubes as indexed by

$\vec{n}$. This is analogous to performing a discrete Fourier transform and selecting the zero momentum piece. This gives us

$$\mathcal{O}(t)_\pi = \sum_{\vec{n}} \tilde{\mathcal{O}}_\pi(\vec{n}, t). \tag{3.6}$$

Now that we have defined our operator, we can measure the operator correlation function:

$$\begin{aligned}
\langle \mathcal{O}_\pi(0)\mathcal{O}_\pi(t)\rangle &= \frac{1}{\mathcal{Z}}\int [dA d\bar{\chi} d\chi] \left\{ \sum_{\vec{x}} \overline{\bar{\chi}(\vec{x},0)\epsilon(\vec{x},0)\,\chi(\vec{x},0)\;\underbrace{\sum_{\vec{y}} \bar{\chi}(\vec{y},t)\epsilon(\vec{y},0)\chi(\vec{y},t)}} \right\} \times \\
&\qquad e^{-S[A,\bar{\chi}_i,\chi_i]} \\
&= \frac{1}{\mathcal{Z}}\int [dA] \sum_{\vec{x}}\sum_{\vec{y}} \mathrm{Tr}\left[\epsilon(\vec{x},0) G_F(\vec{x},0;\vec{y},t)\epsilon(\vec{y},t) G_F(\vec{y},t;\vec{x},0)\right] W[A] \\
&= \frac{1}{\mathcal{Z}}\int [dA] \sum_{\vec{x}}\sum_{\vec{y}} \left|G_F(\vec{x},0;\vec{y},t)\right|^2 W[A] \\
&= \sum_{\vec{x}}\sum_{\vec{y}} \left\langle \left|G_F(\vec{x},0;\vec{y},t)\right|^2 \right\rangle_{ens}
\end{aligned} \tag{3.7}$$

To compute the zero-momentum $\gamma_5\Gamma_5$ correlation function, we measure the magnitude-squared of the fermion Green's function from all points on timeslice 0 to all points on timeslice t and then sum over all spatial coordinates.

While exact, this calculation as described is expensive. To understand where this expense comes from, we review how the Green's function is calculated.

Let us consider the fermion propagator from the origin, $(\vec{0}, 0)$, to another coordinate $(\vec{x}, t)$. This is denoted $G_F(\vec{0}, 0; \vec{x}, t)$. In the continuum, the Green's function is the inverse of the Dirac matrix in a formal, mathematical sense. On a finite lattice, this becomes an exact statement because the Dirac matrix is now a finite, sparse matrix (see Eqn. A.16, for example). To measure $G_F(\vec{0}, 0; \vec{x}, t)$, we first construct a "source" vector

$$q_p(\vec{y}, t') = \delta_{\vec{y},\vec{0}}\delta_{t',0}, \tag{3.8}$$

which is 1 at the origin and 0 elsewhere (a so-called point source), and compute the Green's function via

$$\begin{aligned} G_F(\vec{0},0;\vec{x},t) &\equiv \left(D^{staggered}\right)^{-1}(\vec{x},t;\vec{y},t')q_p(\vec{y},t') \\ &= \left(D^{staggered}\right)^{-1}(\vec{x},t;\vec{0},0'). \end{aligned} \tag{3.9}$$

As a note, when we compute the Green's function from a given source, we get the value at all other coordinate locations. Unfortunately, as noted in Eqn. 3.7, we still need to perform the inverse from all possible sources. Later, we will see there are a few potential tricks to avoid this constraint using stochastic methods. For now, though, we can make this a far less expensive prospect on the lattice by exploiting translational invariance in the ensemble average.

3.2 Measuring Fermion Correlation Functions: In Practice

In the previous subsection, we saw that to measure the zero momentum $\gamma_5\Gamma_5$ correlation function, we needed to measure the propagator from all spatial points on a timeslice. This additional volume factor makes this calculation prohibitively expensive.

To reduce this computation cost, we can take advantage of translational invariance in the ensemble average.[1] Let us start back at Eqn. 3.7 and take advantage of this.

$$\begin{aligned} \langle \mathcal{O}_\pi(0)\mathcal{O}_\pi(t)\rangle &= \sum_{\vec{x}}\sum_{\vec{y}}\left\langle |G_F(\vec{x},0;\vec{y},t)|^2\right\rangle_{ens} \\ &= \sum_{\vec{x}}\sum_{\vec{y}}\left\langle |G_F(\vec{x},0;\vec{x}+\vec{y},t)|^2\right\rangle_{ens} \\ &= V_{spatial}\sum_{\vec{y}}\left\langle \left|G_F(\vec{0},0;\vec{y},t)\right|^2\right\rangle_{ens} \end{aligned} \tag{3.10}$$

In going from the first to the second line, we took advantage of translational invariance in the sum over $\vec{y}$ to shift $\vec{y}$ to $\vec{x}+\vec{y}$. In going from the second to the third line, we

[1] Assuming we have appropriate boundary conditions—in our case, we have periodic boundary conditions in the gauge field.

used translational invariance in the sum over $\vec{x}$ to just use the value at $\vec{0}$ instead with an appropriate rescaling by the spatial volume, $V_{spatial}$.

As a note, we could have placed one operator on a general timeslice t' and the second operator on timeslice $t' + t$ to measure the same quantity. This is exploiting translational invariance in the time direction as opposed to just in the spatial direction.

By exploiting translational invariance, we have reduced our computational costs by a factor of $V_{spatial}$ matrix inversions. There are a few remarks to be made. Since we are never in the infinite ensemble limit, there is a gain from using more than one source on each configuration. This is not a free lunch: since the configurations are approximately smooth, the Green's functions $G_F(\vec{0}, 0; \vec{0}, t)$ and $G_F(\vec{0}, 1; \vec{0}, t+1)$ are correlated in noise. When two point sources are far apart, though, the Green's functions become less correlated and there is something to gain from measuring at additional source locations.

It is instructive for later discussion to understand the consequence of using a single point source to measure the Goldstone correlation function. This requires us to "work backwards": we start from Eqn. 3.10 and work back to Eqn. 3.6.

$$
\begin{aligned}
& V_{spatial} \sum_{\vec{y}} \left\langle \left| G_F(\vec{0}, 0; \vec{y}, t) \right|^2 \right\rangle_{ens} \\
=& \frac{1}{\mathcal{Z}} \int [dA] \sum_{\vec{y}} V_{spatial} \left| G_F(\vec{0}, 0; \vec{y}, t) \right|^2 W[A] \\
=& \frac{1}{\mathcal{Z}} \int [dA] \sum_{\vec{y}} V_{spatial} \mathrm{Tr} \left[G_F(\vec{0}, 0; \vec{y}, t) G_F^\dagger(\vec{0}, 0; \vec{y}, t) \right] W[A] \\
=& \frac{1}{\mathcal{Z}} \int [dA] \sum_{\vec{y}} V_{spatial} \mathrm{Tr} \left[\epsilon(\vec{0}, 0) G_F(\vec{0}, 0; \vec{y}, t) \epsilon(\vec{y}, t) G_F(\vec{y}, t; \vec{0}, 0) \right] W[A] \\
=& \frac{1}{\mathcal{Z}} \int [dA d\bar{\chi} d\chi] \left\{ V_{spatial} \overline{\bar{\chi}(\vec{0}, 0) \epsilon(\vec{0}, 0) \, \chi(\vec{0}, 0) \underbrace{\sum_{\vec{y}} \bar{\chi}(\vec{y}, t) \epsilon(\vec{y}, 0) \chi(\vec{y}, t)}} \right\} e^{-S[A, \bar{\chi}_i, \chi_i]} \\
=& \langle \left[V_{spatial} \bar{\chi}(\vec{0}, 0) \epsilon(\vec{0}, 0) \chi(\vec{0}, 0) \right] \mathcal{O}_\pi(t) \rangle
\end{aligned}
\tag{3.11}
$$

While one of the operators is the familiar zero-momentum $\gamma_5\Gamma_5$ operator at timeslice t, the operator we are correlating it with appears to not even have a well defined spin-taste

or momentum structure. Ignoring constant multiplicative factors, we isolate the left-hand operator as

$$\mathcal{O}_{gen}(0) = \bar{\chi}(\vec{0},0)\chi(\vec{0},0), \tag{3.12}$$

where *gen* refers to it being a "general" operator without well defined quantum numbers. To better understand the use of this operator, we decompose it in two steps. First, we can decompose it as

$$\begin{aligned}\mathcal{O}_{gen}(0) &= \bar{\chi}(\vec{0},0)\chi(\vec{0},0) \\ &= \frac{1}{8}\sum_{\alpha}\bar{\chi}(\alpha)\left[1+(-1)^{x}+(-1)^{x+y}+(-1)^{y}+\cdots+(-1)^{x+y+z}\right]\chi(\alpha),\end{aligned} \tag{3.13}$$

noting $\mathcal{O}_{gen}$ contains operators of all possible local spin-taste structures.

Next, we can recall results from discrete Fourier analysis to decompose $\mathcal{O}_{gen}$ into momentum states. Under a Fourier transform, an object localized at a single spatial coordinate has an equal contribution from all momentum states. Thus, $\mathcal{O}_{gen}(\vec{0},0)$ contains all possible lattice momenta—not just $\vec{p}=0$.

Combining these two decompositions, we see that $\mathcal{O}_{gen}(\vec{0},0)$ is a sum over operators with all possible lattice momenta and local spin-taste structure. By contracting it with a well-defined operator, $\mathcal{O}_{\pi}(t)$, we project out the zero-momentum $\gamma_5\Gamma_5$ state. This lends itself to an amount of efficiency: by performing a single inversion (times three colors), we can look at several different spin-taste structures as well as lattice momenta depending on what operator contraction we perform at t.

As a tangent, there is a physical interpretation to a point source as a delta function quark wavefunction ansatz in the continuum limit. After projecting onto well-defined quantum numbers, we expect our general operator to couple to any meson state containing a quark whose wavefunction is non-zero at the origin. In this regard, a more "physically shaped" source will couple better to a specific state. A discussion of state-of-the-art methods for

improved sources, with reference to older methods, can be found in [85]. For simplicity, however, we will stick with a minimal use of point sources, as well as so-called "wall sources," as discussed in the next section.

3.3 Wall Sources and Gauge Fixing

Instead of considering sources localized in position space, we can consider sources localized in momentum space at zero momentum, so called "wall sources." These measurements measure the correlation between a "wall" operator and another operator with the same quantum numbers. For example, for the $\gamma_5\Gamma_5$ spin-taste structure, the wall operator is given by:

$$\begin{aligned}\mathcal{O}_t^{wall}(x_\mu) &= \sum_{\vec{x},\vec{y}} \bar{\psi}(\vec{x},t)\gamma_5\Gamma_5\psi(\vec{y},t) \\ &\rightarrow \sum_{\vec{n},\vec{m}}\sum_{\vec{\alpha}} \bar{\chi}(2\vec{n}+\vec{\alpha})\epsilon(2\vec{n}+\vec{\alpha})\chi(2\vec{m}+\vec{\alpha}),\end{aligned} \tag{3.14}$$

where we have decomposed $\vec{x} = 2\vec{n} + \vec{\alpha}$, $\vec{y} = 2\vec{m} + \vec{\alpha}$. Its label as a zero momentum operator follows from the sum over all hypercubes $\vec{m}$ and $\vec{n}$, much in the same way Eqn. 3.6 is also zero momentum.

As written, Eqn. 3.14 is not a gauge-covariant operator. Random gauge transformations will make the non-local pieces of Eqn. 3.14 vanish because they are not covariantly connected. To address this problem, we fix the gauge links to Coulomb gauge. The wall operator is now well defined because Coulomb gauge removes all gauge freedom within each timeslice. The definition and implementation of Coulomb gauge fixing is not relevant to our discussion and is deferred to appendix B.1.

We are free to correlate the wall operator with any other operator of the same quantum numbers, for example the point operator of Eqn. 3.6

$$
\begin{aligned}
&\langle \mathcal{O}_\pi^{wall}(0)\mathcal{O}_\pi(t)\rangle \\
&= \frac{1}{\mathcal{Z}}\int [dA d\bar{\chi} d\chi]\left\{\sum_{\vec{m},\vec{n}}\sum_{\vec{\alpha}} \overline{\bar{\chi}(2\vec{n}+\vec{\alpha})\epsilon(2\vec{n}+\vec{\alpha})\,\chi(2\vec{m}+\vec{\alpha})\sum_{\vec{y}}\bar{\chi}(\vec{y},t)\epsilon(\vec{y},0)\chi(\vec{y},t)}\right\}\times \\
&\quad e^{-S[A,\bar{\chi}_i,\chi_i]} \\
&= \frac{1}{\mathcal{Z}}\int [dA]\sum_{\vec{y}}\sum_{\vec{m},\vec{n}}\sum_{\alpha}\mathrm{Tr}\left[\epsilon(2\vec{n}+\vec{\alpha},0)G_F(2\vec{n}+\vec{\alpha},0;\vec{y},t)\epsilon(\vec{y},t)G_F(\vec{y},t;2\vec{m}+\vec{\alpha},0)\right]W[A] \\
&= \frac{1}{\mathcal{Z}}\int [dA]\sum_{\vec{y}}\sum_{\vec{m},\vec{n}}\sum_{\vec{\alpha}}\mathrm{Tr}\left[G_F(2\vec{n}+\vec{\alpha},0;\vec{y},t)G_F^\dagger(2\vec{m}+\vec{\alpha},0;\vec{y},t)\right]W[A] \\
&= \sum_{\vec{y}}\sum_{\vec{m},\vec{n}}\sum_{\vec{\alpha}}\left\langle \mathrm{Tr}\left[G_F(2\vec{n}+\vec{\alpha},0;\vec{y},t)G_F^\dagger(2\vec{m}+\vec{\alpha},0;\vec{y},t)\right]\right\rangle_{ens} \\
&= \sum_{\vec{y}}\sum_{\vec{\alpha}}\left\langle \mathrm{Tr}\left[\left(\sum_{\vec{n}}G_F(2\vec{n}+\vec{\alpha},0;\vec{y},t)\right)\left(\sum_{\vec{m}}G_F^\dagger(2\vec{m}+\vec{\alpha},0;\vec{y},t)\right)\right]\right\rangle_{ens} \qquad (3.15)
\end{aligned}
$$

In practice, we measure this correlation function by first, for each corner $\vec{\alpha}$ of the hypercube, constructing a "corner" source

$$
q_w^{\vec{\alpha}}(\vec{y},t') = \sum_{\vec{\ell}}\delta_{\vec{y},2\vec{\ell}+\vec{\alpha}}\delta_{t',0}, \qquad (3.16)
$$

that is, a source with a 1 on each corner $\vec{\alpha}$ separately of every hypercube on timeslice 0. Following the definition of G_F in Eqn. 3.9, we find

$$
\begin{aligned}
\left(D^{staggered}\right)^{-1}(\vec{x},t;\vec{y},t')q_w^{\vec{\alpha}}(\vec{y},t') &= \sum_{\vec{\ell}}\left(D^{staggered}\right)^{-1}(\vec{x},t;\vec{y},t')\delta_{\vec{y},2\vec{\ell}+\vec{\alpha}}\delta_{t',0} \\
&= \sum_{\vec{\ell}}\left(D^{staggered}\right)^{-1}(\vec{x},t;2\vec{\ell}+\vec{\alpha},0) \\
&= \sum_{\vec{\ell}}G_F(2\vec{\ell}+\vec{\alpha},0;\vec{x},t). \qquad (3.17)
\end{aligned}
$$

Up to a relabeling, this reproduces the last line of Eqn. 3.15 for a given $\vec{\alpha}$. To measure the above correlation function, we need to invert the staggered Dirac matrix against a corner source for each of eight corners of the hypercube.

In practice, for quark-line connected correlation functions, we don't follow this routine for efficiency reasons. Instead, we follow the original wall source technology of [86].

To discuss this method, we construct one of two wall sources proposed, a so-called "even" wall source,[2]

$$\begin{aligned} q_w^q(\vec{y},t') &= \sum_{\vec{x}} \delta_{\vec{y},\vec{x}}\delta_{t',0}, \\ \left(D^{staggered}\right)^{-1}(\vec{x},t;\vec{y},t')q_w^q(\vec{y},t') &= \sum_{\vec{z}} G_F(\vec{z},0;\vec{x},t). \end{aligned} \tag{3.18}$$

As we did in Eqn. 3.11, we can reverse engineer what general operator this source corresponds to.

$$\begin{aligned} &\sum_{\vec{y}} \left\langle \mathrm{Tr}\left[\left(\sum_{\vec{w}} G_F(\vec{w},0;\vec{y},t)\right)\left(\sum_{\vec{x}} G_F^\dagger(\vec{x},0;\vec{y},t)\right)\right]\right\rangle_{ens} \\ =&\frac{1}{\mathcal{Z}}\int [dA]\sum_{\vec{y}}\mathrm{Tr}\left[\left(\sum_{\vec{w}} G_F(\vec{w},0;\vec{y},t)\right)\left(\sum_{\vec{x}} G_F^\dagger(\vec{x},0;\vec{y},t)\right)\right] W[A] \\ =&\frac{1}{\mathcal{Z}}\int [dA]\sum_{\vec{y}}\sum_{\vec{w},\vec{x}}\mathrm{Tr}\left[\epsilon(\vec{x},0)G_F(\vec{w},0;\vec{y},t)\epsilon(\vec{y},t)G_F(\vec{y},t;\vec{x},0)\right] W[A] \\ =&\frac{1}{\mathcal{Z}}\int [dAd\bar{\chi}d\chi]\left\{\sum_{\vec{w},\vec{x}}\overline{\bar{\chi}(\vec{x},0)\epsilon(\vec{x},0)\,\chi(\vec{w},0)\;\underbrace{\sum_{\vec{y}}\bar{\chi}(\vec{y},t)\epsilon(\vec{y},0)\chi(\vec{y},t)}}\right\} e^{-S[A,\bar{\chi}_i,\chi_i]} \\ =&\left\langle\left[\sum_{\vec{w},\vec{x}}\bar{\chi}(\vec{x},0)\epsilon(\vec{x},0)\chi(\vec{w},0)\right]\mathcal{O}_\pi(t)\right\rangle \end{aligned} \tag{3.19}$$

Similar to the definition in Eqn. 3.11, one of the operators in the correlation function is the local $\gamma_5\Gamma_5$ operator. The left hand operator, a "general" wall operator, can be decomposed into a basis with well defined quantum numbers in much the same way as in Eqn. 3.13. While we will not perform the full decomposition explicitly, one example of another state in the operator can be found by exploiting translational invariance and noting

[2] "Even" is a misnomer with respect to the idea of even and odd sites on the lattice: in this context, even refers to a full wall source without a phase, while odd refers to a full wall source with an $\epsilon(x_\mu)$ phase.

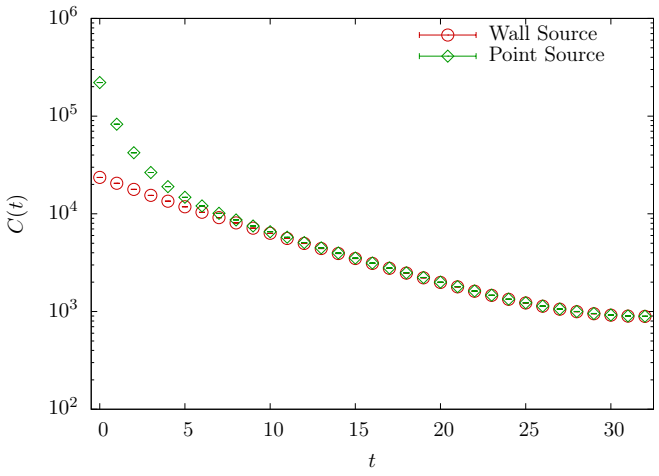

Figure 3.2. The Goldstone boson correlator from two different sources. The Goldstone boson correlator as measured using a point source, in green, and a wall source, in red. The correlators are artificially rescaled to agree at the center of the correlator at a separation $t = 32$. For smaller values of t, the values of the two correlators split, with the point source correlator having a larger magnitude than the wall source correlator. We interpret this as the point operator coupling more strongly to excited states than the wall operator. This example is from 1000 measurements on the $36^3 \times 64$, $m_\ell = 0.003$, $m_h = 0.080$ ensemble.

$$\left[\sum_{\vec{w},\vec{x}} \bar{\chi}(\vec{x},0)\epsilon(\vec{x},0)\chi(\vec{w},0)\right] = \left[\sum_{\vec{w},\vec{x}} \bar{\chi}(\vec{x},0)\epsilon(\vec{x},0)\chi(\vec{w}+\hat{x},0)\right]. \tag{3.20}$$

This new operator on the right hand side has a spin-taste structure of $\gamma_1\gamma_5\Gamma_5$, a pseudovector, which has a parity partner $\gamma_1\gamma_4\Gamma_4$, a vector meson. By modifying the sum over $\vec{y}$ at the start of Eqn. 3.19, it is possible to measure many different correlation functions without performing additional numerical inverses.

The method of wall sources as outlined in [86] constitutes the majority of quark-line connected measurements we perform. In practice, measurements from wall sources have reduced couplings to excited states when compared with measurements from point sources as described in section 3.2. As a example of this, we refer to Figure 3.2 where we show the $\gamma_5\Gamma_5$ pseudoscalar meson measured using a point source and a wall source, normalized such that the value of the correlator at the center ($t = T/2 = 32$) is equal for both correlators. Away from the center, the point source correlator raises higher than the wall source correlator.

Since both correlators couple to the same ground state, any deviation is attributed to excited state contaminations.

As a remark, a full list of all states measured in FUEL can be found in appendix B.2.

3.4 Stochastic Sources

There are some situations where exploiting translational invariance in the ensemble average breaks down, in general because the fluctuations within a single configuration are too large. An example is measuring the expectation value of the light fermion chiral condensate, defined by

$$\mathcal{O}_{pbp} = \frac{1}{V}\sum_{x_\mu} \bar{\psi}(x_\mu)\psi(x_\mu) \rightarrow \frac{1}{V}\sum_{x_\mu} \bar{\chi}(x_\mu)\chi(x_\mu). \tag{3.21}$$

The chiral condensate is interesting to look at for a wide variety of reasons. In the chiral limit, it is an order parameter for spontaneous chiral symmetry breaking. Away from the chiral limit, it appears in the GMOR relation, relating the Goldstone boson mass to the fermion mass at finite values of the fermion mass [87]. It can also be used in the hunt for the onset of near-conformal behavior via chiral enhancement [88]. For the purpose of HMC evolution, it is a useful indicator of long-range autocorrelation along the HMC due to its non-local behavior, similar to the topological charge as discussed in section 2.7.

To measure the chiral condensate on the lattice, we compute the following expectation value:

$$\begin{aligned}
\langle \mathcal{O}_{pbp} \rangle &= \frac{1}{\mathcal{Z}} \int [dA d\bar{\chi} d\chi] \left\{ \frac{1}{V} \sum_{x_\mu} \overline{\bar{\chi}(x_\mu)\chi(x_\mu)} \right\} e^{-S[A,\bar{\chi}_i,\chi_i]} \\
&= \frac{1}{\mathcal{Z}} \int [dA] \frac{1}{V} \sum_{x_\mu} \mathrm{Tr}\left[G_F(x_\mu; x_\mu)\right] W[A] \\
&= \frac{1}{V} \sum_{x_\mu} \langle \mathrm{Tr}\left[G_F(x_\mu; x_\mu)\right] \rangle_{ens} \,.
\end{aligned} \tag{3.22}$$

Measuring the chiral condensate is equivalent to averaging the point-to-self Green's function over the lattice. Unlike with the pseudoscalar two-point function, measuring the chiral condensate at a single point and invoking translational invariance over the full ensemble is not sufficient to achieve an accurate answer in practice. It is also infeasible to compute the Green's function at each point on the lattice.

It is possible to achieve a good compromise with stochastic methods. Recalling that the Green's function is the numerical inverse of the staggered Dirac matrix, we can approach stochastic estimators as follows:

Consider a complex matrix $S(x, y)$, where x and y index rows and columns, respectively. We can construct a set of noise vectors, $\eta_{[i]}(x)$, satisfying

$$\lim_{N_i \to \infty} \frac{1}{N_i} \sum_{i=1}^{N_i} \eta_{[i]}(x) \eta^{\dagger}_{[i]}(y) = \mathbf{I}(x, y), \tag{3.23}$$

where $\mathbf{I}(x, y)$ is the identity matrix. The vectors $\eta_{[i]}(x)$ can be pulled from a $U(1)$, $\mathbb{Z}_2$, or normal distribution, for example. For each $\eta_{[i]}(x)$, we define the vector $\phi_{[i]}(x)$ by

$$\phi_{[i]}(x) = S^{-1}(x, y) \eta_{[i]}(y). \tag{3.24}$$

A stochastic estimation of the inverse of the matrix $S(x, y)$ is given by

$$\begin{aligned}
\lim_{N_i \to \infty} \frac{1}{N_i} \sum_{i=1}^{N_i} \eta^{\dagger}_{[i]}(y) \phi_{[i]}(x) &= \lim_{N_i \to \infty} \frac{1}{N_i} \sum_{i=1}^{N_i} \eta^{\dagger}_{[i]}(y) S^{-1}(x, z) \eta_{[i]}(z) \\
&= \lim_{N_i \to \infty} \frac{1}{N_i} \sum_{i=1}^{N_i} S^{-1}(x, z) \eta_{[i]}(z) \eta^{\dagger}_{[i]}(y) \\
&= S^{-1}(x, z) \left[\lim_{N_i \to \infty} \frac{1}{N_i} \sum_{i=1}^{N_i} \eta_{[i]}(z) \eta^{\dagger}_{[i]}(y) \right] \\
&= S^{-1}(x, z) \mathbf{I}(z, y) \\
&= S^{-1}(x, y).
\end{aligned} \tag{3.25}$$

For finite N_i, the error of this approximation goes as $\frac{1}{\sqrt{N_i}}$.

This method can be translated into the language of sources and Green's functions. Consider a set of sources defined

$$q_{[i]}(\vec{y},t') = \sum_{\vec{z},t''} \delta_{\vec{y},\vec{z}}\delta_{t',t''}\eta_{[i]}(\vec{z},t''), \tag{3.26}$$

where $\eta_{[i]}(\vec{z},t'')$ satisfy Eqn. 3.23. We define

$$\begin{aligned}\left(D^{staggered}\right)^{-1}(\vec{x},t;\vec{y},t)q_{[i]}(\vec{y},t') &= \sum_{\vec{z},t''} G_F(\vec{z},t'';\vec{x},t)\eta_{[i]}(\vec{z},t'') \\ &\equiv \phi_{[i]}(\vec{x},t).\end{aligned} \tag{3.27}$$

In terms of Eqn. 3.26 and 3.27, we can perform a stochastic measurement of the chiral condensate by

$$\begin{aligned}&\lim_{N_i\to\infty}\frac{1}{N_i}\sum_{i=1}^{N_i}\left\langle \mathrm{Tr}\left[\frac{1}{V}\sum_{x_\mu}\eta^\dagger_{[i]}(x_\mu)\phi_{[i]}(x_\mu)\right]\right\rangle_{ens} \\ =&\lim_{N_i\to\infty}\frac{1}{N_i}\sum_{i=1}^{N_i}\left\langle \mathrm{Tr}\left[\frac{1}{V}\sum_{x_\mu}\eta^\dagger_{[i]}(x_\mu)\left(\sum_{z_\mu}G_F(z_\mu;x_\mu)\eta_{[i]}(z_\mu)\right)\right]\right\rangle_{ens} \\ =&\left\langle \mathrm{Tr}\left[\frac{1}{V}\sum_{x_\mu,z_\mu}\left(\lim_{N_i\to\infty}\frac{1}{N_i}\sum_{i=1}^{N_i}\eta_{[i]}(z_\mu)\eta^\dagger_{[i]}(x_\mu)\right)G_F(z_\mu;x_\mu)\right]\right\rangle_{ens} \\ =&\left\langle \mathrm{Tr}\left[\frac{1}{V}\sum_{x_\mu,z_\mu}\delta_{x_\mu,z_\mu}G_F(z_\mu;x_\mu)\right]\right\rangle_{ens} \\ =&\left\langle \mathrm{Tr}\left[\frac{1}{V}\sum_{x_\mu}G_F(x_\mu;x_\mu)\right]\right\rangle_{ens} \\ =&\frac{1}{\mathcal{Z}}\int[dA]\frac{1}{V}\sum_{x_\mu}\mathrm{Tr}\left[G_F(x_\mu;x_\mu)\right]W[A] \\ =&\frac{1}{\mathcal{Z}}\int[dAd\bar{\psi}d\psi]\left\{\frac{1}{V}\sum_{x_\mu}\overline{\bar{\chi}(x_\mu)\chi}(x_\mu)\right\}e^{-S[A,\bar{\psi}_i,\psi_i]} \\ =&\left\langle\mathcal{O}_{pbp}\right\rangle.\end{aligned} \tag{3.28}$$

Again, for finite N_i, the deviations from the infinite stochastic limit are expected to go as $\frac{1}{\sqrt{N_i}}$. As a remark, there is an improved estimator for the chiral condensate, featuring less stochastic noise for finite N_i. Discussion of this is deferred to the following section.

For reasons of notational conciseness, we point out a useful identification to make within Eqn. 3.28. Within the appropriate ensemble averages, the identity

$$\lim_{N_i\to\infty} \frac{1}{N_i} \sum_i \eta^\dagger_{[i]}(x_\mu)\phi_{[i]}(y_\mu) \to \overbrace{\chi(x_\mu)\bar{\chi}}(y_\mu). \tag{3.29}$$

holds, with the details that

- Matching subscripts $[i]$ corresponds to a contraction.
- By our convention, $\eta^\dagger \to \chi$, and $\phi \to \bar{\chi}$.

This identification is useful, in practice, for translating operator expectation values into contractions of noise vectors. As an example, we repeat the computation of Eqn. 3.7 using stochastic methods. As a reminder, the zero-momentum $\gamma_5\Gamma_5$ meson operator is given by (combining Eqn. 3.5 and 3.6)

$$\mathcal{O}(t)_\pi = \sum_{\vec{x}} \bar{\chi}(\vec{x},t)\epsilon(\vec{x},t)\chi(\vec{x},t). \tag{3.30}$$

Using the identifications defined above, we construct a "stochastic" operator

$$\mathcal{O}^{stoch}_{\pi,[i,j]}(t) = \sum_{\vec{x}} \phi_{[i]}(\vec{x},t)\epsilon(\vec{x},t)\eta^\dagger_{[j]}(\vec{x},t), \tag{3.31}$$

and form the combination

$$\lim_{N_i\to\infty} \frac{1}{N_i(N_i-1)} \sum_{i=1}^{N_i} \sum_{j=1,j\neq i}^{N_i} \mathcal{O}^{stoch}_{\pi,[i,j]}(0)\mathcal{O}^{stoch}_{\pi,[j,i]}(t). \tag{3.32}$$

Before performing a formal proof, we provide some intuition for this construction:

- The interchange of i and j between the two operators corresponds to always contracting a fermion with an antifermion.
- There is a double sum over noise sources because we need two propagators for a meson: each summed index corresponds to one propagator.
- The double sum is non-overlapping to avoid taking the square of stochastic quantities.

We will now prove that this expression indeed recreates the correlation function for the $\gamma_5\Gamma_5$ meson. For simplicity, we will also replace $N_i(N_i-1)$ with N_i^2 for the infinite N_i limit.

$$
\begin{aligned}
&\lim_{N_i\to\infty}\frac{1}{N_i^2}\sum_{i,j\neq i}\left\langle \mathcal{O}^{stoch}_{\pi,[i,j]}(0)\mathcal{O}^{stoch}_{\pi,[j,i]}(t)\right\rangle_{ens}\\
=&\lim_{N_i\to\infty}\frac{1}{N_i^2}\sum_{i,j\neq i}\left\langle\left(\sum_{\vec{x}}\phi_{[i]}(\vec{x},0)\epsilon(\vec{x},0)\eta^\dagger_{[j]}(\vec{x},0)\right)\left(\sum_{\vec{y}}\phi_{[j]}(\vec{y},t)\epsilon(\vec{y},t)\eta^\dagger_{[i]}(\vec{y},t)\right)\right\rangle_{ens}\\
=&\lim_{N_i\to\infty}\frac{1}{N_i^2}\sum_{i,j\neq i}\sum_{\vec{x},\vec{y}}\left\langle\left(\left(\sum_{z_\mu}G_F(z_\mu;\vec{x},0)\eta_{[i]}(z_\mu)\right)\epsilon(\vec{x},0)\eta^\dagger_{[j]}(\vec{x},0)\right)\times\right.\\
&\left.\left(\left(\sum_{w_\mu}G_F(w_\mu;\vec{y},t)\eta_{[j]}(w_\mu)\right)\epsilon(\vec{y},t)\eta^\dagger_{[i]}(\vec{y},t)\right)\right\rangle_{ens}\\
=&\lim_{N_i\to\infty}\sum_{\vec{x},\vec{y},z_\mu,w_\mu}\left\langle G_F(z_\mu;\vec{x},0)\left(\frac{1}{N_i}\sum_j\eta^\dagger_{[j]}(\vec{x},0)\eta_{[j]}(w_\mu)\right)\epsilon(\vec{x},0)G_F(w_\mu;\vec{y},t)\times\right.\\
&\left.\left(\frac{1}{N_i}\sum_i\eta^\dagger_{[i]}(\vec{y},t)\eta_{[i]}(z_\mu)\right)\epsilon(\vec{y},t)\right\rangle_{ens}\\
=&\sum_{\vec{x},\vec{y},z_\mu,w_\mu}\left\langle G_F(z_\mu;\vec{x},0)\delta_{\vec{x},\vec{w}}\delta_{0,w_t}\epsilon(\vec{x},0)G_F(w_\mu;\vec{y},t)\delta_{\vec{y},\vec{z}}\delta_{t,z_t}\epsilon(\vec{y},t)\right\rangle_{ens}\\
=&\sum_{\vec{x},\vec{y}}\langle G_F(\vec{y},t;\vec{x},0)\epsilon(\vec{x},0)G_F(\vec{x},0;\vec{y},t)\epsilon(\vec{y},t)\rangle_{ens}\\
=&\frac{1}{\mathcal{Z}}\int[dA]\sum_{\vec{x},\vec{y}}G_F(\vec{y},t;\vec{x},0)\epsilon(\vec{x},0)G_F(\vec{x},0;\vec{y},t)\epsilon(\vec{y},t)W[A]\\
=&\frac{1}{\mathcal{Z}}\int[dAd\bar{\chi}d\chi]\sum_{\vec{x}}\overline{\bar{\chi}(\vec{x},0)\epsilon(\vec{x},0)\,\underbrace{\chi(\vec{x},0)\sum_{\vec{y}}\bar{\chi}(\vec{y},t)\epsilon(\vec{y},t)\chi(\vec{y},t)}}e^{-S[A,\bar{\chi}_i,\chi_i]}\\
=&\langle\mathcal{O}_\pi(0)\mathcal{O}_\pi(t)\rangle\,.
\end{aligned}
\tag{3.33}
$$

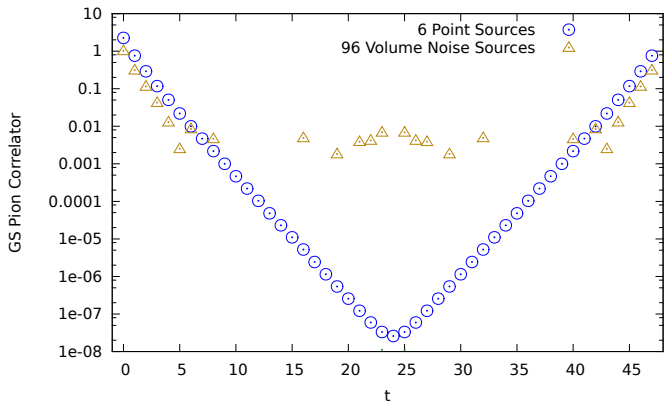

Figure 3.3. The Goldstone boson meson correlator compared between point and full volume stochastic sources. The Goldstone boson meson correlator is compared here on a single configuration between point and full volume stochastic sources. In blue, six point sources are used, which reproduces the entire Goldstone boson correlator. On the other hand, the equivalent measurement in yellow uses 96 stochastic sources. We notice that full volume stochastic sources become noisy away from small correlator separations. This is from a single configuration of a partner project studying the $SU(3)$ 8 fermion theory with $\beta = 4.8$, $m_\ell = 0.0075$ as a continuation of work in [90].

By using our previous identification, we could have skipped from the second line to the penultimate line of Eqn. 3.33. From here on, we will use the identity to simplify derivations and not go through the same detail.

Beyond the notational convenience, the numerical construction of these stochastic operators, such as Eqn. 3.31, has a computational advantage. In memory, constructing the stochastic Goldstone correlator amounts to constructing a single complex number $\mathcal{O}^{stoch}_{\pi,[i,j]}(t)$ for each timeslice and pair of indices via an inner product. This is far more efficient than instead constructing the actual propagator $G_F(\vec{x}, t; \vec{y}, t')$ by taking the *outer* product instead. This memory and time saving benefit is noted, for example, in [89].

As a test case, in Figure 3.3 we compare the Goldstone boson meson measured using six point sources versus with 96 full volume $U(1)$ stochastic sources on a single configuration to avoid questions of gauge fluctuations. We see that, in blue, the point sources show a good profile of a correlator through the entire range of separations. On the other hand, in yellow, the full volume stochastic sources degrade beyond a separation of $t \approx 4$. This degradation occurs because we are not in the infinite stochastic limit. In this case, the outer product of

η vectors is not the identity but

$$\frac{1}{N_i}\sum_i \eta^\dagger_{[i]}(\vec{x},0)\eta_{[i]}(\vec{w},w_t) \to \delta_{\vec{x},\vec{w}}\delta_{0,w_t} + R(\vec{x},0;\vec{w},w_t), \tag{3.34}$$

where R is a random noise matrix which, beyond having zero mean, has properties depend on the type of source (U_1, $\mathbf{Z}_2$, etc.) and the number N_i used. With full volume noise sources every off-diagonal element has a non-zero value. To see how this introduces noise in Figure 3.3, we consider, for example, the correlator at separation $t = 12$. Through the random number matrix, a noisy component may enter proportional to the noise times the correlator at a different separation, for example at $t = 0$ separation.

Since a correlator decays exponentially in time while the coupling through noise to $t = 0$ is constant, we have a large signal to noise problem. In the following section, we will demonstrate a method to avoid this exponential signal to noise problem by guaranteeing some components of the noise matrix R are zero.

3.5 Improved Stochastic Measurements: Dilution

The method of dilution was introduced in [91] as a systematic method to reduce noise from stochastic calculations. To motivate dilution, we will return to the notation in the original example, Eqn. 3.23. Given a single noise vector $\eta_{[i]}(x)$, we implicitly define a set of "diluted" noise vectors via

$$\eta_{[i]}(x) = \sum_{d=1}^{N_d} \eta^{(d)}_{[i]}(x), \tag{3.35}$$

where the exact construction of $\eta^{(d)}_{[i]}(x)$ can be arbitrary for any number of dilutions N_d. In general, dilutions are defined by a partitioning. We partition the coordinate space x into N_d parts indexed by d and denoted by $P(d)$ such that the union of all $P(d)$ span the entire coordinate space. We then define $\eta^{(d)}_{[i]}(x)$ by:

$$\eta_{[i]}^{(d)}(x) = \begin{cases} \eta_{[i]}(x) & : x \in P(d) \\ 0 & : x \notin P(d) \end{cases} \tag{3.36}$$

We note that

$$\lim_{N_i \to \infty} \frac{1}{N_i} \sum_{i=1}^{N_i} \eta_{[i]}^{(d)}(x) \eta_{[i]}^{(d)\dagger}(y) = \begin{cases} \mathbf{I}(x,y) & : x, y \in P(d) \\ 0 & : \text{else} \end{cases} \tag{3.37}$$

$$\rightarrow$$

$$\lim_{N_i \to \infty} \frac{1}{N_i} \sum_{i=1}^{N_i} \sum_{d=1}^{N_d} \eta_{[i]}^{(d)}(x) \eta_{[i]}^{(d)\dagger}(y) = \mathbf{I}(x,y). \tag{3.38}$$

The benefit of dilution is that the "else" part of Eqn. 3.37 is guaranteed to be zero for both finite and infinite N_i. Put differently, Eqn. 3.38 is now block diagonal with noise only in the blocks defined by the partitions.

Following the pattern before, we can define a vector $\phi_{[i]}^{(d)}(x)$ by

$$\phi_{[i]}^{(d)}(x) = S^{-1}(x,y) \eta_{[i]}^{(d)}(y), \tag{3.39}$$

noting

$$\begin{aligned} \sum_{d=1}^{N_d} \phi_{[i]}^{(d)}(x) &= \sum_{d=1}^{N_d} S^{-1}(x,y) \eta_{[i]}^{(d)}(y) \\ &= S^{-1}(x,y) \left[\sum_{d=1}^{N_d} \eta_{[i]}^{(d)}(y) \right] \\ &= S^{-1}(x,y) \eta_{[i]}(y) \\ &= \phi_{[i]}(x). \end{aligned} \tag{3.40}$$

With this property, we can approximate $S^{-1}(x,y)$ via

$$\begin{aligned}
\lim_{N_i\to\infty}\frac{1}{N_i}\sum_{i=1}^{N_i}\sum_{d=1}^{N_d}\eta_{[i]}^{(d)\dagger}(y)\phi_{[i]}^{(d)}(x) &= \lim_{N_i\to\infty}\frac{1}{N_i}\sum_{i=1}^{N_i}\sum_{d=1}^{N_d}\eta_{[i]}^{(d)\dagger}(y)S^{-1}(x,z)\eta_{[i]}^{(d)}(z) \\
&= \lim_{N_i\to\infty}\frac{1}{N_i}\sum_{i=1}^{N_i}\sum_{d=1}^{N_d}S^{-1}(x,z)\eta_{[i]}^{(d)}(z)\eta_{[i]}^{(d)\dagger}(y) \\
&= S^{-1}(x,z)\left[\lim_{N_i\to\infty}\frac{1}{N_i}\sum_{i=1}^{N_i}\sum_{d=1}^{N_d}\eta_{[i]}^{(d)}(z)\eta_{[i]}^{(d)\dagger}(y)\right] \\
&= S^{-1}(x,z)\mathbf{I}(z,y) \\
&= S^{-1}(x,y). \qquad (3.41)
\end{aligned}$$

As an example, we can apply dilution to the calculation of the connected $\gamma_5\Gamma_5$ meson correlator. We will use "timeslice dilution," where the partitions are defined by

$$\eta_{[i]}^{(t')}(x) = \begin{cases} \eta_{[i]}(\vec{x},t) & : t = t' \\ 0 & : t \neq t'. \end{cases} \qquad (3.42)$$

In the language of Eqn. 3.34, a component of the noise matrix R is zero if the component's row index and column index reflect different time coordinates.

In analogy to Eqn. 3.31, we define

$$\mathcal{O}_{\pi,[i,j]}^{stoch,(d,e)}(t) = \sum_{\vec{x}}\phi_{[i]}^{(d)}(x)\epsilon(x)\eta_{[j]}^{(e)\dagger}(x), \qquad (3.43)$$

and in analogy to Eqn. 3.32, we form the following combination:

$$\lim_{N_i\to\infty}\frac{1}{N_i(N_i-1)}\sum_{i=1}^{N_i}\sum_{j=1,j\neq i}^{N_i}\sum_{d,e=1}^{N_t}\mathcal{O}_{\pi,[i,j]}^{stoch,(d,e)}(0)\mathcal{O}_{\pi,[j,i]}^{stoch,(e,d)}(t). \qquad (3.44)$$

We can show this combination reproduces the $\gamma_5\Gamma_5$ meson.

$$
\begin{aligned}
&\lim_{N_i\to\infty}\frac{1}{N_i^2}\sum_{i,j\neq i}\sum_{d,e=1}^{N_t}\left\langle \mathcal{O}^{stoch,(d,e)}_{\pi,[i,j]}(0)\mathcal{O}^{stoch,(e,d)}_{\pi,[j,i]}(t)\right\rangle_{ens}\\
=&\lim_{N_i\to\infty}\frac{1}{N_i^2}\sum_{i,j\neq i}\sum_{d,e=1}^{N_t}\left\langle\left(\sum_{\vec{x}}\phi^{(d)}_{[i]}(\vec{x},0)\epsilon(\vec{x},0)\eta^{(e),\dagger}_{[j]}(\vec{x},0)\right)\times\right.\\
&\left.\left(\sum_{\vec{y}}\phi^{(e)}_{[j]}(\vec{y},t)\epsilon(\vec{y},t)\eta^{(d)\dagger}_{[i]}(\vec{y},t)\right)\right\rangle_{ens}\\
=&\lim_{N_i\to\infty}\frac{1}{N_i^2}\sum_{i,j\neq i}\sum_{d,e=1}^{N_t}\sum_{\vec{x},\vec{y}}\left\langle\left(\left(\sum_{z_\mu}G_F(z_\mu;\vec{x},0)\eta^{(d)}_{[i]}(z_\mu)\right)\epsilon(\vec{x},0)\eta^{(e)\dagger}_{[j]}(\vec{x},0)\right)\times\right.\\
&\left.\left(\left(\sum_{w_\mu}G_F(w_\mu;\vec{y},t)\eta^{(e)}_{[j]}(w_\mu)\right)\epsilon(\vec{y},t)\eta^{(d)\dagger}_{[i]}(\vec{y},t)\right)\right\rangle_{ens}\\
=&\lim_{N_i\to\infty}\sum_{\vec{x},\vec{y},z_\mu,w_\mu}\left\langle G_F(z_\mu;\vec{x},0)\left(\frac{1}{N_i}\sum_i\sum_d\eta^{(d)\dagger}_{[i]}(\vec{x},0)\eta^{(e)}_{[i]}(w_\mu)\right)\epsilon(\vec{x},0)G_F(w_\mu;\vec{y},t)\times\right.\\
&\left.\left(\frac{1}{N_i}\sum_j\sum_e\eta^{(e)\dagger}_{[j]}(\vec{y},t)\eta^{(e)}_{[j]}(z_\mu)\right)\epsilon(\vec{y},t)\right\rangle_{ens}\\
=&\sum_{\vec{x},\vec{y},z_\mu,w_\mu}\left\langle G_F(z_\mu;\vec{x},0)\delta_{\vec{x},\vec{w}}\delta_{0,w_t}\epsilon(\vec{x},0)G_F(w_\mu;\vec{y},t)\delta_{\vec{y},\vec{z}}\delta_{t,z_t}\epsilon(\vec{y},t)\right\rangle_{ens}\\
=&\sum_{\vec{x},\vec{y}}\langle G_F(\vec{y},t;\vec{x},0)\epsilon(\vec{x},0)G_F(\vec{x},0;\vec{y},t)\epsilon(\vec{y},t)\rangle_{ens}\\
=&\frac{1}{\mathcal{Z}}\int[dA]\sum_{\vec{x},\vec{y}}G_F(\vec{y},t;\vec{x},0)\epsilon(\vec{x},0)G_F(\vec{x},0;\vec{y},t)\epsilon(\vec{y},t)W[A]\\
=&\frac{1}{\mathcal{Z}}\int[dAd\bar{\chi}d\chi]\sum_{\vec{x}}\overbrace{\bar{\chi}(\vec{x},0)\epsilon(\vec{x},0)\,\underbrace{\chi(\vec{x},0)\sum_{\vec{y}}\bar{\chi}(\vec{y},t)\epsilon(\vec{y},t)\chi(\vec{y},t)}}e^{-S[A,\bar{\chi}_i,\chi_i]}\\
=&\langle\mathcal{O}_\pi(0)\mathcal{O}_\pi(t)\rangle\,.
\end{aligned}
\tag{3.45}
$$

As a simplifying point, we note that after the fourth line of the above derivation there are no changes compared with the derivation in Eqn. 3.33. We can also update the identification we made earlier in Eqn. 3.29:

$$
\lim_{N_i\to\infty}\frac{1}{N_i}\sum_i\sum_d\eta^{(d)\dagger}_{[i]}(x_\mu)\phi^{(d)}_{[i]}(y_\mu)\to\overbrace{\chi(x_\mu)\bar{\chi}}(y_\mu).
\tag{3.46}
$$

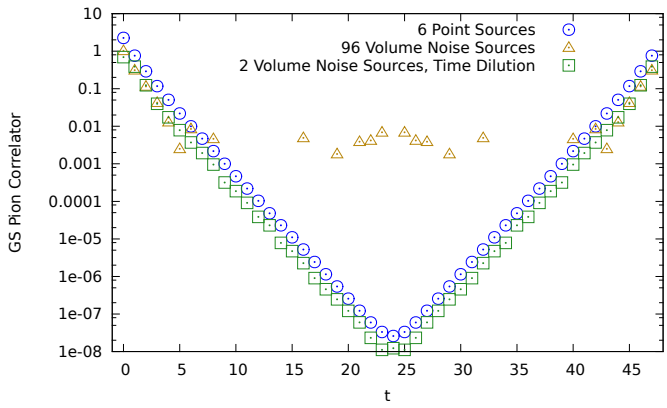

Figure 3.4. The Goldstone boson meson correlator compared between diluted and non-diluted stochastic sources. The Goldstone boson meson correlator is compared here on a single configuration between point, non-diluted, and timeslice diluted stochastic sources. This is equivalent to Figure 3.3 but with the addition of timeslice diluted points in green. Importantly, the timeslice diluted plot uses only 2 full volume sources, requiring 96 staggered Dirac matrix inversions, the same computational cost as the non-diluted result. This is from a single configuration of a partner project studying the $SU(3)$ 8 fermion theory with $\beta = 4.8$, $m_\ell = 0.0075$ as a continuation of work in [90].

To see the benefit of timeslice dilution, we turn to Figure 3.4. This figure is equivalent to Figure 3.3 but with the addition of measurements using timeslice dilution in green. With the addition of timeslice dilution, we can resolve the Goldstone boson correlator for all separations in t.

Most impressively, the non-diluted measurement and the timeslice diluted measurement had the same cost in terms of number of discrete staggered Dirac matrix inversions: both used 96 inversions. We note that the observation that six non-stochastic point sources works just as well is rather unique to the Goldstone boson correlator, and in most cases a measurement on a single configuration with just point sources will not give a reliable signal. This is documented, for example, in [91].

At this point, we are ready to discuss measuring the quark-line disconnected 0^{++} correlator.

3.6 Measuring the Isosinglet Meson: Theory

The interpolating operator for the spin scalar, taste scalar meson has the trivial spin-taste structure 1. After projecting to the zero momentum state, it has the operator form

$$\mathcal{O}_{0^{++}}(t) = \sum_{\vec{x}} \bar{\chi}(\vec{x},t)\chi(\vec{x},t). \tag{3.47}$$

For this discussion, it is important that we note that we are interested in the isosinglet meson, not the isomultiplet meson. This means that we cannot drop the quark-line disconnected contraction, and instead the full measurement is given by

$$\begin{aligned}
&\langle \mathcal{O}_{0^{++}}(0)\mathcal{O}_{0^{++}}(t)\rangle \\
=&\frac{1}{\mathcal{Z}}\int [dAd\bar{\chi}d\chi]\left\{\sum_{\vec{x}}\overbrace{\bar{\chi}(\vec{x},0)\chi}(\vec{x},0)\ \sum_{\vec{y}}\overbrace{\bar{\chi}(\vec{y},t)\chi}(\vec{y},t) - \right. \\
&\left. \sum_{\vec{x}}\overbrace{\bar{\chi}(\vec{x},0)\,\chi(\vec{x},0)\ \underbrace{\sum_{\vec{y}}\bar{\chi}(\vec{y},t)}\chi}(\vec{y},t)\right\} e^{-S[A,\bar{\chi}_i,\chi_i]} \\
=&\frac{1}{\mathcal{Z}}\int [dA]\left\{\frac{N_\ell}{4}\sum_{\vec{x}}\mathrm{Tr}\left[G_F(\vec{x},0;\vec{x},0)\right]\sum_{\vec{y}}\mathrm{Tr}\left[G_F(\vec{y},t;\vec{y},t)\right] - \right. \\
&\left. \sum_{\vec{x}}\sum_{\vec{y}}\mathrm{Tr}\left[G_F(\vec{x},0;\vec{y},t)G_F(\vec{y},t;\vec{x},0)\right]\right\} W[A] \\
=&\frac{1}{\mathcal{Z}}\int [dA]\sum_{\vec{x},\vec{y}}\left\{\frac{N_\ell}{4}\mathrm{Tr}\left[G_F(\vec{x},0;\vec{x},0)\right]\mathrm{Tr}\left[G_F(\vec{y},t;\vec{y},t)\right] - \right. \\
&\left. \mathrm{Tr}\left[G_F(\vec{x},0;\vec{y},t)G_F(\vec{y},t;\vec{x},0)\right]\right\} W[A] \\
=&\sum_{\vec{x},\vec{y}}\left[\frac{N_\ell}{4}\left\langle\mathrm{Tr}\left[G_F(\vec{x},0;\vec{x},0)\right]\mathrm{Tr}\left[G_F(\vec{y},t;\vec{y},t)\right]\right\rangle_{ens} - \right. \\
&\left. \left\langle\mathrm{Tr}\left[G_F(\vec{x},0;\vec{y},t)G_F(\vec{y},t;\vec{x},0)\right]\right\rangle_{ens}\right]
\end{aligned} \tag{3.48}$$

There are multiple quick remarks to make about these contractions.

- The factor of $\frac{N_\ell}{4}$ on the first term is a counting factor for the number of fields. The number of fields is counted twice on the first term (the quark-line disconnected or

just "disconnected" term) and on the second term (the quark-line connected or just "connected" term). The division by 4 is due to each staggered fermions containing four tastes.

- The connected term is equivalent to what we would compute if we were interested in the isomultiplet scalar meson, or in QCD language, the a_0 meson.

In light of the last remark, we will make the following definition for the connected piece for convenience of future discussion:

$$C_{\ell\ell}(t) = C(t) = \sum_{\vec{x},\vec{y}} \langle \mathrm{Tr}\left[G_F(\vec{x},0;\vec{y},t) G_F(\vec{y},t;\vec{x},0)\right]\rangle_{ens}\,. \tag{3.49}$$

The disconnected piece is more complicated. The isosinglet 0^{++} channel operator has a vacuum expectation value due to chiral symmetry breaking, that is,

$$\langle \mathrm{Tr}\left[G_F(\vec{x},0;\vec{x},0)\right]\rangle_{ens} \neq 0$$

We remark that this vacuum contribution is equal to the chiral condensate defined in Eqn. 3.22. This vacuum contribution must be subtracted explicitly during a lattice calculation. In the context of continuum perturbation theory, this can be thought of as removing the contribution of vacuum bubbles [92].

The proper, vacuum subtracted form for the 0^{++} correlator, modified from Eqn. 3.48, is

$$\begin{aligned}
&\langle \mathcal{O}_{0^{++}}(0)\mathcal{O}_{0^{++}}(t)\rangle \\
=&\frac{N_\ell}{4}\left[\sum_{\vec{x},\vec{y}} \langle \mathrm{Tr}\left[G_F(\vec{x},0;\vec{x},0)\right]\mathrm{Tr}\left[G_F(\vec{y},t;\vec{y},t)\right]\rangle_{ens} - \left\langle \sum_{\vec{x}} \mathrm{Tr}\left[G_F(\vec{x},0;\vec{x},0)\right]\right\rangle^2_{ens}\right] - C(t).
\end{aligned} \tag{3.50}$$

In practice, the vacuum subtraction is a numerically difficult topic. We will defer this discussion to section 4.5. For future reference, we will define the quark-line disconnected piece via

$$D_{\ell\ell}(t) = D(t) = \sum_{\vec{x},\vec{y}} \langle \mathrm{Tr}\left[G_F(\vec{x},0;\vec{x},0)\right] \mathrm{Tr}\left[G_F(\vec{y},t;\vec{y},t)\right]\rangle_{ens} - \left\langle \sum_{\vec{x}} \mathrm{Tr}\left[G_F(\vec{x},0;\vec{x},0)\right] \right\rangle^2_{ens}. \tag{3.51}$$

For future convenience, we will make the following definition:

$$\mathcal{O}_D(t) = \sum_{\vec{x}} \mathrm{Tr}\left[G_F(\vec{x},t;\vec{x},t)\right]. \tag{3.52}$$

We remark that we can build the entirety of Eqn. 3.51 out of $\mathcal{O}_D(t)$ for each noise source η in post processing. We will denote $\mathcal{O}_D(t)$ estimated from stochastic source (i) by $\mathcal{O}_{D,(i)}$.

Combining the quark-line connected and disconnected pieces, we define

$$S(t) = S_{\ell\ell}(t) \equiv \langle \mathcal{O}_{0^{++}}(0)\mathcal{O}_{0^{++}}(t)\rangle = \frac{N_\ell}{4} D_{\ell\ell}(t) - C_{\ell\ell}(t). \tag{3.53}$$

We parameterize Eqn. 3.49 and 3.53 in terms of the states they couple to by

$$-C(t) = A_{a_0} e^{-M_{a_0} t} + [\text{excited } a_0], \tag{3.54}$$

$$S(t) = A_{0^{++}} e^{-M_{0^{++}} t} + [\text{excited } 0^{++}],. \tag{3.55}$$

where we have recalled $C(t)$ is defined by the measurement of the iso*multiplet* spin-taste scalar state. For simplicity, we have also suppressed the contribution of the parity partner states in each channel, the $\gamma_4\gamma_5\Gamma_4\Gamma_5$ pseudoscalar for the quark-line connected correlator and the $\gamma_4\gamma_5\Gamma_4\Gamma_5$ isosinglet pseudoscalar (the η meson in QCD language) for the 0^{++} correlator. In practice, the parity partner states are only a numerically small contribution which can be suppressed analytically by methods discussed in appendix C.2.

It was noted in [35] that, despite not being a positive amplitude correlator, there is merit in studying only $D(t)$. In terms of Eqn. 3.54 and 3.55, $D(t)$ can be parameterized as

$$\begin{aligned} D(t) &= S(t) - (-C(t)) \\ &= A_{0^{++}} e^{-M_{0^{++}} t} - A_{a_0} e^{-M_{a_0} t} + \left([\text{excited } 0^{++}] - [\text{excited } a_0] \right). \end{aligned} \tag{3.56}$$

If the mass of the 0^{++} state is lighter than the mass of the a_0, the isosinglet will dominate for large t. The a_0 acts like an excited state, albeit with a negative amplitude. Further, we can argue that the excited states in the a_0 and the 0^{++} could cancel, which we give empirical support to in section 4.5.

As a last remark, we have made a large assumption in our discussion of measuring the light isosinglet 0^{++} meson by assuming that light and heavy fermion operators do not mix. In reality, both the light fermion operator of Eqn. 3.47 and the heavy fermion operator

$$\mathcal{O}_{0^{++},h}(t) = \sum_{\vec{x}} \bar{\chi}_h(\vec{x}, t)\, \chi_h(\vec{x}, t) \tag{3.57}$$

have the quantum numbers of an isosinglet zero momentum vacuum channel state and can mix due to quantum effects. We will assume for the present work that this mixing is negligible. Further, even if mixing is not negligible, it only effects the exact parameterization of the *amplitudes* in Eqn. 3.55 and Eqn. 3.56 and not the masses. For completeness, however, a discussion of mixing is present in appendix B.3.

3.7 Measuring the Isosinglet Meson: In Practice

In practice, we measure the 0^{++} meson using stochastic methods supplemented by the improvement offered by dilution. Following the example of [37], we not only dilute across timeslices but also in the $SU(3)$ of color, as well as on even/odd spatial sites.[3]

[3]Even/odd dilution can be thought of as chirality dilution, due to γ_5 hermiticity becoming even/odd hermiticity for staggered fermions.

As remarked earlier, we can use an improved estimator to measure the quark-line disconnected piece of the 0^{++} correlator. The improved estimator can be derived from a Ward identity for the staggered chiral symmetry, first noted in [84]. In the notation of this dissertation, the Ward identity gives

$$G_F(x_\mu; x_\mu) = m \sum_{z_\mu} |G_F(x_\mu; z_\mu)|^2 , \tag{3.58}$$

where m is the mass of the staggered Dirac operator. We will later demonstrate that this construction reduces the stochastic noise of the disconnected measurement. We propose, and will subsequently prove, that the improved estimator can be computed from the construction

$$G_F(x_\mu; x_\mu) = \lim_{N_i \to \infty} \frac{1}{N_i} \sum_i \sum_d m \phi^{(d)}_{[i]}(x_\mu) \phi^{(d)\dagger}_{[i]}(x_\mu). \tag{3.59}$$

The proof proceeds as

$$\begin{aligned}
&\lim_{N_i \to \infty} \frac{1}{N_i} \sum_i \sum_d m \phi^{(d)}_{[i]}(x_\mu) \phi^{(d)\dagger}_{[i]}(x_\mu) \\
&= \lim_{N_i \to \infty} \frac{1}{N_i} \sum_i \sum_d m \left(\sum_{y_\mu} G_F(y_\mu; x_\mu) \eta^{(d)}_{[i]}(y_\mu) \right) \left(\sum_{z_\mu} G_F(z_\mu; x_\mu) \eta^{(d)}_{[i]}(z_\mu) \right)^\dagger \\
&= m \sum_{y_\mu, z_\mu} \left(\lim_{N_i \to \infty} \frac{1}{N_i} \sum_i \sum_d \eta^{(d)}_{[i]}(y_\mu) \eta^{(d)\dagger}_{[i]}(z_\mu) \right) G_F(y_\mu; x_\mu) G_F(z_\mu; x_\mu)^\dagger \\
&= m \sum_{y_\mu, z_\mu} \delta_{y_\mu, z_\mu} G_F(y_\mu; x_\mu) G_F(z_\mu; x_\mu)^\dagger \\
&= m \sum_{z_\mu} |G_F(z_\mu; x_\mu)|^2 \\
&= m \sum_{z_\mu} |G_F(x_\mu; z_\mu)|^2 \\
&= G_F(x_\mu; x_\mu).
\end{aligned} \tag{3.60}$$

In Figure 3.5, we show the difference between using the unimproved and the improved estimator for $\mathcal{O}_D(t)$ in Eqn. 3.51. We compare the unimproved operator, denoted by yellow

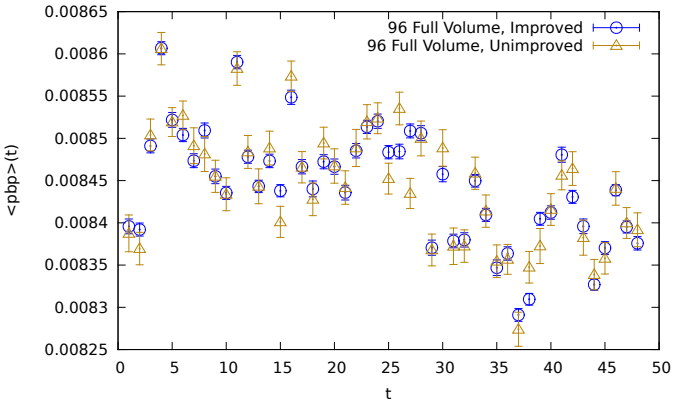

Figure 3.5. A comparison of improved versus unimproved estimators for the chiral condensate. The value of the chiral condensate operator as a function of timeslice, which is used to build Eqn. 3.51, compared between the unimproved (yellow) and the improved (blue) estimator. This comparison uses 96 stochastic sources which are not diluted. We see that the error bars from the measurements with the improved operators are about one half the size of the unimproved operator. This is from a single configuration of a partner project studying the $SU(3)$ 8 fermion theory with $\beta = 4.8$, $m_\ell = 0.0075$ as a continuation of work in [90].

data points, with the improved operator, in blue, on a timeslice by timeslice basis. In this example, we used only 96 non-diluted sources, where the *same* sources went into both calculations. The improved operator features one-half the error as the unimproved operator at no additional cost.

In terms of numerical costs, 0^{++} measurements dominate isomultiplet measurements on a configuration-by-configuration basis. Our choices require $6 \times 3 \times 2 \times T$ discrete staggered Dirac matrix inversions (corresponding to 6 sources, then color, space even/odd, and timeslice dilution, respectively) per configuration, or 1728 inversions on $24^3 \times 48$ volumes and 2304 on $32^3 \times 64$. This is in stark contrast to the wall source quark-line connected measurements described in section 3.3, which require 36 inversions on a $24^3 \times 48$ volume and 48 inversions on a $32^3 \times 64$ volume.

The choice to use a relatively small number of stochastic sources came after a study comparing the effect of gauge noise and stochastic noise, summarized in Figure 3.6. The different vertical lines partition results using a different numbers of stochastic sources per configuration, increasing from left to right as 4, 8, 16, 32, and 64 sources. In each case

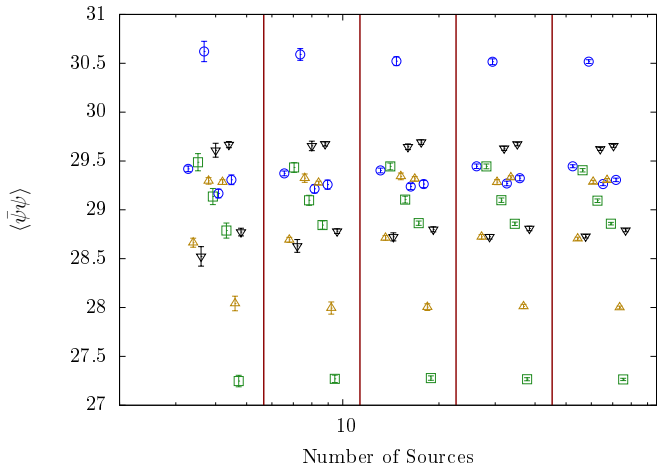

Figure 3.6. A comparison of gauge noise and stochastic noise for chiral condensate measurements. This figure overviews a comparison of gauge noise and stochastic noise for chiral condensate measurements. The solid vertical lines correspond to separating measurements for, from left to right, 4, 8, 16, 32, and 64 stochastic sources each diluted in time, color, and space even/odd. Different data points within each section correspond to different well-separated gauge configurations. The distinguishing feature is the fluctuations with respect to gauge noise dominate by orders of magnitude over the stochastic noise. This study comes from a $24^3 \times 48$ ensemble for $m_\ell = 0.005$, $m_h = 0.080$.

we used the improved operator and the full dilution pattern. Different data points in each partition respectively correspond to a unique configuration well separated along the HMC as to not worry about autocorrelation. We see from looking at this figure that the gauge noise corresponds to fluctuations that are much larger in magnitude than the stochastic noise. Until at least order 1000 independent gauge measurements are performed, the gauge noise dominates over stochastic noise. As such, additional noise sources would supply severely diminishing returns even with large gauge statistics, as also discussed in [91].

We now have all of the tools we need to measure the isosinglet meson correlator Eqn. 3.53:

- The connected piece, Eqn. 3.49, can be built analogously to building the $\gamma_5\Gamma_5$ meson correlator as described in section 3.5 by constructing diluted stochastic operators similar to Eqn. 3.43.

- The disconnected piece, Eqn. 3.51, can be built in post-processing so long as we save $\mathcal{O}_D(t)$ as defined in Eqn. 3.52 on each ensemble on all timeslices t for each noise source.

As written, the connected piece requires a large amount of computer memory and FLOPs spent on inner products. We have derived and made use of a simple trick to reduce memory usage. To motivate this trig, we consider the connected correlator written in terms of stochastic operators

$$\lim_{N_i\to\infty} \frac{1}{N_i(N_i-1)} \sum_{i,j\neq i} \sum_{d,e=1}^{N_t} \left\langle \mathcal{O}^{stoch,(d,e)}_{0^{++},[i,j]}(0) \mathcal{O}^{stoch,(e,d)}_{0^{++},[j,i]}(t) \right\rangle_{ens}. \tag{3.61}$$

We make a bold conjecture: we assert that there is some condition under which, from Eqn. 3.61, we can satisfy

$$\mathcal{O}^{stoch,(d,e)}_{0^{++},[i,j]}(0) \propto \mathcal{O}^{stoch,(e,d)\dagger}_{0^{++},[j,i]}(t). \tag{3.62}$$

Let us pursue this route. We begin by expanding the left hand side of Eqn. 3.62:

$$\begin{aligned}
\mathcal{O}^{stoch,(d,e)}_{0^{++},[i,j]}(0) &= \left(\sum_{\vec{x}} \phi^{(d)}_{[i]}(\vec{x},0) \eta^{(e),\dagger}_{[j]}(\vec{x},0) \right) \\
&= \left(\sum_{\vec{x}} \left(\sum_{z_\mu} G_F(z_\mu;\vec{x},0) \eta^{(d)}_{[i]}(z_\mu) \right) \eta^{(e)\dagger}_{[j]}(\vec{x},0) \right) \\
&= \sum_{\vec{x},z_\mu} G_F(z_\mu;\vec{x},0) \eta^{(d)}_{[i]}(z_\mu) \eta^{(e)\dagger}_{[j]}(\vec{x},0).
\end{aligned} \tag{3.63}$$

Next, we expand the right-hand side.

$$\begin{aligned}
\mathcal{O}^{stoch,(e,d)\dagger}_{0^{++},[j,i]}(t) &= \left(\sum_{\vec{x}} \phi^{(e)}_{[j]}(\vec{x},t) \eta^{(d),\dagger}_{[i]}(\vec{x},t) \right)^\dagger \\
&= \left(\sum_{\vec{x}} \left(\sum_{z_\mu} G_F(z_\mu;\vec{x},t) \eta^{(e)}_{[j]}(z_\mu) \right) \eta^{(d)\dagger}_{[i]}(\vec{x},t) \right)^\dagger \\
&= \sum_{\vec{x},z_\mu} G_F(z_\mu;\vec{x},t)^\dagger \eta^{(e)\dagger}_{[j]}(z_\mu) \eta^{(d)}_{[i]}(\vec{x},t) \\
&= \sum_{\vec{x},z_\mu} G_F(\vec{x},t;z_\mu) \epsilon(\vec{x},t) \epsilon(z_\mu) \eta^{(e)\dagger}_{[j]}(z_\mu) \eta^{(d)}_{[i]}(\vec{x},t).
\end{aligned} \tag{3.64}$$

Let us compare Eqn. 3.63 and 3.64. Assume that the dilution pattern (d) included timeslice dilution such that $\eta^{(d)}_{[i]}$ was only non-zero on timeslice t, and dilution pattern (e) included timeslice dilution such that $\eta^{(e)}_{[j]}$ was only non-zero on timeslice 0, In this case, the sum over z_μ would only be a spatial sum since the temporal sum would be restricted to one value by timeslice dilution. In Eqn. 3.63, the time component of z_μ would be restricted to t, and in Eqn. 3.64, the time component of z_μ would be restricted to 0. In this case, and for both Eqn. 3.63 and 3.64, we could freely interchange the labels $\vec{x}$ and $\vec{z}$ in the sum.

If we do this and perform the relabeling, we have:

$$\mathcal{O}^{stoch,(d,e)}_{0^{++},[i,j]}(0) = \sum_{\vec{x},\vec{z}} G_F(\vec{z},t;\vec{x},0)\eta^{(d)}_{[i]}(\vec{z},t)\eta^{(e)\dagger}_{[j]}(\vec{x},0), \tag{3.65}$$

$$\mathcal{O}^{stoch,(e,d)\dagger}_{0^{++},[j,i]}(t) = \sum_{\vec{x},\vec{z}} G_F(\vec{z},t;\vec{x},0)\epsilon(\vec{z},t)\epsilon(\vec{x},0)\eta^{(e)\dagger}_{[j]}(\vec{z},0)\eta^{(d)}_{[i]}(\vec{x},t). \tag{3.66}$$

The only remaining difference between Eqn. 3.65 and 3.66 is the existence of ϵ symbols in Eqn. 3.66 that are missing from Eqn. 3.65. We can address this issue if we assume the dilution patterns (d) and (e) also include spatial even/odd dilution. In this case, the factors of $\epsilon(\vec{z},t)$ and $\epsilon(\vec{x},0)$ could be factored out as they are constants with respects to sums uniquely over even or odd sites.

Between timeslice and spatial even/odd dilution, we have satisfied Eqn. 3.62. By numerically computing $\mathcal{O}^{stoch,(d,e)}_{0^{++},[i,j]}(0)$, we automatically obtain $\mathcal{O}^{stoch,(e,d)}_{0^{++},[j,i]}(t)$ after a quick complex conjugation and sign change from $\epsilon(x_\mu)$ symbols. This allows us to build the quark-line connected piece of the 0^{++} correlator with low memory overhead: only the six of the η vectors and a single $\phi^{(d)}_{[i]}$ vector need to be held in memory at a given time.

With this last tool in mind, we can measure the 0^{++} correlator. We are now ready to discuss analyzing correlators in chapter 4.

4 Analysis of Measurements

4.1 Isomultiplet Spectrum Analysis

As we discussed in section 3.1, for a general meson state, the correlator can be factored into two parts, a direct and an oscillating part[1]

$$C_{\mathcal{O}}(t) = \left(\sum_n a_n e^{-E_n^a t}\right) + \left(\sum_n b_n (-1)^t e^{-E_n^b t}\right) \tag{4.1}$$

The first sum corresponds to the direct case (labeled a), and the second to the oscillating term (labeled b). We order the sum according to:

$$E_0^a < E_1^a < \cdots \qquad\qquad E_0^b < E_1^b < \cdots$$

No guarantee can be made about the relative ordering between E_i^a's and E_i^b's, as they have different quantum numbers.

As $t \to \infty$, the correlator is dominated by the lightest state in the direct and the oscillating channel with all other states becoming exponentially suppressed. This correlator can be parameterized as

$$C(t) = a_0 e^{-E_0^a t} + b_0 (-1)^t e^{-E_0^b t} \tag{4.2}$$

In this case, E_0^a and E_0^b correspond to the mass of the ground state meson with the quantum numbers for the direct and oscillating state, respectively, and the coefficients in front, a_0 and b_0, are related to vacuum-to-"state" amplitudes (such as F_π in QCD).

In our case, we are measuring these correlation functions sampled via a Markov chain so we have a series of measurements with a corresponding central value and error. To

[1] Again, we will ignore the boundary conditions: the appropriate function is a hyperbolic cosine function, not a single decaying exponential.

extract meaningful estimates of the errors of the fit parameters, a_0, E_0^a, b_0, E_0^b, with errors, we perform non-linear correlated fits to the measured correlation functions.

Before discussing fitting, though, we must first discuss addressing autocorrelation in data. This is also relevant for our discussions of the topological charge in section 2.7.

4.2 Autocorrelation and Errors

By using the HMC algorithm, we are in a sense generating a continuous "time series" of configurations. It is possible that our measured data features some amount of autocorrelation, that is, sequential measurements are not statistically independent. In this section we will discuss two methods to check for and address autocorrelation: direct calculation and jackknife resampling. Jackknife resampling also doubles as a method to find approximate errors on non-linearly derived quantities.

Let us assume that we have a set of N, not necessarily independent, measurements y_t^i, where i indexes the configuration and, as needed, t is a parameter indexing a timeslice. One method to estimate the autocorrelation of y_t^i is outlined in [93], which is implemented in a free-to-download `MATLAB` function `UWerr`. In a black-box sense, this function takes in a time series of data and outputs the central value, error, and error of the error corrected for autocorrelation[2] as well as an estimate of the autocorrelation in units of measurement frequency. We use `UWerr` to estimate the autocorrelation of the topological charge, $\langle E \rangle$from the Wilson flow analysis, and the chiral condensate.

It is also possible to quantify and address the effects of autocorrelation as a byproduct of a jackknife resampling. We begin by defining a single elimination jackknife as defined in [94]. We define N jackknifed values, $\tilde{y}_t^j$, from the original dataset y_t^i by the expression

$$\tilde{y}_t^{j,(1)} = \frac{1}{N-1} \sum_{i \neq j} y_t^i. \tag{4.3}$$

[2] Autocorrelation causes naïvely computed errors to be under-approximated because it artificially inflates the number of measurements.

We can see how this gets the name single-elimination: to define each jackknife value $\tilde{y}_t^j$, we average over all of the data y_t^i, except for a *single* data point that gets *eliminated*. The mean of the single-elimination jackknife values is equal to the mean of the original data,

$$\overline{y}_t = \frac{1}{N}\sum_{j=1}^{N} y_t^{j,(1)} = \frac{1}{N}\sum_{i=1}^{N} \tilde{y}_t^i. \tag{4.4}$$

Next, we define a jackknife covariance of the error which by construction also agrees with the covariance of the original data:

$$\sigma_{t,t'}^{2,(1)} = \frac{N-1}{N}\sum_{j=1}^{N}\left(\tilde{y}_t^{j,1} - \overline{y}_t\right)\left(\tilde{y}_{t'}^{j,1} - \overline{y}_{t'}\right), \tag{4.5}$$

where to be explicit, the error of y_t^i is

$$\sigma_t^{(1)} = \sqrt{\sigma_{t,t}^{2,(1)}} = \sqrt{\frac{N-1}{N}\sum_{j=1}^{N}\left(\tilde{y}_t^{j,1} - \overline{y}_t\right)^2}. \tag{4.6}$$

This far, we have done nothing to address autocorrelation. To look at the effect of autocorrelations, we apply the n-elimination jackknife.

Under an n-elimination jackknife, we define $N_{block} = N/n$ jackknife block values defined by

$$\tilde{y}_t^{j,(n)} = \frac{1}{N-n}\sum_{i\notin b_j} y_t^i, \tag{4.7}$$

where b_j is the n values of y_t^i in the interval $[(j-1)n+1, jn]$, inclusive. More qualitatively, for each block, we eliminate n values in sequence.

In the case that n does not evenly divide into N, we apply the consistent convention that we throw out extra values when defining the first and the last block. As an example, we consider $N = 26, n = 3$. There are two extra data points when dividing $N = 26$ by 3. By convention, when defining the first and last block, we use the first four and the last

four measurements, respectively, instead of the first and last three. This convention induces potential deviations in the mean and the error which come at order $\frac{1}{N}$, negligible in the large N limit.

Under an n-elimination, the jackknife covariance of the error is defined by

$$\sigma^{2,(n)}_{t,t'} = \frac{N-n}{N} \sum_{j=1}^{N_{block}} \left(\tilde{y}^{j,(n)}_t - \overline{y}_t\right)\left(\tilde{y}^{j,(n)}_{t'} - \overline{y}_{t'}\right), \tag{4.8}$$

and the jackknife error is

$$\sigma^{(n)}_t = \sqrt{\sigma^{2,(n)}_{t,t}} = \sqrt{\frac{N-n}{N} \sum_{j=1}^{N_{block}} \left(\tilde{y}^{j,(n)}_t - \overline{y}_t\right)^2}. \tag{4.9}$$

We can now discuss using n-elimination jackknife to study autocorrelation. Let us assume there is an autocorrelation in a measurement of 5 measurements. The error, $\sigma^{(n)}_t$, will increase as a function of n until approximately $n = 5$, at which point it plateaus. For a general set of data, this method of hunting for a plateau defines a method to approximate the autocorrelation.

To see why this works, we recast the n-elimination jackknife in terms of *binning* the data first, and then computing an error. We define binned values of y^i_t via

$$y^{j,(n)}_t = \frac{1}{n} \sum_{i \in b_j} y^i_t, \tag{4.10}$$

where the groups b_j are identical to the groups defined for Eqn. 4.7 for n-elimination. This gives us N_{block} binned data points. Up to order $\frac{1}{N}$ effects related to n not dividing evenly into N, we can then use the single-elimination jackknife equations on the N_{block} binned data points to find the mean, covariance of the error, and the error. If the bin size is larger than the autocorrelation time, we have created N_{block} independent measurements.

In practice, we find the autocorrelation of our base quantities, such as correlators, by using `UWerr`, bin such measurements with the reported autocorrelation time, and use these

new binned values as the input to a jackknife analysis for derived quantities such as fit masses as described in the following section.

With the discussion of addressing autocorrelation in mind, we will assume going forward that all data does not feature autocorrelation.

4.3 Nonlinear Least Squares Fitting and Errors

Let us consider the problem of general least-squares fitting. In the least-square-residual sense, the best fit parameters are found by minimizing the χ^2 function

$$\chi^2 = \sum_{t,t'} \left(\overline{y}_t - f(\vec{\alpha}; t)\right) \sigma^{-2}_{t,t'} \left(\overline{y}_{t'} - f(\vec{\alpha}; t')\right), \tag{4.11}$$

with respect to the non-linear fit parameters $\vec{\alpha}$. The sum over t may only be over a subset of all possible values, for example, when fitting correlators. This may be because our fit ansatz is only valid over a subset of the full interval. In an abuse of notation, $\sigma^{-2}_{t,t'}$ is the inverse of the variance-covariance matrix, where $\sigma^2_{t,t'}$ is a square, symmetric matrix over the desired subinterval of t.

Let us now specialize to a general staggered meson correlator containing n direct states and m oscillating states. The fit function $f(\vec{\alpha}; t)$ takes the form

$$f(\vec{\alpha}; t) = \sum_{i=1}^{n} A_i \cosh\left(M_i^a \left(T/2 - t\right)\right) + \sum_{j=1}^{m} B_j (-1)^t \cosh\left(M_j^b \left(T/2 - t\right)\right), \tag{4.12}$$

where we have assumed periodic boundary conditions, A_i and B_j are related to the amplitudes defined in Eqn. 4.1 by $a_i = 2A_i e^{M_i^a T/2}$, $b_i = 2B_i e^{M_i^b T/2}$, and M_i^a and M_j^b are the masses of states. The free parameters in this fit are the A_i's, B_j's, and $M's$, which take the place of the $\vec{\alpha}$ in Eqn. 4.11. For an $n+m$ state fit, there are $2(n+m)$ free parameters.

Finding the least squares fit parameters requires minimizing the χ^2 in Eqn. 4.11 with the functional form in Eqn. 4.12 with respect to the A_i's, B_i's, and M's. For the analysis in this dissertation, we minimize the χ^2 function via the Nelder-Mead simplex direct

search method [95] as implemented via `MATLAB`'s function `fminsearch`. Other minimization algorithms include the gradient-descent and non-linear conjugate gradient algorithm. For a stable fit, any method must give an equivalent answer.

Since these fits are non-linear, it is important to supply initial guesses to these fits. We outline methods to find initial guesses in section 4.4. In some cases, it may be useful to perform an uncorrelated fit (assume the variance-covariance matrix is diagonal, with the off-diagonal elements replaced by zero) after finding initial guesses but before performing the correlated fit. This progression may be more numerically stable.

In practice, we only perform fits to a single direct and oscillating state, which is generally stable with respect to an initial guess so long as the amplitudes A_1 and B_1 are given the correct positive or negative sign.

To check the goodness of fit for correlated fits, we can at first order look at the quantity χ^2_{min}/N_{dof}, where N_{dof} is equal to the number of data points (y_t's) minus the number of parameters in the fit ($2N$, or 2 for a fit to a single direct state, $n + m$. In general, an acceptable fit has $\chi^2_{min}/N_{dof} \approx 1$, with a large value becoming less acceptable.

As a more rigorous test, one looks at the p value of a fit. The p value is defined as 1 minus the integral of the χ^2 distribution for N_{dof} from 0 to the measured χ^2_{min}. The p value with this convention represents the probability that the true χ^2_{min} is less than or equal to the measured χ^2. As a convention, we look for the p value to be greater than 0.05. We compute the integrated χ^2 distribution via `MATLAB`'s function `chi2cdf`. A benefit of the p value is that it is agnostic of the number of degrees of freedom, making it more meaningful for comparing two fits with a different N_{dof}. For many purposes, though, looking at χ^2/N_{dof} gives a sufficient qualitative idea of the quality of a fit.

We remark that a poor fit does not necessarily mean the data is of poor quality. It may mean the data is of sufficient quality that we can resolve excited states, and need to change our fit ansatz.

We make the further remark that, if the data $\overline{y}_t$ have correlations amongst different values of t, an uncorrelated fit does not give a statistically well defined χ^2 value, which

makes a p-value test meaningless. In this case, the best way to evaluate the goodness of the fit is to visually inspect how the fit curve lies on the data. Even with correlated fits, one should visually inspect a derived fit curve.

To measure the errors of the fit parameters, we can use the jackknife procedure described in section 4.2. For a given t_{min}, t_{max}, and fit parameterization, let us assume we have already performed a fit to the central values of a correlator. For discussion, we will focus on defining the error on the fit result for M_1^a, denoted $\overline{M}_1^a$.

To approximate the error, we obtain jackknife block values of M_1^a by repeating the fit but replacing $\overline{y}_t$ in Eqn. 4.11 with $\tilde{y}_t^{j,(n)}$ for all N_{block} values of $\tilde{y}_t^{j,(n)}$. This gives us N_{block} jackknife values of, for example, M_1^a which we denote $M_1^{a,j,(n)}$.

As a remark, with this convention, we reuse the covariance matrix as defined from the full data set defined in Eqn. 4.8. This is an $\mathcal{O}(\frac{1}{N})$ approximation known as using a "frozen" covariance matrix. To be strictly correct, we should also replace the covariance matrix in the fit with the covariance of the n-elimination jackknife dataset.

Once we have the N_{block} values of $M_1^{a,j,(n)}$, we can compute an approximation to the error via Eqn. 4.8. We note that the central value of the mass, $\overline{M}_1^a$, does *not* in general equal the mean of the N_{block} values of $M_1^{a,j,(n)}$.

We have now outlined how, given a fixed parameterization, t_{min}, and t_{max}, we can find the central values of the fit parameters, check the acceptability of the fit via a p value, and find errors on the central values of the fit parameters through the jackknife procedure. We will now specialize this for our analysis of the quark-line connected spectrum for the 4+8 model. The disconnected spectrum requires special care as outlined in section 4.5.

For the current state of the analysis of the isomultiplet spectrum, we do not perform any excited state analysis, but instead we fit to only one direct plus one oscillating state via the functional form

$$f(\vec{\alpha};t) = A_1 \cosh\left(M_1^a\left(T/2-t\right)\right) + B_1(-1)^t \cosh\left(M_1^b\left(T/2-t\right)\right). \tag{4.13}$$

In the case of the Goldstone boson pion, we only need to fit the form

$$f(\vec{\alpha}; t) = A_1 \cosh\left(M_1^a \left(T/2 - t\right)\right). \tag{4.14}$$

Before performing a fit, we exploit the symmetry of the correlator about $T/2$ by "folding" the data as described in appendix C.2. We then study fits from all possible values of t_{min} to a t_{max} of either T/2 or less for correlators that are noisy near the center.

In performing these fits, we currently follow the following prescription in the interest of automating the fitting procedure:

1. Find initial guesses for A_1, M_1^a, and B_1, M_1^b if needed, valid around $t = 10$. Finding initial guesses is described in section 4.4.

2. Using these initial guesses, we perform a non-linear fit from $t_{min} = 10$ to the above decided t_{max}, computing the errors on the fit parameters via a single-elimination jackknife.

3. Using the results from $t_{min} = 10$ to t_{max} as initial guesses, fit from $t_{min} = 9$ to t_{max} and find errors. Next use the results from $t_{min} = 9$ as an initial guess for $t_{min} = 8$, and repeat until reaching $t_{min} = 1$.

4. Next go in the other direction, using the results from $t_{min} = 10$ as an initial guess for a fit from $t_{min} = 11$, find errors, use these results as initial guesses for $t_{min} = 12$, and repeat until reaching $t_{min} = t_{max} - N_{dof} - 2$.

The choice to start from $t = 10$ is *ad hoc* but effective in practice, offering a balance between excited state contamination for smaller t and noise at larger t. There is no reason why we could not start from a value of t which is one or two smaller or larger.

We reuse fit results for neighboring intervals as initial guesses because we expect fit results to vary smoothly with t_{min}.

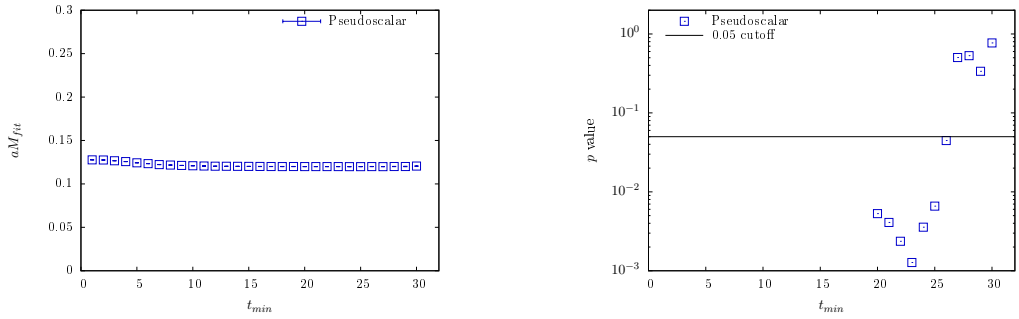

Figure 4.1. Example single state fits to a correlator without a parity partner. An example of single state fits to a correlator without a parity partner as parameterized in Eqn. 4.14. This example is from 1000 measurements on the $36^3 \times 64$, $m_\ell = 0.003$, $m_h = 0.080$ ensemble. Left: The mass extracted from a fit to the Goldstone boson $\gamma_5\Gamma_5$ meson state with a wall source from variable t_{min} to a fixed $t_{max} = T/2$, the center of the correlator. Right: The p value of the fit as a function of t_{min}. We note that, for larger t_{min} values, the fit is acceptable. For smaller t_{min} values, the p-value drops below 0.05 (the horizontal black line), corresponding the presence of excited state contamination.

The choice to fit up to $t_{min} = t_{max} - N_{dof} - 2$ is *ad hoc*, but reasonable as it avoids performing fits where the number of degrees of freedom is equal to the number of free parameters.

As an example, we document two fits: one without an oscillating term, and one with an oscillating term.

First, we fit to the Goldstone boson $\gamma_5\Gamma_5$ state originally shown in Figure 3.1. In Figure 4.1, we see on the left the fit mass aM_π from a fit to a variable t_{min} to a fixed $t_{max} = 32$, the center of the correlator. The fit is parameterized by Eqn. 4.14, and includes the full covariance as described in Eqn. 4.11. The fit is statistically independent of t_{min} for a large range of potential values. This is because the wall source couples only weakly to excited states as we saw in Figure 3.2. For a sufficiently small t_{min}, excited state contamination sets in as noted by the p value plot on the right hand side of Figure 4.1. It is only for larger values of t_{min} that the fit is acceptable, having a p value larger than 0.05. For smaller t_{min} values, the fit becomes unacceptable. For this correlator, we use $t_{min} = 27$, corresponding to $aM_\pi = 0.11992(12)$, where the error in parenthesis is statistical as determined by the jackknife procedure described in section 4.2.

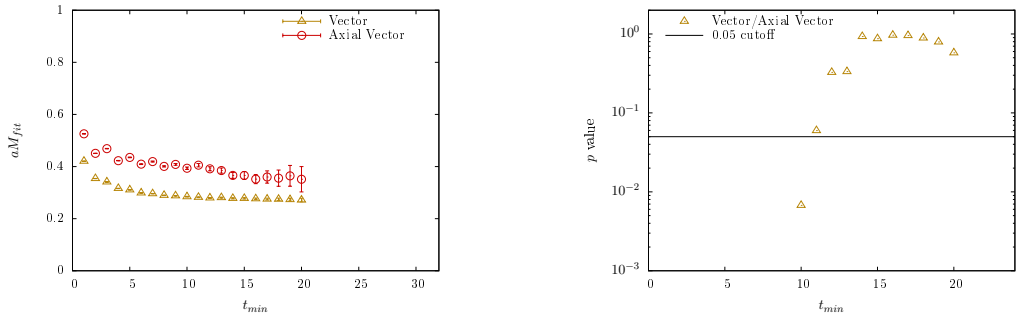

Figure 4.2. Example single state fits to a correlator with a parity partner. An example of single state fits to a correlator with a parity partner as parameterized in Eqn. 4.13. This example is from 1000 measurements on the $36^3 \times 64$, $m_\ell = 0.003$, $m_h = 0.080$ ensemble. Left: The mass extracted from a fit to a vector $\gamma_3\gamma_4\Gamma_1\Gamma_5$ meson state (yellow), parity partner axial vector $\gamma_3\gamma_5\Gamma_1\Gamma_4$ meson (red), with a wall source from variable t_{min} to a fixed $t_{max} = 24$. Right: The p value of the fit as a function of t_{min}. We note that, for larger t_{min} values, the fit is acceptable. For smaller t_{min} values, the p-value drops below 0.05 (the horizontal black line), corresponding the arrival of excited state contamination.

The choice in t_{min} hinges on two factors: the fit itself being acceptable, and the fit parameters being stable with respect to neighboring values of t_{min}. If the fit mass is fluctuating above statistical noise as a function of t_{min}, the fit may not be trustworthy because of noise or a strong excited state presence.

Next, we refer to a fit to a vector meson with its axial vector oscillating partner. This corresponds to a correlated fit to the oscillating correlator in Figure 3.1. In Figure 4.2, we see on the left the fit mass for the vector (yellow) and the axial vector (red) simultaneously extracted from a fit to a variable t_{min} to a fixed $t_{max} = 24$. The fit is parameterized by Eqn. 4.13, and includes the full covariance as described in Eqn. 4.11. For larger value of t_{min}, both the mass of the vector meson and the axial vector meson are rather constant. For smaller t_{min}, we see the extracted mass of the vector meson rise, and the axial vector meson mass both appears to oscillate as well as raise in value. By referring to the p-value plot on the right hand side of Figure 4.2, we see that the fit loses acceptability for $t_{min} < 11$. This coincides with the onset of excited state features in the left hand figure. For this fit we choose $t_{min} = 15$, corresponding to $aM_\rho = 0.2779(27)$ for the vector meson, and $aM_{a_1} = 0.366(15)$ for the axial vector meson, where again the error is statistical as

determined by the jackknife procedure described in section 4.2.

The choice of t_{max} is best motivated within the discussion of the following section. In short, we can argue that the correlator is too noisy for $t > t_{max}$ to be of any meaningful contribution.

4.4 Finding Initial Guesses: Effective Masses

Next, we will discuss how to find good initial guesses to non-linear fits. We will focus on the case where we can assume there is only one state, and then briefly discuss a general method to find initial guesses when there are an arbitrary number of decaying and oscillating states.

Let us remind ourselves of the form of a single hyperbolic cosine correlator.

$$\begin{aligned} C(t) &= A_1 \cosh\left(M_1^a \left(T/2 - t\right)\right) \\ &= \frac{A_1}{2}\left(e^{M_1^a(T/2-t)} + e^{-M_1^a(T/2-t)}\right), \end{aligned} \tag{4.15}$$

If we choose a value of t far from T/2 (let us take $t < T/2$), then one exponential in the hyperbolic cosine is dominant and we find

$$C(t) \approx \frac{A_1 e^{M_1^a T/2}}{2} e^{-M_1^a t}. \tag{4.16}$$

We can now extract a two-point "effective" mass that is exact for a single exponential via

$$\begin{aligned} m_{eff}(t) &= \log\left(\frac{C(t)}{C(t+1)}\right) \\ &= \log\left(\frac{\frac{A_1 e^{M_1^a T/2}}{2} e^{-M_1^a t}}{\frac{A_1 e^{M_1^a T/2}}{2} e^{-M_1^a (t+1)}}\right) \\ &= \log\left(e^{M_1^a}\right) \\ &= M_1^a. \end{aligned} \tag{4.17}$$

Given a set of data $\overline{y}_t$, we can compute a series of effective masses by replacing $C(t)$ and $C(t+1)$ by $\overline{y}_t$ and $\overline{y}_{t+1}$ for all t. Similarly, we can approximate the errors of the effective mass by performing a jackknife analysis. We can also find a guess for the amplitude A_1 by forming the combination

$$A_{1,eff} = \frac{\overline{y}_t}{\cosh\left(m_{eff}(t)\left(T/2-t\right)\right)}. \tag{4.18}$$

With a bit of algebra, we can relax the assumption that the hyperbolic cosine is well approximated by a single decaying exponential. We define a three point effective mass by

$$\begin{aligned} m_{eff}^{3pt}(t) &= \operatorname{acosh}\left(\frac{C(t+1)+C(t-1)}{2C(t)}\right) \\ &= \operatorname{acosh}\left(\frac{A_1\cosh\left(M_1^a\left(T/2-t-1\right)\right)+A_1\cosh\left(M_1^a\left(T/2-t+1\right)\right)}{2A_1\cosh\left(M_1^a\left(T/2-t\right)\right)}\right) \\ &= \operatorname{acosh}\left(\frac{2\cosh\left(M_1^a\left(T/2-t\right)\right)\cosh\left(M_1^a\right)}{2\cosh\left(M_1^a\left(T/2-t\right)\right)}\right) \\ &= \operatorname{acosh}\left(\cosh\left(M_1^a\right)\right) \\ &= M_1^a. \end{aligned} \tag{4.19}$$

In deriving this, we made use of the identity $\cosh(a+b) = \cosh(a)\cosh(b)+\sinh(a)\sinh(b)$ to simplify the numerator in the second line of Eqn. 4.19. Once we have found $m_{eff}^{3pt}(t)$ using now $\overline{y}_t$, $\overline{y}_{t+1}$, and $\overline{y}_{t-1}$, we can find an estimate for A_1 again using Eqn. 4.18.

We can use this method directly in the case of the Goldstone boson $\gamma_5\Gamma_5$ meson. We demonstrate this for the Goldstone correlator in Figure 3.1, for which we discussed the results of non-linear fits in the previous section. The three point effective mass, as defined in Eqn. 4.19, is plotted in Figure 4.3. As a sanity check, we note that the effective mass agrees with the non-linearly fit mass as plotted in Figure 4.1, although it features larger errors than the non-linear fits. This is reasonable since an effective mass is a far more local definition of a global quantity than the non-linear fit result. It is for this reason that we prefer to cite results from direct fits to the correlator as opposed to the local effective mass results.

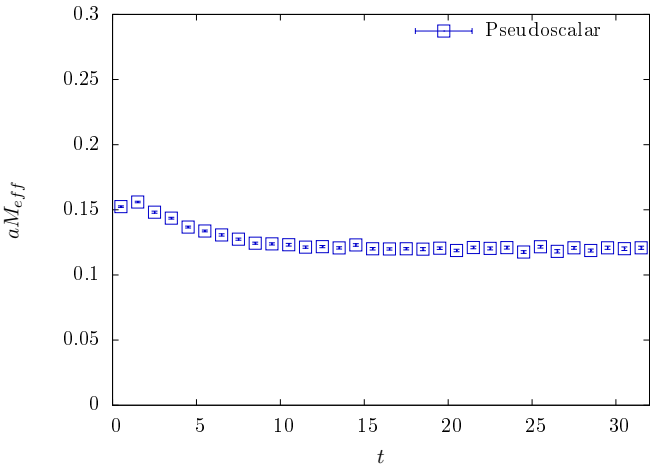

Figure 4.3. Example three point effective mass to a correlator without a parity partner. An example of a three point effective mass extracted from a correlator without a parity partner. The three point effective mass is defined in Eqn. 4.19, and is applied to the Goldstone boson $\gamma_5\Gamma_5$ meson state with a wall source. This example is from 1000 measurements on the $36^3 \times 64$, $m_\ell = 0.003$, $m_h = 0.080$ ensemble.

In its current form, the effective mass has been derived under the assumption that there is only one state contributing to the correlator. This is often not the case with staggered fermions since there is both the direct and the oscillating term. There are two potential routes to address this. The first route is analytically suppress either the direct or oscillating state as will be described in appendix C.2, which may be sufficient to use the effective mass equations defined above. As a remark, it may further help to replace the definitions of effective masses above to use, e.g., $t+2$ and $t-2$ instead of $t+1$ and $t-1$, respectively, to minimize bias by the partner state.

It is possible to generalize the definition of an effective mass for an arbitrary number of states. The details of this method are relegated to appendix C.1. We nonetheless use this method to find initial guesses for staggered correlator fits featuring a single direct and oscillating term. We remark that it can be difficult to extract excited states in the direct or the oscillating channel reliably using this method.

We demonstrate the result of a two state generalized effective mass calculation in Figure 4.4. These generalized effective masses are determined for the vector meson correlator in Figure 3.1. Again, the effective masses match well with the non-linear fit results in

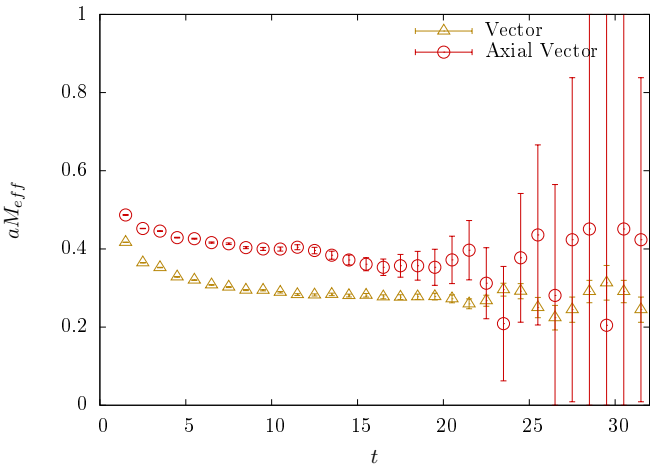

Figure 4.4. Example effective mass for the vector and axial vector. An example of using a generalized effective mass to extract initial guesses from a correlator with a parity partner. This effective mass assumes two states, and is applied to the vector $\gamma_3\gamma_4\Gamma_1\Gamma_5$ meson state (yellow), parity partner axial vector $\gamma_3\gamma_5\Gamma_1\Gamma_4$ meson (red) measured with a wall source. This example is from 1000 measurements on the $36^3 \times 64$, $m_\ell = 0.003$, $m_h = 0.080$ ensemble.

Figure 4.2. As expected, the effective mass results do feature larger statistical errors.

The effective mass used here does qualitatively show why we choose $t_{max} = 24$ for the non-linear fits. We see in Figure 4.4 that we cannot resolve the parity partner axial vector for larger values of t than 24, suggesting either that the oscillating state is exponentially suppressed compared to the direct state or that there is a strong contribution from noise making it unsuitable for fitting. In general, though, choosing t_{max} to be smaller or much larger should be inconsequential in extracting masses. It can, however, artificially inflate the χ^2/N_{dof} if we choose t_{max} too large, for the virtue that we are adding data so noisy that it could be well described by any functional form. For this reason it is important to chose t_{max} with some wisdom.

4.5 Building and Fitting the 0^{++}

4.5.1 Building the 0^{++} Correlator

Before fitting the 0^{++} correlator, we need to discuss building the disconnected piece from the operator measurements described in section 3.6.

Let us start with the operator $\mathcal{O}^n_{D,(i)}(t)$ defined below Eqn. 3.52 on a single configuration n. For a single pair of stochastic vectors i, j, we can build the non-vacuum subtracted part of Eqn. 3.51 in terms of $\mathcal{O}^n_{D,(i)}(t)$ and $\mathcal{O}^n_{D,(j)}(t)$ with

$$D^n_{(i,j)}(t) = \sum_{t_0} \mathcal{O}_{D,(i)}(t_0)\mathcal{O}_{D,(j)}(t+t_0), \tag{4.20}$$

where in this case we have taken advantage of the periodic boundary conditions.

This takes T^2 multiplications and sums on an $L^3 \times T$ lattice. As a point of efficiency, we can also perform this in $T \log T$ operations instead via a Fast Fourier Transform. For reference, our convention for the discrete Fourier transform will be

$$\mathcal{O}_{D,(i)}(t) = \frac{1}{T}\sum_{\omega} e^{i\omega t}\widetilde{\mathcal{O}}_{D,(i)}(\omega) \qquad\qquad \widetilde{\mathcal{O}}_{D,(i)}(\omega) = \sum_{t} e^{-i\omega t}\mathcal{O}_{D,(i)}(t) \tag{4.21}$$

For discussion in this chapter, a tilde above a quantity indicates a Fourier transform.

Since $\mathcal{O}_{D,(i)}(t)$ is real, $\widetilde{\mathcal{O}}^\dagger_{D,(i)}(\omega) = \widetilde{\mathcal{O}}_{D,(i)}(-\omega)$. Let us consider the inverse Fourier transform of the quantity $\widetilde{\mathcal{O}}^{n\dagger}_{D,(i)}(\omega)\widetilde{\mathcal{O}}^n_{D,(j)}(\omega)$.

$$\begin{aligned}
\frac{1}{T}\sum_{\omega} e^{i\omega t}\widetilde{\mathcal{O}}^{n\dagger}_{D,(i)}(\omega)\widetilde{\mathcal{O}}^n_{D,(j)}(\omega) &= \frac{1}{T}\sum_{\omega} e^{i\omega t}\widetilde{\mathcal{O}}^n_{D,(i)}(-\omega)\widetilde{\mathcal{O}}^n_{D,(j)}(\omega) \\
&= \frac{1}{T}\sum_{\omega} e^{i\omega t}\sum_{t_0} e^{-i(-\omega)t_0}\mathcal{O}^n_{D,(i)}(t_0)\sum_{t'} e^{-i\omega t'}\mathcal{O}^n_{D,(j)}(t') \\
&= \frac{1}{T}\sum_{\omega}\sum_{t_0}\sum_{t'} e^{i\omega(t+t_0-t')}\mathcal{O}^n_{D,(i)}(t_0)\mathcal{O}^n_{D,(j)}(t') \\
&= \frac{1}{T}\sum_{t_0}\sum_{t'}\left[\sum_{\omega} e^{i\omega(t+t_0-t')}\right]\mathcal{O}^n_{D,(i)}(t_0)\mathcal{O}^n_{D,(j)}(t') \\
&= \frac{1}{T}\sum_{t_0}\sum_{t'}\left[T\delta_{t+t_0,t'}\right]\mathcal{O}^n_{D,(i)}(t_0)\mathcal{O}^n_{D,(j)}(t') \\
&= \sum_{t_0}\mathcal{O}^n_{D,(i)}(t_0)\mathcal{O}_{D,(j)}(t_0+t).
\end{aligned} \tag{4.22}$$

We see that, through this method, we have reproduced Eqn. 4.20 above. We thus note

$$\widetilde{D}^n_{(i,j)}(\omega) \equiv \sum_t e^{-i\omega t} D^n_{(i,j)}(t) = \widetilde{\mathcal{O}}^{n\dagger}_{D,(i)}(\omega)\widetilde{\mathcal{O}}^n_{D,(j)}(\omega). \tag{4.23}$$

This gives us the ability to, on a configuration by configuration basis, build the quark line disconnected piece of the 0^{++} correlator efficiently by forming $D^n_{(i,j)}(t)$ for all combinations of i, j. Because we use timeslice dilution, this includes $i = j$ at all separations except $t = 0$. This gives us a slight boost compared to the connected case.

Up to an overall normalization, we can build the full Eqn. 3.51 via

$$D(t) = \lim_{N_i \to \infty} \frac{1}{N_i^2} \sum_{i,j=1}^{N_i} \left[\left\langle D^n_{(i,j)}(t) \right\rangle_{ens} - T \left\langle \mathcal{O}^n_{D,(i)} \right\rangle_{ens} \left\langle \mathcal{O}^n_{D,(j)} \right\rangle_{ens} \right]. \tag{4.24}$$

There are a few remarks to make about this expression, in particular the vacuum subtraction.

- The factor of T on the vacuum subtraction exists because we are summing as opposed to averaging over all possible t_0 in Eqn. 4.20.
- We do not have time coordinates attached to the vacuum subtraction because its ensemble average is time translation invariant.
- It *is* important that we subtract the expectation value for stochastic measurement (i) multiplied by the expectation value for measurement (j), as opposed to just taking the square of the expectation value averaged over all stochastic measurements. Doing the latter would inadvertently cause squaring of stochastic noise, which would not give an unbiased estimate for the square of the expectation value.

As an example of the quark line disconnected piece of the 0^{++} correlator in both momentum and position space we refer to Figure 4.5. On the left hand side, we have the momentum space correlator as defined in Eqn. 4.23 as a function of the momenta ω. In momentum space the correlator is peaked around zero momentum and is otherwise suppressed. As a remark, this figure is corrected for the vacuum subtraction which would otherwise manifest

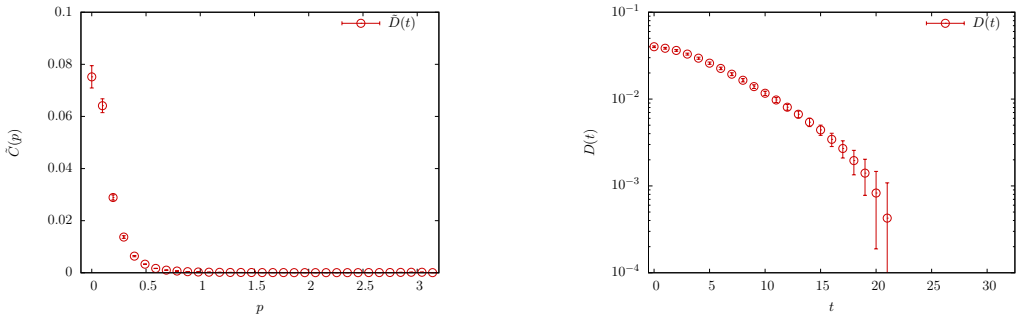

Figure 4.5. An example of $D(t)$ both in momentum and position space. Left: The momentum space disconnected correlator as defined in Eqn. 4.23 averaged over all stochastic noise sources, with the addition of the effect of the vacuum subtraction. Right: The equivalent position space correlator as defined in Eqn. 4.24. Both figures come from 1000 measurements on the $36^3 \times 64$ ensemble for $m_\ell = 0.003$, $m_h = 0.080$.

itself as a large additional delta function spike at $\omega = 0$. While we do not discuss it here, one method to perform the vacuum subtraction is by extrapolating the $\omega = 0$ dependence of the momentum space correlator from neighboring momentum values.

On the right hand side of Figure 4.5, we have the corresponding position space disconnected correlator. This is our first look at the quark-line disconnected correlator, and there are many important features to comment on in comparison to, for example, the Goldstone boson correlators featured in Figure 3.2.

- The quark-line disconnected piece of the 0^{++} correlator features *negative* curvature on a log plot for smaller values of t. This is a result of the quark-line disconnected correlator containing states with negative amplitudes, as parameterized in Eqn. 3.56. In contrast, the Goldstone boson correlator only contains states of positive amplitude. We will see later that the full 0^{++} correlator also features positivity.

- The correlator, as plotted, "disappears" for $t \gtrsim 21$. This issue is not the result of physics, but stems from having insufficient statistics to resolve the vacuum subtraction. This issue will be the focus of most of our forthcoming discussion.

- The correlator does not appear to have a region that is a straight line on a log plot, corresponding to a single state dominating. This issue is exasperated by the issue

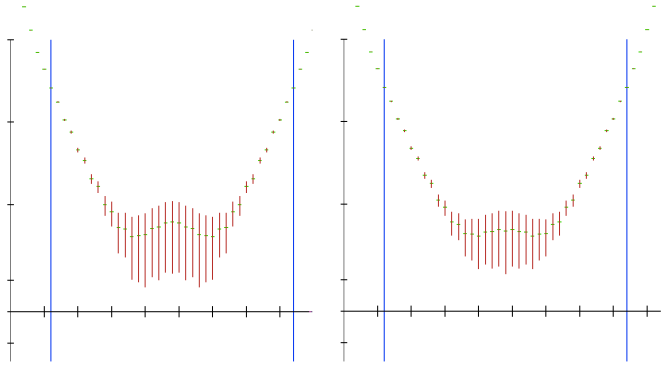

Figure 4.6. An evaluation of the benefits of measuring more frequently than the autocorrelation. An evaluation of the benefits of measuring more frequently than the autocorrelation. Left: Measurement of $S(t)$ every 20 MDTU. Right: Measurement of $S(t)$ every 10 MDTU. Error bars are not corrected for autocorrelation. This comes from 20000 MDTU of measurements on the $24^3 \times 48$ ensemble for $m_\ell = 0.015$, $m_h = 0.080$.

with the vacuum subtraction.

It is important to note that an important subtlety can come in if there is autocorrelation between the measurements of $\mathcal{O}_{D,(i)}$. When building $D(t)$ as described in Eqn. 4.24, it is important to *first* build $D^n_{(i,j)}(t)$ on a configuration by configuration basis from unbinned operators, *then* bin both $D^n_{(i,j)}(t)$ and $\mathcal{O}_{D,(i)}$, *then* form the correlator as defined. This order is important because $D^n_{(i,j)}(t)$ is a base quantity with meaning on a single configuration, not a derived ensemble quantity such as the Goldstone mass. As a note, when forming Eqn. 3.53, the connected piece, Eqn. 3.49, must be binned with the same frequency as the disconnected piece.

Due to the vacuum subtraction, it is difficult to estimate the autocorrelation of the 0^{++} correlator. It is also non-trivial to use `UWerr` to estimate the autocorrelation, as discussed in section 4.2. Instead, we take the autocorrelation of the chiral condensate as an estimate for the autocorrelation of the quark-line disconnected correlator. Since we estimate the 0^{++} correlator stochastically, we can ask if there is a benefit to measuring more frequently than the autocorrelation.

We address this question via a study plotted in Figure 4.6. The left hand side features

the full 0^{++} correlator, $S(t)$, measured every 20 MDTU, while the right hand side is measured every 10 MDTU, or twice as frequently along the HMC. The autocorrelation of the chiral condensate as measured by `UWerr` is 40 MDTU for this ensemble, larger than the measurement frequency in both cases. We note, qualitatively, that both the left and the right hand side correlators have the same qualitative shape featuring a fluctuation in the center which will be a point of comment later. These measurements are unbinned such that we expect the right hand side to have error bars a factor of $\sqrt{2}$ smaller than the left hand side. Since this appears to be the case, we do not expect there to be a benefit from measuring more frequently than the autocorrelation.

This study, more subtly, tests that using only 6 stochastic sources per configuration is sufficient. On each of the two configurations, we use 6 unique stochastic sources. If the two configurations are equivalent with respect to gauge fluctuations due to autocorrelation, measuring on both configurations instead of one is approximately equal to using twice as many noise sources on only one configuration. The statement that measuring more frequently than the autocorrelation offers no benefit is equivalent to saying that gauge fluctuations dominate the noise from using stochastic sources.

We are now ready to discuss analyzing and fitting the 0^{++} correlator.

4.5.2 Analyzing the 0^{++} Correlator

As we saw in Figures 4.5 and 4.6, the quark-line disconnected piece of the 0^{++} correlator introduces difficulties not present in other measurements, which results from our inability to resolve the vacuum subtraction with sufficient statistical accuracy. For example, on the $36^3 \times 64$ ensemble with $m_\ell = 0.003, m_h = 0.080$, the vacuum subtraction portion of Eqn. 4.24 has a magnitude and statistical error, corrected for autocorrelation, of 28.380(70). As can be confirmed in Figure 4.5, the signal of the correlator after the vacuum subtraction is of similar or smaller order of magnitude than the error of the vacuum subtraction. It should not be surprising that the vacuum subtraction is not sufficiently accurate.

There is an even deeper issue here: there are situations where the vacuum subtraction

can lead to a plot of $D(t)$ looking just as good as plot of the Goldstone boson, only by coincidence. It is misleading to assume that we can trust the vacuum subtraction in this case, even if it qualitatively looks good, as a small incorrect vacuum subtraction can bias the extraction of the 0^{++}.

There are multiple potential solutions to this issue. One solution is to boost statistics until the vacuum subtraction is sufficiently resolved. In light of Figure 4.5, we would need reduce the error on the vacuum by at least a factor of 100. Since the error drops with the square root of the number of measurements, we would need to increase the number of measurements by a factor of 10^4 which would be prohibitively expensive.

With this in mind, we must pursue alternative solutions to the issue of addressing the vacuum subtraction. Each of these methods hinge on one observation: no matter how large the error on the vacuum subtraction is, it still always contributes as an extra constant to the correlator. To account for the extra constant, we can parameterize $D(t)$ or equivalently $S(t)$ as

$$S_{vev}(t) = A_{0^{++}} \cosh\left(M_{0^{++}}\left(T/2 - t\right)\right) + V, \tag{4.25}$$

where the additional $+V$ parameterizes the additional constant. We have assumed and will demonstrate later that the oscillating partner is negligible. For discussion, we list a few methods to address this issue of the extra constant.

1. Ignore the additional constant in the data and fit the correlator assuming a single hyperbolic cosine.

   For sufficiently small separations t, the extra constant is exponentially small compared to the hyperbolic cosine term, and thus can be neglected. In practice, for values of t where the constant is exponentially suppressed, excited state contamination is too large. For the $D(t)$ correlator, the excited state contamination is due to the negative amplitude a_0 isomultiplet state.

For the $S(t)$ correlator, the excited state contamination comes from higher energy resonances, and more importantly that any and all two particle states with equal and opposite momentum and other quantum numbers will couple to the 0^{++} channel.

For these reasons, we cannot ignore the vacuum subtraction.

2. As a modification, [37] advocated looking at the shifted correlators

This corresponds to looking at

$$\begin{aligned} \tilde{D}(t) &= D(t) - D(T/2), \\ \tilde{S}(t) &= S(t) - S(T/2), \end{aligned} \tag{4.26}$$

where the notation of a tilde is taken from [37] and is not to be confused with a Fourier transform. This data is then fit to the appropriate modification to Eqn. 4.25,

$$\tilde{S}_{vev}(t) = S_{vev}(t) - S_{vev}(T/2) = A_{0^{++}} \left(\cosh \left(M_{0^{++}} \left(T/2 - t \right) \right) - 1 \right), \tag{4.27}$$

where we most note that the contribution of the vacuum explicitly cancels. Since the correlator is zero by construction at $t = T/2$, this is known as the "zero shift."

A few important considerations must go into this. We are implicitly assuming that we trust the measured value of $D(t)$ or $S(t)$ at the center of the correlator (independent of the vacuum), which is where the relative error is the largest. More importantly, the absolute error on the correlator is not exponentially suppressed at the center compared to other parts of the correlator. Subtracting the center can contaminates other time separations with additional noise, boosting the error by another factor of $\sqrt{2}$. As a last subtlety, the correlator by definition has zero error at the center because we zero the center of the correlator on a configuration-by-configuration basis. It is meaningless to include the zero data point at the center in a fit, and because the correlator is correlated with itself, it is also meaningless to include nearby time separations. We

arrive at the same problem as before: fits to the zero-shifted correlator should not include points close to the center of the correlator, leaving us with only timeslices contaminated by excited state effects.

3. Instead of performing a zero subtraction, fit the original vacuum subtracted correlator including the constant to the fit form in Eqn. 4.25.

   This form is convenient for a few reasons. First, the free constant allows us to avoid the issue of the vacuum subtraction. The constant also allows us an additional consistency check in the fit. Under a jackknife error the free constant should be consistent with zero, and an inconsistency is a sign that our fit ansatz is not correct, for example due to excited state contamination.

In practice, we use fits with a free constant but with one modification: we fit the finite differences instead. As proven in appendix C.2, the use of a finite difference fit is equivalent to the use of a fit with an extra constant, however a finite difference fit is more numerically stable because it includes one less free parameter.

There is a further qualitative benefit to looking at finite differences: it is easier to plot and visually inspect the finite differences of a correlator. The extra unresolved constant impedes our ability to visualize the correlator on a log plot as noted in Figure 4.5.

Before fitting the 0^{++} mass, we remark on one further analytic modification we perform on the correlator. Both [35] and [37] note, empirically, that the parity partner state contributes negligibly to $D(t)$ and weakly to $S(t)$. Instead of attempting to fit the oscillating state, we perform a positive parity projection as described in appendix C.2, before calculating the finite differences and only fit the 0^{++} state.

4.5.3 Fitting the 0^{++}

As a platform to discuss fitting the 0^{++} correlator, we will refer to one of our high quality ensembles, the $36^3 \times 64$, $m_\ell = 0.003, m_h = 0.080$ ensemble. We will use the fit form

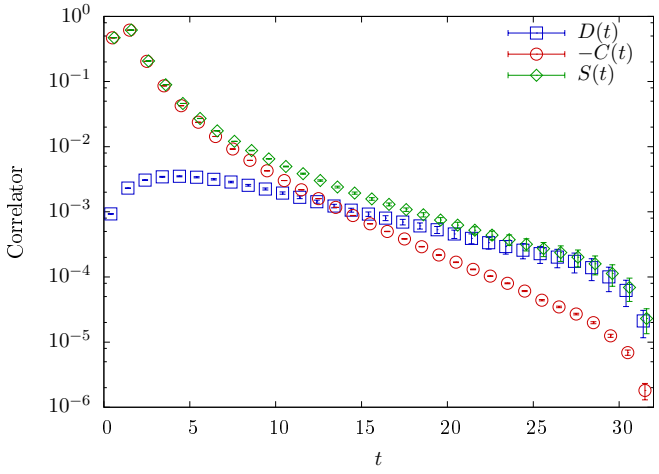

Figure 4.7. A representative plot of the components of the 0^{++} correlator. This is a representative plot of the quark-line connected ($-C(t)$, in red) and disconnected ($D(t)$, in blue) pieces of the full 0^{++} correlator ($S(t)$, in green) from a good quality ensemble. This plot shows all three correlators with both positive parity projection and finite differences, as described in appendix C.2. This comes from 1000 measurements on the $36^3 \times 64$ ensemble for $m_\ell = 0.003$, $m_h = 0.080$.

$$S'(t) = 2A_{0^{++}} \sinh\left(\frac{M_{0^{++}}}{2}\right) \sinh\left(M_{0^{++}}\left(T/2 - t\right)\right), \tag{4.28}$$

which follows from appendix C.2, noting our use of positive parity projection and finite differences. In practice, we will define

$$A^*_{0^{++}} \equiv 2A_{0^{++}} \sinh\left(\frac{M_{0^{++}}}{2}\right), \tag{4.29}$$

to simplify the fitting procedure. and calculate $A_{0^{++}}$ in post-processing.

We will begin by looking at Figure 4.7 which shows the positive parity projected, finite differences of the quark line connected piece, Eqn. 3.49, quark line disconnected piece, Eqn. 3.51, and the full correlator, Eqn. 3.53. There are several remarks to make about this plot.

- All three correlators feature a sharp downward turn for $t \approx T/2 = 32$. This is because the finite difference of a correlator is an odd function with respect to the center, which follows from the original correlator being an even function with respect to the center.

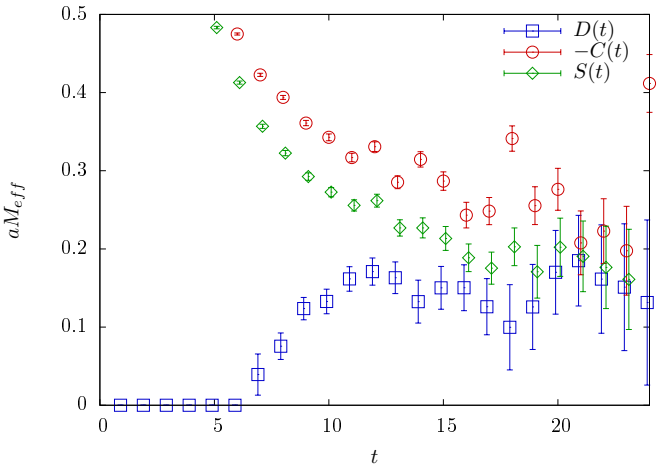

Figure 4.8. An effective mass plot for the components of the 0^{++} correlator. A three point effective mass plot for the quark-line connected ($-C(t)$, in red) and disconnected ($D(t)$, in blue) pieces of the full 0^{++} correlator ($S(t)$, in green) from a good quality ensemble. These effective masses were calculated from the correlators plotted in Figure 4.7, with colors matching respectively. This comes from 1000 measurements on the $36^3 \times 64$ ensemble for $m_\ell = 0.003$, $m_h = 0.080$.

- For larger t, $D(t) > -C(t)$. This is a qualitative proof that the quark-line disconnected piece couples to a lighter state than the quark-line connected piece. Therefore the mass of the 0^{++} singlet is smaller than the mass of the isomultiplet a_0 meson. This also supports looking at just the disconnected correlator, $D(t)$: for large t, the heavier a_0 will be exponentially suppressed.

- For smaller t, $D(t) < -C(t)$. This is not surprising since $-C(t)$ couples only to positive amplitude states, unlike $D(t)$.

- Combining these observations, we note $S(t)$ follows the behavior of $D(t)$ for larger t, of $-C(t)$ for smaller t, and smoothly interpolates between both correlators where a crossover occurs for $t \approx 13$.

- Qualitatively, $D(t)$ is a straight line on a log plot for $t \in [10, 25]$. This suggests that, on this interval, $D(t)$ couples to only one state above noise.

In light of the last point in this list, it is instructive to look at an effective mass for $D(t)$.

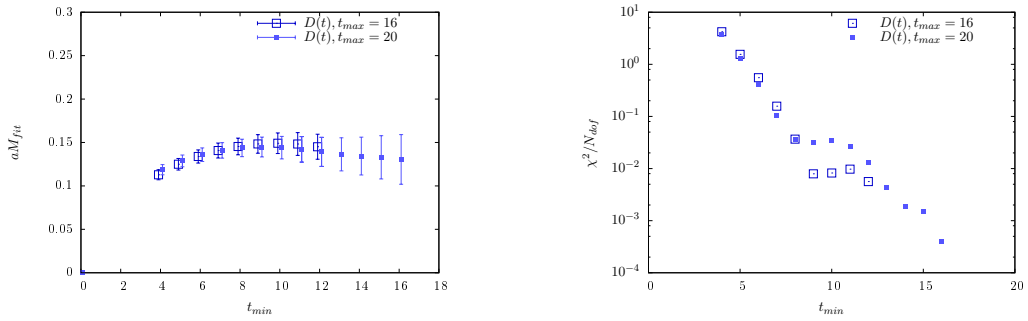

Figure 4.9. Example uncorrelated single state fits to a 0^{++} correlator. Left: An example of the extracted $M_{0^{++}}$ from uncorrelated, positive parity projected, uncorrelated fits from varying t_{min} to two fixed values of t_{max}. Right: The χ^2/N_{dof} for these fits. Because these fits are uncorrelated, the χ^2/N_{dof} tends to artificially be very small, instead of $\mathcal{O}(1)$ for a good fit. Both are extracted from 1000 measurements on the $36^3 \times 64$ ensemble for $m_\ell = 0.003$, $m_h = 0.080$.

For completeness, we show the effective mass for the quark-line connected, disconnected, and full 0^{++} correlator in Figure 4.8.

There is a visible, albeit noisy, plateau in the disconnected correlator which extends for $t \gtrsim 11$ in the effective mass for $D(t)$, suggesting a mass between 0.1 and 0.2. As a consistency check, we see that $S(t)$ is consistent for larger t as expected since $D(t)$ and $S(t)$ asymptotically agree for large t in the correlator plot in Figure 4.7. As t decreases, the effective mass from $S(t)$ increases due to excited state contamination *before* $D(t)$ begins to decrease due to negative amplitude contributions from the a_0. This is equivalent to the note that $D(t)$ has a longer "straight line" region in the correlator log plot.

We are now ready to begin discussing fitting the 0^{++}. At this point, we perform *uncorrelated* fits to just $D(t)$ to extract the mass of the 0^{++} scalar meson. The use of positive parity projection and finite differences greatly correlates the values of $D(t)$, resulting in an ill-conditioned covariance matrix. In the future it would be interesting to study the use of PCA analysis to stabilize the fit as described in [37].

We show the results of fitting $D(t)$ from variable t_{min} to two fixed values of t_{max} for the $36^3 \times 64$, $m_\ell = 0.003, m_h = 0.080$ ensemble in the left hand side of Figure 4.9. The errors are defined via single elimination jackknife after binning. We see that these fit results are

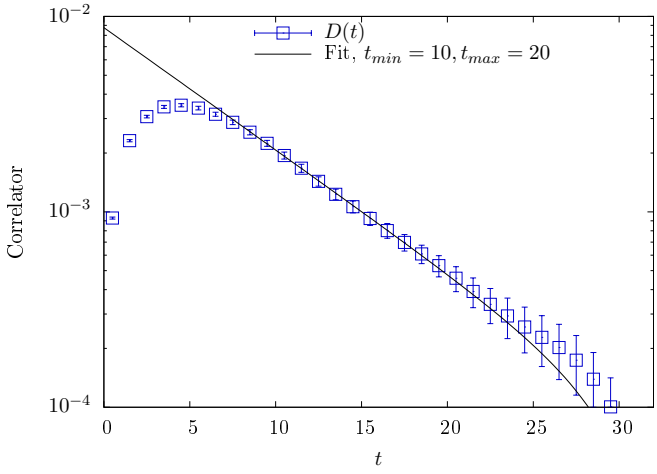

Figure 4.10. A representative plot of $D(t)$ correlator with a fit curve overlaid. The positive parity projected, finite differenced $D(t)$ correlator with a fit curve overlaid from the interval $10 \leq t \leq 20$. We note that the curve fits the data well on the interval, as well as outside of the interval, within error bars. This comes from 1000 measurements on the $36^3 \times 64$ ensemble for $m_\ell = 0.003$, $m_h = 0.080$.

stable independent of the choice of t_{max}. Further, the fits are rather independent of t_{min} up until $t \lesssim 7$, where they begin to dip. This coincides well with the onset of curvature in the correlator log plot of Figure 4.7. We remark that downward curvature sets in for larger t in the effective mass plot, Figure 4.8, which we interpret as an artifact of the non-locality of the effective mass after using positive parity projection and taking a finite difference.

On the right, we have plotted the χ^2/N_{dof} for reference. As expected, uncorrelated fits predict a very small $\chi^2/N_{dof} \ll 1$. This supports it being unreasonable to look at the p-value, as the χ^2 statistic is meaningless. Nonetheless, the χ^2/N_{dof} is still a useful indication of if a fit is very poor. For values of $t_{min} < 5$, it becomes larger than 1 and continues rising in stride with $D(t)$ beginning to show curvature.

Because we cannot trust the χ^2/N_{dof} for larger values of t_{min}, it is of utmost importance to visually inspect any fit curve. A sample fit is shown in Figure 4.10. The choice of $t_{min} = 10$ was made because it agrees well with neighboring choices of t_{min} while still being separated from the onset of downward curvature for $t_{min} \lesssim 7$. Since the fit does not depend strongly on t_{max}, we chose the larger value of 20. We note that the curve fits the data well within the fit interval as well as for time separations outside of the fit interval.

The latter point is an important consistency check since the fit should be stable with respect to small changes in t_{min} and t_{max}. We note that there is some bias for the fit curve to lie below the correlator for $t > t_{max}$, but this is not concerning because of the large error bars and the use of an uncorrelated fit.

For the $36^3 \times 64, m_\ell = 0.003, m_h = 0.080$, we prefer a value for $aM_{0^{++}}$ of 0.145(16), where the error is statistical with a slight inflation to reflect the slight variation in the fit mass with respect to the choice of t_{min} and t_{max}.

4.5.4 Fitting the 0^{++}: A Poor Ensemble

After a long discussion of the difficulties and choices that are made when fitting the 0^{++} on a "good" ensemble, it helps to get a context for the features of a low quality ensemble. As an example, we will look at the $32^3 \times 64$ ensemble with $m_\ell = 0.010, m_h = 0.080$. Unlike the $36^3 \times 64, m_\ell = 0.003, m_h = 0.080$ ensemble, with 333 independent measurements after correcting for autocorrelation, the $32^3, m_\ell = 0.010, m_h = 0.080$ ensemble includes only 188 independent measurements.

Since, we expect the light meson masses to depend on the light fermion mass, this is not an apples-to-apples comparison. We expect the 0^{++} to have a heavier mass on this ensemble compared to the $m_\ell = 0.003$ ensemble. Since we extract the mass from a signal which decays exponentially in the mass with t, we expect to have fewer reliable values of t in the correlator compared to the $m_\ell = 0.003$ even if statistics were equal.

As a point of comparison, we show the quark line connected, disconnected, and full 0^{++} correlator for the $m_\ell = 0.010$ ensemble in Figure 4.11. There are several remarks to make on this correlator.

- The quark-line connected correlator, $-C(t)$, has a consistent shape over the entire range of t. In general, $-C(t)$ is always well resolved with respect to statistics.
- The quark-line disconnected correlator, $D(t)$, shows strange fluctuations for $t \gtrsim 13$. In particular, it qualitatively dips for $t \approx 15$, back up for $t \approx 18$, and loses any physically

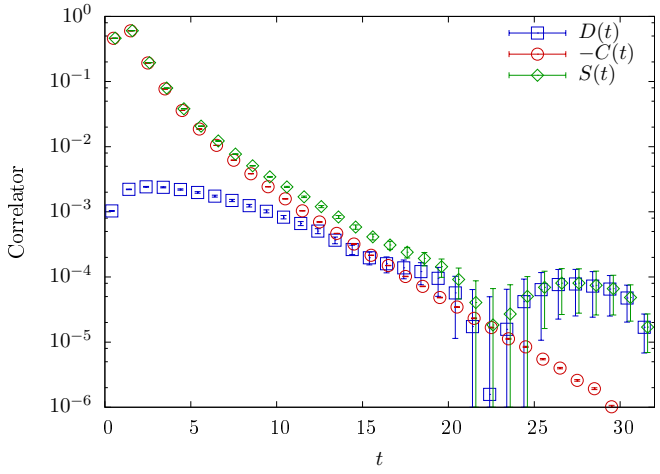

Figure 4.11. A representative plot of the components of the 0^{++} correlator for an ensemble deemed poor. This is a representative plot of the quark-line connected ($-C(t)$, in red) and disconnected ($D(t)$, in blue) pieces of the full 0^{++} correlator ($S(t)$, in green) from a poor quality ensemble. This plot shows all three correlators with both positive parity projection and finite differences, as described in appendix C.2. This comes from 750 measurements on the $32^3 \times 64$ ensemble for $m_\ell = 0.010$, $m_h = 0.080$.

justifiable shape for $t > 20$.

- As noted with Figure 4.7, the quark-line connected piece $-C(t)$ dominates for smaller t. For larger t, we argue with caution that $D(t)$ dominates. This is supported by $D(t)$ having a smaller slope on a log plot than $-C(t)$ on a more trustworthy interval, such as for $t \in [7, 10]$. This implies the mass of the 0^{++} is still smaller than the mass of the isomultiplet a_0 meson on this ensemble.

The very poor quality of the quark-line disconnected correlator in Figure 4.11 does prompt an important question: is the strange shape of the correlator just a fluctuation of poor statistics, or is there an issue of physics on this ensemble?

To begin to study this question, we turn to Figure 4.12 where we look again at the quark line disconnected piece, $D(t)$, from the good quality $36^3 \times 64$, $m_\ell = 0.003, m_h = 0.080$ ensemble. Instead of looking at it with the full statistics, however, we separately plot $D(t)$ built from the first one-fifth, second one-fifth, etc, of the data with no overlap. After partitioning the data, we have binned each partition with the autocorrelation size of 3

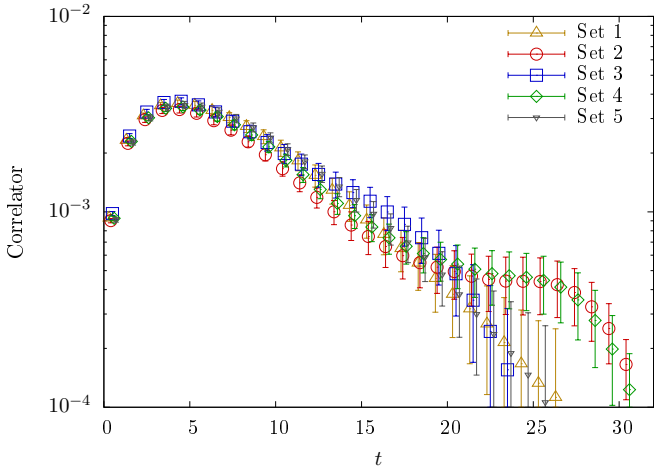

Figure 4.12. A plot of the quark line disconnected piece of the 0^{++} correlator subdivided over fifths of the full statistics. A plot of the quark line disconnected piece of the 0^{++} correlator, where each color corresponds to using the first, second, etc 20% of the full statistics. This comes from a total of 1000 measurements on the $36^3 \times 64$ ensemble for $m_\ell = 0.003$, $m_h = 0.080$.

determined from the full dataset. Each curve is thus constructed from 66 independent measurements.

As a positive note, all correlators agree rather well for $t \lesssim 5$ and within one standard deviation for $t \lesssim 10$. Unfortunately, this regime is also where excited state contamination is significant, so resolving the correlator well here does not benefit us with our current fitting methods.

Beyond this note, we can identify several worrying behaviors between the different datasets.

- If we look at Sets 1 and 5, in yellow and gray respectively, the correlator follows a straight trajectory, until developing a kink for $t \approx 20$, and falling more steeply before the correlator goes negative. We do not expect their similar behavior to be a consequence of long range autocorrelation since Sets 1 and 5 are well separated.

- If we look at Sets 2 and 4, in red and green respectively, we see that the correlators fall more steeply than the other datasets for $10 \lesssim t \lesssim 17$ and then effectively flatten out for $21 \lesssim t \lesssim 25$. This can be interpreted as a heavy and then near massless state

depending on the interval in question. Again, we do not expect the similarity between these sets to be the result of long range autocorrelation.

- If we look at Set 3, in blue, we see that the correlator falls the most slowly for smaller t, then smoothly transitions to falling more sharply and becoming negative for $t \approx 23$. Interesting, the correlator that would imply the smallest mass for the 0^{++} shows the most drastic change in behavior for large t.

Despite all five divisions of the data qualitatively featuring worrisome behavior, the combined correlator from the full set of data looks reasonable. This is both exciting and worrying. On one hand, this suggests that the strange fluctuations in smaller data sets are statistical in nature and therefore can be addressed by boosting statistics. On the other hand, some low statistics subsets qualitatively appear to be of high quality, and by extension the correlator in Figure 4.7 could be another coincidence. We take the, perhaps optimistic perspective, that because the different correlators in Figure 4.12 are well distributed around the correlator from the full data, this full set should well reflect the true nature of the quark-line disconnected 0^{++} correlator. This would suggest 250 to 300 independent measurements as a good benchmark for a trustworthy dataset. We caution, again, that this may depend heavily on the mass of the 0^{++} itself, and do not take it as a hard rule.

We have outlined and studied in this section a sound method to fit and check the quality of the fit to the quark line disconnected 0^{++} correlator. Emphasis has been given to a visual inspection both to the correlator and to a preferred fit in question, along with confirming relative independence of the results with respect to the choice of t_{min} and t_{max}. In cases where the correlator is not of high quality, we make conservative estimates of the mass from the available data, and in some cases we are making ongoing efforts to boost statistics to attempt to extract more reliable estimates of the 0^{++} mass.

We overview this, as well as results from the full quark line connected spectrum, in the following section.

4.6 Discussion of Results

We have performed spectrum measurements for a wide range of the parameter space of volume, bare m_ℓ, and bare m_h. The results to date of this study are summarized in Table 4.1. Both configuration generation and measurements are ongoing for some ensembles. Before discussing the overall picture of the spectrum, we comment on finite volume effects.

We asserted in section 1.5 that the condition $M_\pi L > 4.5$ produces sufficiently small finite volume effects in the fermionic sector. To justify this *ad hoc* assumption, we look at two different light/heavy fermion mass pairs on two different volumes.

First, we consider the parameter pair $m_\ell = 0.010, m_h = 0.080$ on 24^3 and 32^3 spatial volumes. On the 24^3 spatial volume, the Goldstone boson mass is $aM_\pi = 0.22236(13)$, such that $M_\pi L \approx 5.34$. On the 32^3 spatial volume, the mass is $aM_\pi = 0.22079(10)$, such that $M_\pi L \approx 7.07$. We consider the mass difference to be negligible because it is below 1%. Since $M_\pi L$ is larger than 4.5 on the 24^3 volume, this behavior is consistent with our *ad hoc* bound.

In contrast, we consider the pair $m_\ell = 0.005, m_h = 0.060$ on 24^3 and 32^3 spatial volumes. The bare Goldstone masses are $aM_\pi = 0.1628(10)$ and $= 0.14382(28)$, respectively, showing a 13% difference we attribute to finite volume. On the 24^3 volume, $M_\pi L \approx 3.91$. As expected, finite volume effects are large because $M_\pi L < 4.5$. As a passing remark, we note that finite volume effects give a positive shift to the mass of the Goldstone.

Going forward, we will only discuss spectral results from ensembles that are independent of finite volume effects. We will also rescale all bare mass quantities into physical units via the Wilson flow scale $\sqrt{8\tilde{t}_0}$. In section 2.5 we demonstrated that the lattice scale depends heavily on m_ℓ and m_h, making the conversion to physical units necessary for a reasonable comparison between ensembles.

In Figure 4.13, we show the Goldstone boson and vector meson mass in physical units. Different colors correspond to different bare values of am_h. The fit lines are only meant to guide the eyes and do not correspond to formal chiral extrapolations. These fit lines are

am_h	am_ℓ	L	T	# MDTU	N_{meas}/bin	aM_π	aM_ρ	$aM_{0^{++}}$
0.050	0.005	48	96	1321	52/2	0.13541(33)	0.2313(23)	—
0.050	0.005	32	64	10101	506/5	0.14015(47)	0.2503(15)	0.150(50)
0.050	0.010	48	96	1061	50/2	0.19592(25)	0.2874(14)	—
0.050	0.010	32	64	10051	502/3	0.19673(24)	0.2912(11)	0.320(20)
0.050	0.010	24	48	10101	504/5	0.20812(84)	0.3114(31)	—
0.050	0.015	32	64	10051	502/3	0.24675(17)	0.34147(84)	0.350(20)
0.050	0.015	24	48	10001	500/3	0.25062(47)	0.3505(12)	—
0.060	0.003	48	96	1381	147/2	0.10867(16)	0.2189(53)	—
0.060	0.005	32	64	15071	750/5	0.14382(28)	0.2624(20)	0.190(30)
0.060	0.005	24	48	10001	500/4	0.1628(10)	0.2994(31)	0.190(30)
0.060	0.010	32	64	15001	750/4	0.20522(14)	0.3167(14)	0.215(20)
0.060	0.010	24	48	20001	1000/3	0.20940(37)	0.3312(14)	0.215(20)
0.060	0.015	24	48	40701	2005/2	0.25812(15)	0.37551(71)	0.240(30)
0.060	0.025	24	48	20151	1004/2	0.34133(16)	0.45737(51)	0.350(50)
0.080	0.003	36	64	20282	1014/3	0.119936(99)	0.2779(27)	0.145(16)
0.080	0.003	32	64	10051	500/2	0.12118(17)	0.2918(37)	0.180(30)
0.080	0.005	32	64	20031	1000/2	0.15505(11)	0.3122(16)	0.208(21)
0.080	0.005	24	48	20051	1000/3	0.15983(29)	0.3306(28)	0.200(30)
0.080	0.010	32	64	10101	506/2	0.22079(10)	0.3757(10)	0.280(20)
0.080	0.010	24	48	40021	2000/2	0.22236(13)	0.38178(86)	0.238(15)
0.080	0.015	24	48	40161	2000/2	0.27459(10)	0.43251(68)	0.316(15)
0.080	0.025	24	48	20101	1000/2	0.36145(10)	0.52018(54)	0.400(50)
0.100	0.005	32	64	1521	119/2	0.16631(19)	0.3731(46)	—
0.100	0.005	24	48	10051	500/2	0.16827(20)	0.3859(43)	0.320(30)
0.100	0.010	32	64	1561	141/2	0.23639(16)	0.4424(25)	—
0.100	0.010	24	48	20001	1000/2	0.23693(11)	0.4461(12)	0.400(30)
0.100	0.015	24	48	10001	500/2	0.29158(15)	0.4952(28)	0.470(30)
0.100	0.025	24	48	10101	500/2	0.38113(11)	0.5966(13)	—
0.040	0.035	24	48	10081	500/2	0.38982(25)	0.47183(61)	—
0.050	0.035	24	48	10591	500/1	0.40160(19)	0.50047(53)	—
0.060	0.035	24	48	10531	500/2	0.41302(18)	0.53270(75)	—
0.080	0.035	24	48	10201	500/2	0.43547(13)	0.6055(16)	—
0.100	0.035	24	48	10261	500/1	0.456189(96)	0.68374(97)	—

Table 4.1. An overview table listing all ensembles and measured spectral quantities. A listing of all 4+8 model ensembles noted in Figure 1.2. For each ensemble, we list the bare mass of the Goldstone boson, M_π, of the vector meson, M_ρ, and where available, the 0^{++} meson, $M_{0^{++}}$. In all cases measurements are performed every 20 MDTU.

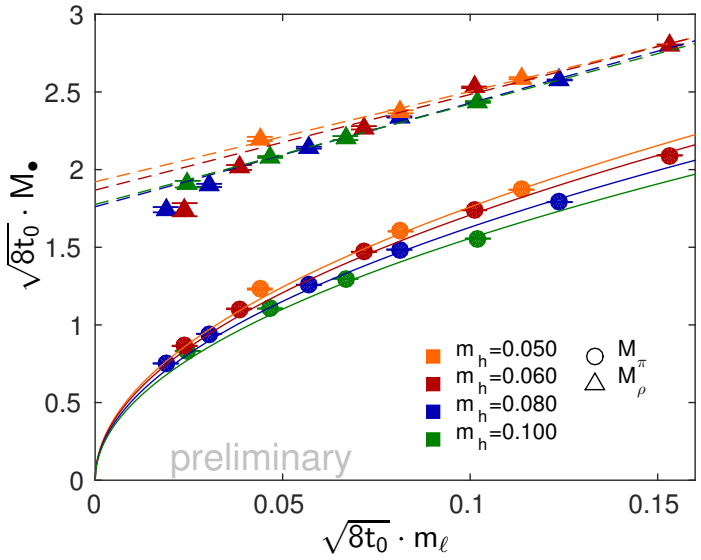

Figure 4.13. The Goldstone boson and the vector meson across different values of m_h. The mass of the Goldstone boson and the vector meson across different values of m_ℓ and m_h in physical units. We see that both quantities share similar behavior as a function of $\sqrt{8\tilde{t}_0}m_\ell$, indicative of IR behavior independent of m_h in this sector. Fit lines follow leading order chiral perturbation theory predictions and serve only to guide the eyes.

parameterized as

$$M_\rho(m_\ell) = M_\rho(m_\ell = 0) + cm_\ell, \tag{4.30}$$

$$M_\pi(m_\ell) \propto \sqrt{m_\ell}, \tag{4.31}$$

which follows from leading order chiral perturbation theory.

The Goldstone boson and the vector meson follow a similar curve independent of m_h. We emphasize that proper scale setting was essential to find this behavior. The behaviors of the Goldstone and the vector as a function of m_ℓ are well described by a chiral perturbation theory ansatz. We take this as supporting evidence that the 4+8 model is chirally broken and features an isomultiplet spectrum that is independent of m_h. Put differently, the Goldstone and the vector are not influenced by the slow running noted in section 2.6 in a statistically significant manor.

The ratio of the vector mass to the Goldstone mass is an additional check for chirally

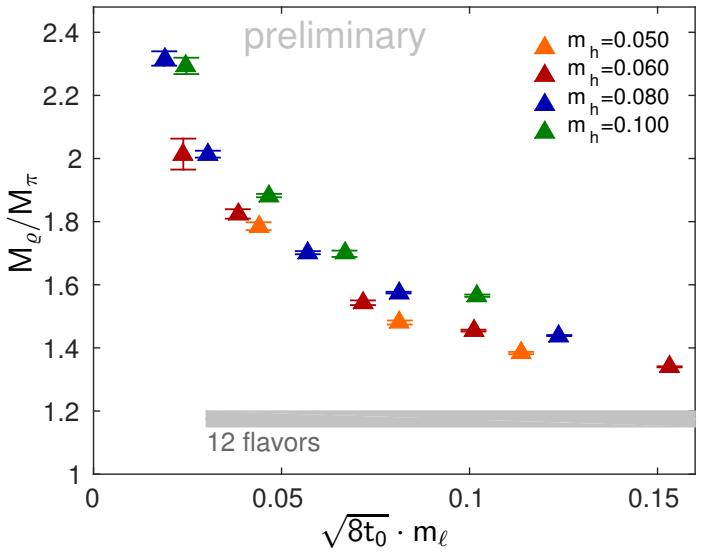

Figure 4.14. The ratio of the vector meson mass to the Goldstone boson mass across different values of m_h. The ratio of the vector meson mass to the Goldstone boson mass across different values of m_ℓ and m_h. We see that the ratio appears divergent as m_ℓ decreases, indicative of chiral symmetry breaking, independent of the value of m_h. The 12 fermion result is taken from [32].

broken behavior. Due to Goldstone's theorem, this ratio should diverge as the light fermion mass goes to zero. Another possibility is that we are in a mass deformed conformal phase. In this case, the mass of all dimensionful quantities follows hyperscaling behavior,

$$M_\bullet(m_\ell) \propto c_\bullet m_\ell \left(\frac{m_\ell}{\Lambda}\right)^{-\frac{\gamma_m^*}{1+\gamma_m^*}}, \tag{4.32}$$

where γ_m^* is the mass anomalous dimension at the IR fixed point [44], and Λ is an arbitrary scale introduced to maintain appropriate dimensionality. The ratio of two massive quantities should be equivalently constant independent of the light fermion mass deformation up to finite volume corrections to scaling [32].

The ratio of the vector mass to the Goldstone mass is plotted for each m_h in Figure 4.14. We note a clear divergent behavior as the physical light fermion mass decreases, consistent with chirally broken behavior. This divergence is in contrast to the constant ratio observed for the mass deformed 12 fermion theory, shown in a gray band.

For larger physical m_ℓ, the ratio of the vector meson to the Goldstone boson approaches

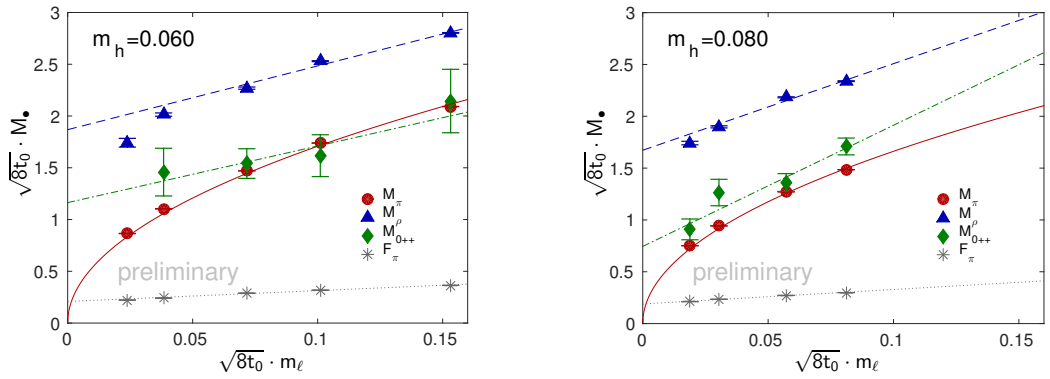

Figure 4.15. The Goldstone boson, vector meson, pseudoscalar decay constant, and isosinglet 0^{++} meson mass for two values of m_h. The mass of the Goldstone boson, vector meson, pseudoscalar decay constant, and isosinglet 0^{++} meson as a function of m_ℓ in physical units for $m_h = 0.060$ (left) and $m_h = 0.080$ (right). Fit lines follow leading order chiral perturbation theory predictions and serve only to guide the eyes.

the 12 fermion result. While we are not interested in this result for chiral light fermion physics in the 4+8 model, it does serve as a consistency check on our simulations. We expect that we will reproduce the 12 fermion mass-deformed results as we increase m_ℓ towards m_h.

In conclusion, the Goldstone boson and the vector meson are consistent with chiral symmetry breaking independent of the heavy fermion mass m_h over the measured range of m_ℓ. Further, the light fermion chiral limit of the vector meson is qualitatively independent of the heavy fermion mass.

We will now introduce measurements of the isosinglet 0^{++} meson. It is natural to also consider the pseudoscalar decay constant F_π, where the name and label are borrowed from QCD. For a composite model of EWSB, the 0^{++} becomes the Higgs boson with mass $m_h \approx 126$ GeV in the low energy effective theory of the Standard Model. The chiral value of F_π is comparable to the EWSB scale $v = 246$ GeV.

In Figure 4.15, we show the mass of the Goldstone boson, vector meson, and the 0^{++} as well as the pseudoscalar decay constant for $m_h = 0.060$ and 0.080. We begin by discussing the $m_h = 0.060$ system. First, we remark that the most chiral point suffers from a

low number of independent measurements. We are still working to improve the isosinglet measurement on this ensemble.

For all other light fermion masses, the 0^{++} mass is statistically consistent with the Goldstone boson. It is also well separated from the mass of the vector meson. This is remarkable for two reasons. First, this relatively light behavior is in contrast to QCD where the $\sigma(500)$ is roughly three times heavier than the pion and comparable in mass to the vector meson. It also gives positive evidence that not all chirally broken systems feature qualitatively similar infrared dynamics: a light scalar can exist in a chirally broken theory. This result on its own is important for composite EWSB phenomenology.

In addition, the behavior of the 0^{++} following the Goldstone boson mass qualitatively matches the mass deformed 12 fermion theory where the would-be Goldstone again tracks the 0^{++} [96]. On the scale of the 4+8 project, this suggests that for the range of light fermion masses studied, $m_h = 0.060$ is sufficiently small to generate 12 fermion scalar dynamics in the chirally broken 4+8 model. It would be interesting to see if this is a general behavior of $N_\ell + N_h$ models. More specifically, is it possible to put the scalar dynamics of any mass-degenerate $N_\ell + N_h$ fermion theory into the chirally broken N_ℓ fermion theory by this mechanism?

The picture is qualitatively different for $m_h = 0.080$. The 0^{++} mass is marginally larger than the mass of the Goldstone as opposed to being degenerate. Similar to the $m_h = 0.060$ case, the scalar is well separated from the vector meson. From a numerical standpoint, the $m_h = 0.080$ ensembles are our highest quality, offering a balance between producing sufficiently light states, which eases performing nonlinear fits, and low autocorrelation, which reduces the relative cost of producing independent measurements.

We do not show a plot of the 0^{++} mass for the $m_h = 0.100$ ensembles because we cannot reliably extract a numerical value. In contrast to the $m_h = 0.060$ ensembles where difficulties arise from low statistics due to high autocorrelations, on the $m_h = 0.100$ ensembles the mass of the 0^{++} is too heavy to extract despite high statistics. This problem arises because the 0^{++} mass is extracted from a signal which decays exponentially in the mass against a

constant background of noise.

The behaviors going from $m_h = 0.060$ to 0.100 suggest that the 0^{++} is getting heavier as m_h increases. If true, this is an important result: the 4+8 model not only prescribes a method to continuously tune walking behavior, but also shows a correlation between near conformal behavior and a light 0^{++} state.

In the greater picture of composite models for EWSB, we consider the ratio of the mass of the 0^{++} to the pseudoscalar decay constant, F_π. This quantity is phenomenologically related to the measured SM ratio $\frac{M_{Higgs}}{v} \approx 0.5$. As a naïve estimation, the linear extrapolation of $M_{0^{++}}$ and F_π for $m_h = 0.080$ in Figure 4.15 suggests a ratio more comparable to 3. This is not a concern for the 4+8 model and the general $N_\ell + N_h$ for two reasons. First, our lattice simulations of the 4+8 model do not include the dynamical effects of the top quark. In an effective field theory treatment, the top loop contribution reduces the mass of the 0^{++}. A ratio of 3 before considering SM effects may therefore be sufficient [97]. Furthermore, even if dynamical contributions from the SM are not sufficient to make the 4+8 model phenomenologically viable, a different $N_\ell + N_h$ model could provide the correct behavior.

The 4+8 model joins the $SU(3)$ 8 fermion theory as an important composite model for EWSB. The 8 fermion theory is likely chirally broken, and if so is near conformal and contains a relatively light scalar. These two models suggest that a light scalar could be a general consequence of walking dynamics as opposed to being a dynamical coincidence of one model. The 4+8 model, and the general $N_\ell + N_h$ model, is a unique platform to quantitatively study the effect of near conformal dynamics on composite theories through a single continuously tunable parameter.

4.7 Future Work

There are multiple avenues for future studies of the 4+8 model. There is evidence that the mass of the light 0^{++} state depends on the heavy fermion mass. In light of this, we are pursuing improved methods to extract the mass of the 0^{++}. One method is improved quark sources as mentioned in section 3.2. Improved sources can greatly suppress the coupling of

excited states to two-point correlation functions. This makes it possible to extract the 0^{++} mass from earlier, less noisy time separations.

In our current studies, we assume that the heavy fermions contribute negligibly to determining the 0^{++} mass. We can test this assumption by including heavy fermion interpolating operators in our study. The basic motivation and methods of a light/heavy fermion mixing study are summarized in appendix B.3. Heavy fermion operators can be used in conjunction with improved sources, producing an additional improvement on extracting the 0^{++} mass.

For the purpose of this study, we have focused on only three states: the Goldstone boson, the vector meson, and the 0^{++}. The 4+8 model contains a far larger spectrum than just these three states. This spectrum becomes important if we want to transform the 4+8 model into a model of EWSB satisfying electroweak constraints. As an example, the axial vector meson, or the a_1 in QCD language, is an important piece of a lattice study of the S parameter [98]. Further, as part of a larger model for BSM physics, the lightest baryon of the 4+8 model could become a stable composite dark matter candidate [99].

The heavy fermions also contribute measurable states in the spectrum of the 4+8 model. Of particular concern is the Goldstone boson containing a single light and a single heavy fermion. This state could be lighter than the purely light fermion vector meson. It is important that this state is still heavy enough to also escape detection.

As an avenue to study the underlying low energy structure of the 4+8 model, we can construct a low energy effective theory including both Goldstone bosons and a light scalar. This effective theory includes the decay constants for the Goldstone bosons and the scalar state, as well as the trilinear coupling of two Goldstone bosons to the isosinglet 0^{++} meson. We could also compare the trilinear coupling with experimentally measured couplings of the $W^{\pm}$ and Z bosons to the Higgs boson. An example of how to pursue some of these measurements can be found in [100].

In the pursuit of controlling lattice artifacts, one avenue of future work is taking the continuum limit as outlined in section 1.6.

As a last direction of future work, a viable composite model of EWSB must have only

two chiral fermions to produce three massive vector bosons. In the context of a larger composite model for EWSB, we could pursue a study of a $2 + N_h$ model, where N_h could be tuned to provide a more phenomenologically viable walking sector than the $N = 12$ conformal case.

Even with all of these future options, the 4+8 model has already proven itself to be a powerful model to study near-conformal phenomenology. Given sufficient computing resources, it is possible to generate an arbitrarily long walking regime in the running coupling by tuning m_h and ask questions about the low energy consequences of this tuning. In particular, we have already demonstrated hints of dependence of the light fermion isosinglet 0^{++} state on the heavy fermion mass. Going forward, it will be interesting to consider the potential future directions of research and ask further questions about the effect of walking dynamics on composite theories.

Appendices

A Compositeness and the 4+8 Model

A.1 Derivation of Staggered Fermions

Our derivation of staggered fermions begins in one dimension with a single coordinate x factored into two components: a piece n indexing the "hypercube," which is simply a pair of lattice sites in one dimension, and a piece α indexing sites of the hypercube, such that

$$x = 2n + \alpha. \tag{A.1}$$

We can make a lattice fermion more compact by writing a single fermion as a two-component object at a site n

$$\chi(n) \equiv \begin{pmatrix} \chi_e(n) \\ \chi_o(n+1) \end{pmatrix}. \tag{A.2}$$

Using the naïve free field lattice action as motivation, we can motivate the staggered action via two operations. The free field lattice action is given by

$$S = a \sum_x \frac{1}{2a} \left(\bar{\psi}_x \gamma_x \psi_{x+1} - \bar{\psi}_{x+1} \gamma_x \psi_x \right) + a \sum_x m \bar{\psi}_x \psi_x. \tag{A.3}$$

1. The first operation is translation by a single lattice site. In terms of our two-component notation, this translation interchanges even and odd sites, and as such we can represent this operation by the Pauli matrix

$$\sigma_1 = \begin{pmatrix} 0 & 1 \\ 1 & 0 \end{pmatrix}. \tag{A.4}$$

2. The doubling problem itself motivates a phase factor $(-1)^x$. In one dimension, the discrete massless free fermion has two zero modes: one at $p = 0$, and one at $p = \pi/a$. We can project these out by a Fourier transform. The zero momentum piece is given by $(1)^0 x_1 + (1)^1 x_2$, while the doubler mode, corresponding to π/a momentum, is $(-1)^0 x_1 + (-1)^1 x_2$. This phase factor can be represented by the Pauli matrix

$$\sigma_3 = \begin{pmatrix} 1 & 0 \\ 0 & -1 \end{pmatrix}. \tag{A.5}$$

This construction readily generalizes to four dimensions. Our definition of a coordinate becomes

$$x_\mu \equiv 2n_\mu + \alpha_\mu. \tag{A.6}$$

Instead of having one set of operators, we have four sets for each space-time dimension. Each set of operators is respectively denoted by

$$\begin{aligned} x &\to \sigma_1, \sigma_3, \\ y &\to \rho_1, \rho_3, \\ z &\to \pi_1, \pi_3, \\ t &\to \tau_1, \tau_3, \end{aligned} \tag{A.7}$$

where σ_1, ..., τ_1 describe translations in the x, ..., t directions, and σ_3, ..., τ_3 switch zero modes, respectively. Since translations and Fourier transforms in orthogonal directions commute, the different pairs of Pauli matrices commute with one another.

It is still constructive to consider an overall even-odd phase function denoted by the total phase

$$\begin{aligned}\epsilon(x_\mu) &= (-1)^{x_x+x_y+x_z+x_t} \\ &\equiv (-1)^{\alpha_x+\alpha_y+\alpha_z+\alpha_t}.\end{aligned} \tag{A.8}$$

Using the above sets of translation and phase operators, we can construct a fermion "gamma matrix" algebra. In four Euclidean dimensions, the Dirac matrix algebra obeys

$$\{\gamma_\mu, \gamma_\nu\} = 2\delta_{\mu\nu}. \tag{A.9}$$

Let us begin with the x component, comparing with the naïve action. In the x direction, there is a translation and there is a γ_x. Here we make the simple identification

$$\gamma_x \to \sigma_1. \tag{A.10}$$

The properties of the Pauli matrices ensure σ_1 satisfies the Dirac algebra.

Next, let us look at the y direction. As before, there is a translation and a factor of γ_y. It is not sufficient to identify γ_y with the translation operator in the y direction, ρ_1, as that does not produce the correct anticommutator with our γ_x. At the cost of a phase factor, we can achieve the correct anticommutator by identifying γ_y with $\sigma_1\rho_3$ instead.

We can continue this practice to develop a full set of γ matrices defined by

$$\begin{aligned}\gamma_x &\to \sigma_1, \\ \gamma_y &\to \sigma_3\rho_1, \\ \gamma_z &\to \sigma_3\rho_3\pi_1, \\ \gamma_t &\to \sigma_3\rho_3\pi_3\tau_1.\end{aligned} \tag{A.11}$$

We also note

$$\gamma_5 = \gamma_x\gamma_y\gamma_z\gamma_t = \sigma_1\sigma_3\rho_1\pi_1\pi_3\tau_1. \tag{A.12}$$

While this successfully reconstructs the Dirac algebra for spin, it does not span the full potential algebra of the Pauli matrices. This is motivated by a counting exercise: we have chosen to distribute one fermion degree of freedom over a 2^4 hypercube on the lattice. Thus, we have spread a single-site fermion, a $4N_c$-component object, over sixteen sites each with a single N_c component object. Since we have utilized four times the number of degrees of freedom we originally had needed to, it should not be a surprise that a single staggered fermion contains four Dirac flavors. To transform between these four flavors, we can generate an additional $SU(4)$ of so-called "taste symmetry" which commutes with the spin symmetry we previously constructed. The algebra of the taste symmetry satisfies the same structure as the Dirac algebra. The analogs of the γ matrices of the spin algebra are denoted by Γ.

Let us begin building by Γ_x. First, let us demand the matrix commutes with γ_x. Trivially, this can be accomplished with $\Gamma_x = \sigma_1$. This matrix as is does not commute with the other three γ matrices. To impose this, we can add additional matrices to the definition that commute with γ_x but anti-commute with γ_y, γ_z, and γ_t. This is satisfied by $\Gamma_x = \sigma_1\rho_3\pi_3\tau_3$.

Following this train of thought, we can construct the other Γ matrices by

$$\begin{aligned}
\Gamma_x &\to \sigma_1\rho_3\pi_3\tau_3, \\
\Gamma_y &\to \rho_1\pi_3\tau_3, \\
\Gamma_z &\to \pi_1\tau_3, \\
\Gamma_t &\to \tau_1,
\end{aligned} \tag{A.13}$$

where

$$\Gamma_5 = \Gamma_x\Gamma_y\Gamma_z\Gamma_t = \sigma_1\rho_1\rho_3\pi_1\tau_1\tau_3. \tag{A.14}$$

Lastly, we note

$$\begin{aligned}\gamma_5\Gamma_5 &= \sigma_3\rho_3\pi_3\tau_3 \\ &\equiv \epsilon(x_\mu).\end{aligned} \tag{A.15}$$

One can verify that these definitions satisfy $\{\Gamma_\mu, \Gamma_\nu\} = 2\eta_{\mu\nu}$ and $[\Gamma_\mu, \gamma_\nu] = 0$, and as such we have generated two non-overlapping $SU(4)$ algebras of spin and taste.

From a theoretical standpoint, the only remaining discussion of the staggered action is recognizing the remaining lattice chiral symmetry. In the naïve case, the lattice chiral symmetry manifests itself as the γ_5 hermiticity of the naïve Dirac matrix. To find the equivalent hermiticity condition for the staggered Dirac matrix, we investigate the interacting staggered Dirac matrix, $D_{staggered}$, defined from the action in Eqn. 1.21 by

$$D^{staggered}_{x,y} = \left(\sum_\mu \frac{1}{2}\eta_\mu(x)\left[\delta_{x,y-\hat{\mu}}U_\mu(x) - \delta_{x,y+\hat{\mu}}U^\dagger_\mu(x-\hat{\mu})\right]\right) + m\delta_{x,y}. \tag{A.16}$$

We motivate the form of the staggered chiral symmetry by blindly computing the Hermitian conjugate of the staggered Dirac matrix,

$$\begin{aligned}D^{staggered,\dagger}_{x,y} &= \left(\sum_\mu \frac{1}{2}\eta_\mu(y)\left[\delta_{y,x-\hat{\mu}}U^\dagger_\mu(y) - \delta_{y,x+\hat{\mu}}U_\mu(y-\hat{\mu})\right]\right) + m\delta_{x,y} \\ &= \left(\sum_\mu \frac{1}{2}\left[\eta_\mu(x-\hat{\mu})\delta_{y+\hat{\mu},x}U^\dagger_\mu(x-\hat{\mu}) - \eta_\mu(x+\hat{\mu})\delta_{y-\hat{\mu},x}U_\mu(x)\right]\right) + m\delta_{x,y} \\ &= \left(\sum_\mu \frac{1}{2}\eta_\mu(x)\left[\delta_{y+\hat{\mu},x}U^\dagger_\mu(x-\hat{\mu}) - \delta_{y-\hat{\mu},x}U_\mu(x)\right]\right) + m\delta_{x,y} \\ &= -\left(\sum_\mu \frac{1}{2}\eta_\mu(x)\left[\delta_{x,y-\hat{\mu}}U_\mu(x) - \delta_{x,y+\hat{\mu}}U^\dagger_\mu(x-\hat{\mu})\right]\right) + m\delta_{x,y},\end{aligned} \tag{A.17}$$

where we have taken advantage of the property

$$\eta_\mu(x \pm \hat{\mu}) = 1 = \eta_\mu(x). \tag{A.18}$$

The mass term is automatically Hermitian. On the other hand, the "hopping term" which connects neighboring lattice sites is anti-Hermitian. To make the hopping term Hermitian, we can apply a total phase $\epsilon(x)$. The total phase contributes an additional factor of -1 to the hopping term since it connects even and odd lattice sites. This is better defined in terms of an even/odd decomposition of the staggered Dirac matrix

$$D_{xy}^{staggered} = \begin{pmatrix} D_{xy,ee}^{stag} & D_{xy,eo}^{stag} \\ D_{xy,oe}^{stag} & D_{xy,oo}^{stag} \end{pmatrix}, \tag{A.19}$$

where we have defined

$$D_{xy,ee}^{staggered} = D_{xy,oo}^{staggered} = m\delta_{x,y}, \tag{A.20}$$

$$D_{xy,eo}^{staggered} = D_{xy,oe}^{staggered} = \left(\sum_\mu \frac{1}{2} \eta_\mu(x) \left[\delta_{x,y-\hat{\mu}} U_\mu(x) - \delta_{x,y+\hat{\mu}} U_\mu^\dagger(x-\hat{\mu}) \right] \right). \tag{A.21}$$

We check explicitly that the total phase factor gives the required hermiticity condition:

$$\begin{aligned} \epsilon(x) D_{xy}^{stag} \epsilon(y) &= \begin{pmatrix} 1 & 0 \\ 0 & -1 \end{pmatrix} \begin{pmatrix} D_{xy,ee}^{stag} & D_{xy,eo}^{stag} \\ D_{xy,oe}^{stag} & D_{xy,oo}^{stag} \end{pmatrix} \begin{pmatrix} 1 & 0 \\ 0 & -1 \end{pmatrix} \\ &= \begin{pmatrix} D_{xy,ee}^{stag} & D_{xy,eo}^{stag} \\ -D_{xy,oe}^{stag} & -D_{xy,oo}^{stag} \end{pmatrix} \begin{pmatrix} 1 & 0 \\ 0 & -1 \end{pmatrix} \\ &= \begin{pmatrix} D_{xy,ee}^{stag} & -D_{xy,eo}^{stag} \\ -D_{xy,oe}^{stag} & D_{xy,oo}^{stag} \end{pmatrix} \\ &= \begin{pmatrix} D_{yx,ee}^{stag\dagger} & D_{yx,oe}^{stag\dagger} \\ D_{yx,eo}^{stag\dagger} & D_{yx,oo}^{stag\dagger} \end{pmatrix} \\ &= D_{yx}^{stag\dagger}. \end{aligned} \tag{A.22}$$

The γ_5 hermiticity of the continuum action manifests itself as a phase hermiticity of the staggered Dirac matrix.

B Spectrum Measurements

B.1 Coulomb Gauge Fixing

As motivated in section 3.3, quark sources distributed over an entire timeslice can be useful for extracting the ground states for some fermionic correlation functions, despite being unphysically non-local. Unfortunately, when writing down a non-local quark source, care needs to be taken to make sure the source is gauge covariant. It can be prohibitively expensive to perform this explicitly. An alternative to doing this to the quark source itself is to perform Coulomb gauge fixing on the gauge links themselves, shifting the problem of gauge covariance to the gauge fields from the quark fields. After a quick introduction to gauge fixing in the continuum, we discuss gauge fixing on the lattice. As part of the work I performed for the 4+8 model, I adapted existing code for gauge fixing into `FUEL`.

B.1.1 Continuum Gauge Fixing

Let us constrain our discussion to Coulomb gauge ($\vec{\nabla} \cdot \vec{A} = 0$). Results, in general, extend well to Landau gauge ($\partial_\mu A_\mu = 0$), and in fact rather trivially because we're constraining our discussion to Euclidean metrics as well.

First, lets discuss $U(1)$ gauge fixing, for example in E&M. We know that the vector potential, A_μ, is not the physical quantity in the theory. On the other hand, the field strength tensor $F_{\mu\nu}$ is. The field strength tensor under $U(1)$ is defined by

$$F_{\mu\nu} = \partial_\mu A_\nu - \partial_\nu A_\mu. \tag{B.1}$$

In the $U(1)$ gauge theory, the field strength tensor $F_{\mu\nu}$ is a true physical property of the theory. Since A_μ is not physical, we have the freedom to redefine it so long as we leave $F_{\mu\nu}$ invariant. Since the field strength tensor is antisymmetric, we note that the transformation

$$A_\mu \to A_\mu + \partial_\mu \chi, \tag{B.2}$$

where χ is an arbitrary scalar function of x^μ, leaves $F_{\mu\nu}$ invariant.

This is a manifestation of gauge invariance. To fix the gauge, we need to impose some type of additional constraint on the gauge field. One choice is Coulomb gauge, defined by

$$\vec{\nabla} \cdot \vec{A} = 0. \tag{B.3}$$

Given any vector potential A_μ, we can construct a χ such that $\tilde{A_\mu} \equiv A_\mu + \partial_\mu \chi$ satisfies Coulomb gauge condition given by

$$\begin{aligned} 0 &= \vec{\nabla} \cdot \vec{\tilde{A}} \\ &= \vec{\nabla} \cdot \vec{A} + \nabla^2 \chi.. \end{aligned} \tag{B.4}$$

We thus see the requirement that χ satisfies

$$\nabla^2 \chi = -\vec{\nabla} \cdot \vec{A}. \tag{B.5}$$

By the use of Green's functions for the Poisson equation, we can immediately write down the result to this partial differential equation under the assumption that the fields decay to zero infinite far away. The solution is given as

$$\chi(x^\mu) = \frac{1}{4\pi} \int d^3x' \frac{\vec{\nabla}' \cdot \vec{A}(x'^\mu)}{|\vec{x} - \vec{x'}|}. \tag{B.6}$$

Shifting A_μ by the divergence of the above scalar field will give us, by construction, a field with the same physics and satisfying Coulomb gauge.

B.1.2 Gauge Fixing in $SU(N)$

On the lattice, and in the case of non-Abelian gauge theories, we take a different approach to gauge fixing which we can nonetheless show reduces appropriately in the continuum limit. We consider optimizing the following function

$$f(g,U) = \sum_{x,i=1,2,3} \mathrm{Tr}\left[g(x)U_\mu(x)g^\dagger(x+\hat{i})\right], \tag{B.7}$$

with respect to the $SU(N)$ group matrices g, where $U_\mu(x)$ are the gauge fields in the $SU(N)$ group.

To avoid managing structured matrices in optimizing this function, we will impose the fact that g is in the $SU(N)$ group via Lagrange multipliers satisfying the following constraint equations:

$$\begin{aligned} g(x)g^\dagger(x) &= \mathbf{I}, \\ \det(g(x)) &= 1, \\ \det(g^\dagger(x)) &= 1. \end{aligned} \tag{B.8}$$

In doing this, we leave $g(x)$ and $g^\dagger(x)$ as independent, unstructured matrices, and enforce the $SU(N)$ gauge group structure via these constraints. Since we do not differentiate with respect to the gauge links $U_\mu(x)$ at any point, we can consider them members of the $SU(N)$ gauge group *a priori*.

The final function to optimize, conveniently written in component notation, with Lagrange multipliers can be written as

$$\begin{aligned} f(g,U) = &\sum_{x,i=1,2,3} \left[g_{\alpha\beta}(x)U_{i,\beta\gamma}(x)g^\dagger_{\gamma\alpha}(x+\hat{i})\right] \\ &+ \lambda_{1,\gamma\alpha}(x)\left(g_{\alpha\beta}(x)g^\dagger_{\beta\gamma}(x) - \mathbf{I}_{\alpha\gamma}\right) + \lambda_2(x)\left(\det(g(x)) - 1\right) + \lambda_3(x)\left(\det(g^\dagger(x))\right). \end{aligned} \tag{B.9}$$

We will vary this with respect to $g_{\delta\epsilon}(y)$.

We note that if we have periodic boundary conditions or are in infinite volume, we are free to shift the first part of Eqn. B.9, since the sum over all x implies translational invariance. We will use a shifted form given as

$$g_{\alpha\beta}(x-\hat{i})U_{i,\beta\gamma}(x-\hat{i})g^{\dagger}_{\gamma\alpha}(x) \tag{B.10}$$

with liberty when we vary with respect to $g^{\dagger}$.

As a last note before pressing through, we note the known result for the derivative of the determinant of a matrix with respect to the components of the matrix, given as

$$\frac{\partial \det(g)}{\partial m} = \det(g)\mathrm{Tr}\left[g^{-1}\frac{\partial g}{\partial m}\right]. \tag{B.11}$$

First, we perform the variation of Eqn. B.9 with respect to $g_{\delta\epsilon}$.

$$\begin{aligned}\frac{\partial f}{\partial g_{\delta\epsilon}(y)} &= \sum_{i=1,2,3}\left[\delta_{\alpha\delta}\delta_{\beta\epsilon}\delta_{x,y}U_{i,\beta\gamma}(x)g^{\dagger}_{\gamma\alpha}(x+\hat{i})\right] \\ &\quad + \lambda_{1,\gamma\alpha}(x)\left(\delta_{\delta\alpha}\delta_{\epsilon\beta}\delta_{x,y}g_{\alpha\beta}(x)g^{\dagger}_{\beta\gamma}(x)\right) + \lambda_2(x)\det(g(x))g^{-1}_{\alpha\beta}(x)\delta_{\delta\beta}\delta_{\epsilon\alpha}\delta_{x,y} \\ &= \sum_i\left[U_{i,\epsilon\gamma}(y)g^{\dagger}_{\gamma\delta}(y+\hat{i})\right] + g^{\dagger}_{\epsilon\gamma}(y)\lambda_{1,\gamma\delta}(y) + \lambda_2(y)g^{\dagger}_{\epsilon\delta}(y).\end{aligned} \tag{B.12}$$

Using the alternative form for the first term of Eqn. B.9 given in Eqn. B.10, we immediately jump to the result for variation with respect to $g^{\dagger}_{\delta\epsilon}$, given by

$$\frac{\partial f}{\partial g^{\dagger}_{\delta\epsilon}(y)} = \sum_i\left[g^{\dagger}_{\epsilon\beta}(y-\hat{i})U_{i,\beta\delta}(y-\hat{i})\right] + \lambda_{1,\epsilon\alpha}(y)g_{\alpha\delta}(y) + \lambda_3(y)g_{\epsilon\delta}(y). \tag{B.13}$$

We have made liberal use of the fact that the Lagrange multipliers constrain the g's to be members of $SU(N)$ group.

At this point, the explicit component notation ceases to be useful, and we write

$$\frac{\partial f}{\partial g} = \sum_i \left[U_i(y)g^\dagger(y+\hat{i})\right] + g^\dagger(y)\bar{\lambda}_1(y) + \lambda_2(y)g^\dagger(y) = 0, \tag{B.14}$$

$$\frac{\partial f}{\partial g^\dagger} = \sum_i \left[g(y-\hat{i})U_i(y-\hat{i})\right] + \bar{\lambda}_1(y)g(y) + \lambda_3(y)g(y) = 0. \tag{B.15}$$

We use an overbar on λ_1 to denote that it is a matrix, not a scalar.

We need to eliminate the Lagrange multipliers from these two expressions. This is a multi-step process. First, let us multiply the variation with respect to g from the **left** by $g(y)$, and the variation with respect to $g^\dagger$ from the **right** by $g^\dagger(y)$, giving us

$$g(y)\frac{\partial f}{\partial g} = \sum_i \left[g(y)U_i(y)g^\dagger(y+\hat{i})\right] + \bar{\lambda}_1(y) + \lambda_2(y)\mathbf{I} = 0, \tag{B.16}$$

$$\frac{\partial f}{\partial g^\dagger}g^\dagger(y) = \sum_i \left[g(y-\hat{i})U_i(y-\hat{i})g^\dagger(y)\right] + \bar{\lambda}_1(y) + \lambda_3(y)\mathbf{I} = 0. \tag{B.17}$$

We take a second to solve explicitly for λ_2 and λ_3 in terms of the other variables. This occurs by solving for $\lambda_{2,3}\mathbf{I}$ in their respective equations, then taking a determinant, providing the results

$$\lambda_2(y) = \det\left(-\sum_i \left[g(y)U_i(y)g^\dagger(y+\hat{i})\right] - \bar{\lambda}_1(y)\right), \tag{B.18}$$

$$\lambda_3(y) = \det\left(-\sum_i \left[g(y-\hat{i})U_i(y-\hat{i})g^\dagger(y)\right] - \bar{\lambda}_1(y)\right). \tag{B.19}$$

Let us next take the difference of the two variations in Eqn. B.16 and B.17 to cancel the $\bar{\lambda}_1$ dependence.

$$g(y)\frac{\partial f}{\partial g} - \frac{\partial f}{\partial g^\dagger}g^\dagger(y) \tag{B.20}$$

$$= \sum_i \left[g(y)U_i(y)g^\dagger(y+\hat{i}) - g(y-\hat{i})U_i(y-\hat{i})g^\dagger(y)\right] + \left[\lambda_2(y) - \lambda_3(y)\right]\mathbf{I} = 0 \tag{B.21}$$

Finally, we take a leap of faith and show it's self consistent: let us assume $\lambda_2(y) = \lambda_3(y)$. Doing so, we find

$$g(y)\frac{\partial f}{\partial g} - \frac{\partial f}{\partial g^\dagger}g^\dagger(y) = \sum_i \left[g(y)U_i(y)g^\dagger(y+\hat{i}) - g(y-\hat{i})U_i(y-\hat{i})g^\dagger(y)\right] = 0$$
$$\rightarrow \sum_i \left[g(y)U_i(y)g^\dagger(y+\hat{i})\right] = \sum_i \left[g(y-\hat{i})U_i(y-\hat{i})g^\dagger(y)\right]. \quad \text{(B.22)}$$

With this observation, we note that we self-consistently get $\lambda_2(y) = \lambda_3(y)$ from our above definitions. Thus, our assumption is sound.

As our final conclusion, we find that a set of $g(y)$ satisfying the constraint

$$\sum_i \left[g(y)U_i(y)g^\dagger(y+\hat{i}) - g(y-\hat{i})U_i(y-\hat{i})g^\dagger(y)\right] = 0 \quad \text{(B.23)}$$

will optimize the expression given in Eqn. B.9.

Lastly, lets expand this to lowest order to see that we're reproducing the requirement of Coulomb gauge.

$$\begin{aligned} 0 &= \sum_i \left[g(y)U_i(y)g^\dagger(y+\hat{i}) - g(y-\hat{i})U_i(y-\hat{i})g^\dagger(y)\right] \\ &\approx \sum_i \left(\chi(y) + aA_i(y) - \chi(y+\hat{i}) - \chi(y-\hat{i}) - aA_i(y-\hat{i}) + \chi(y)\right) \\ &\approx \sum_i -a^2\partial_i^2\chi + a^2\partial_i A_i \\ &\rightarrow \vec{\nabla}\cdot\vec{A} - \nabla^2\chi = 0, \end{aligned} \quad \text{(B.24)}$$

which is the result we found in the previous section.

The matrices $g(y)$ which satisfy Eqn. B.23 can be found by an iterative procedure in the spirit of gauge relaxation. This algorithm is used in the implementation of gauge fixing contributed to `FUEL`.

B.2 Measurements Performed in FUEL

A list of all states whose measurements are currently implemented in FUEL [62]. The current standard set of spectrum measurements is anything with a 'Code'. Unless otherwise specified, every measurement uses a point sink.

State	Description	Parity Partner	P.P. Description	Method	Code	Note
Pion (G.B.)	$\gamma_5 \otimes \gamma_5$	–	–	Wall [86]	`ps`	
Pion (G.B.)	$\gamma_5 \otimes \gamma_5$	–	–	Random wall	`ps2`	1
Pion	$\gamma_4\gamma_5 \otimes \gamma_4\gamma_5$	Scalar (T.S.)	$1 \otimes 1$	Wall	`sc`	2
Pion	$\gamma_5 \otimes \gamma_5\gamma_3$	–	–	Wall	`i5`	
Pion	$\gamma_4\gamma_5 \otimes \gamma_1\gamma_2$	Scalar	$1 \otimes \gamma_3$	Wall	`ij`	
Rho	$\gamma_3 \otimes \gamma_2\gamma_3$	Tensor	$\gamma_1\gamma_2 \otimes \gamma_1$	Wall	`rij`	
Rho	$\gamma_3\gamma_4 \otimes \gamma_1\gamma_5$	Axial	$\gamma_3\gamma_5 \otimes \gamma_1\gamma_4$	Wall	`ri5`	
Rho	$\gamma_1\gamma_4 \otimes \gamma_4$	Axial	$\gamma_1\gamma_5 \otimes \gamma_5$	Wall	`r0`	
Rho (T.S.)	$\gamma_1 \otimes 1$	Tensor	$\gamma_2\gamma_3 \otimes \gamma_4\gamma_5$	Wall	`ris`	
Nucleon	8^+ Baryon	Lambda	8^- Baryon	Wall	`nu`	2
Delta	$8'^+$ Baryon	Excited Nucleon	$8'^-$ Baryon	Wall source	`de`	2
Scalar (T.S.)	$1 \otimes 1$	Pion	$\gamma_4\gamma_5 \otimes \gamma_4\gamma_5$	Stochastic [91]	`sc_stoch`	4
Scalar (T.I.S.)	$1 \otimes 1$	Pion	$\gamma_4\gamma_5 \otimes \gamma_4\gamma_5$	Stochastic	`dc_stoch_zcen` `sg_stoch_zcen`	4

Table B.1. A list of states I have implemented measurements for in FUEL. A list of all states I have implemented measurements for in FUEL. For conciseness, I have used the following abbreviations: (G.B.) = Goldstone boson, (T.S.) = Taste singlet, (T.I.S.) = Taste- and Iso- singlet.

Note that, in the case of point or wall sources, the $\varepsilon(x_\mu)$ hermiticity requires the insertion of the phase plus shift with an additional $(-1)^{x+y+z+t}$. For example, in the case of the Goldstone Boston pion, this implies that the propagator dot product has no additional phase shifts, which is to be expected of the Goldstone boson state.

1. Used for measuring F_π.

2. This scalar is the isomultiplet, not the isosinglet.

3. The state listed is the lowest mass state in the rep based off QCD ordering. See [101] for more info.

4. Comes from stochastic, diluted measurements.

B.3 Isosinglet Scalar, Light-Heavy Mixing: Theory

As noted in section 3.6, in a fully rigorous study of the scalar spectrum of the 4+8 model, we cannot ignore the potential for the light isosinglet scalar to contain contributions from both the light and the heavy flavors. We can formulate this on the lattice as an operator mixing problem, and we'll see that this is equivalent to thinking about $\eta - \eta'$ mixing in QCD. Indeed, due to familiarity, we will begin there.

B.3.1 QCD Warmup: $\eta - \eta'$ Mixing

We can address $\eta - \eta'$ mixing from two standpoints:

- Thinking from the perspective of the 8-fold way, that is, assuming the up, down, and strange quarks are degenerate. This gives an $SU(3)_S$ isospin symmetry.
- Thinking from the perspective where the up and down quarks are degenerate (and called the "light" quarks), with a split strange quark, assuming there's no mixing. This gives us an $SU(2)_I$ isospin symmetry of the light quarks.

In nature, we are somewhere in between: for all intents and purposes the up and down quarks are degenerate, and the strange is split, but not so much that mixing is negligible.

This makes the light quarks plus the strange quark an ideal place to think about mixing in the 4+8 project, with the following analogies:

- 8-fold way $\leftrightarrow$ case where $m_\ell = m_h$ in the 4+8 model.
- Two light quarks plus strange quark with no mixing $\leftrightarrow$ case where $m_h \to \infty$ so there is no mixing.

Let us break down the QCD case from both standpoints. By understanding both standpoints, we can quickly understand how mixing will happen in the 4+8 model.

8-fold way

In the case where the up, down, and strange quarks are all mass degenerate, we have an $SU(3)_S$ isospin symmetry[1]. We can predict the pseudoscalar[2] meson spectrum by simple group theory:

$$\mathbf{3} \otimes \bar{\mathbf{3}} = \mathbf{8} \oplus \mathbf{1},$$

Where

- The **8** has $S = 1$ (octet, or adjoint of $SU(3)_S$). These are the 3 pions, 4 kaons, and the η, which can be thought of as coming from the 8 Gell-Mann matrices.
- The **1** has $S = 0$ (singlet of $SU(3)_S$). This is the η'.

Of course, nature does not exactly work this way: the strange quark is split from the up and down. Let's see what the other extreme predicts.

2+1 QCD

In the case where the up and down are mass degenerate, while the strange quark is split such that there is no mixing, we have an $SU(2)_I$ isospin symmetry between the up and down (light) quarks. The meson spectrum still follows from group theory, and should remind us a bit more of nature in some respects:

$$(\mathbf{2} \oplus \mathbf{1}) \otimes (\bar{\mathbf{2}} \oplus \bar{\mathbf{1}}) = (\mathbf{2} \otimes \bar{\mathbf{2}}) \oplus (\mathbf{2} \otimes \bar{\mathbf{1}}) \oplus (\mathbf{1} \otimes \bar{\mathbf{2}}) \oplus (\mathbf{1} \otimes \bar{\mathbf{1}}),$$

where each term on the right hand side corresponds to:

[1] Technically, if we ignore the chiral anomaly, we have a $U(3) = SU(3)_S \otimes U(1)$, where the $U(1)$ is a type of hypercharge. We'll see later that, anomaly or not, we don't need to care about any $U(1)$ symmetry for the η and η', and the analogs for the 4+8 model.

[2] and, in general, any spin/parity state, because flavor commutes with spin/parity

- The $(\mathbf{2} \otimes \bar{\mathbf{2}})$ breaks into a $\mathbf{3} \oplus \mathbf{1}$ of the $SU(2)_I$, giving:
  - The $\mathbf{3}$ has $I = 1$ (a triplet or adjoint of $SU(2)_I$), which is the 3 pions.
  - The $\mathbf{1}$ has $I = 0$ (a singlet of $SU(2)_I$), which we'll call an η_ℓ and discuss later!
- The $(\mathbf{2} \otimes \bar{\mathbf{1}}) \oplus (\mathbf{1} \otimes \bar{\mathbf{2}})$ has $I = 1/2$, which is the 4 kaons. To get techical, the $\mathbf{1}$ parts are the $\bar{u}s$ and $\bar{d}s$ kaons, and the $\bar{\mathbf{1}}$ parts are the $\bar{s}u$ and $\bar{s}d$ kaons.
- The $(\mathbf{1} \otimes \bar{\mathbf{1}})$ has $I = 0$, which we'll call the η_s and also discuss later!

By looking at the isospin charge assignments, we can make a few statements that are consistent with nature.

- Due to being in different representations of isospin, we do not expect the pions to mix with the kaons, which is confirmed in nature (due to the splitting between the light quarks and the strange quark being rather large).
- The pions and kaons do not mix with the aptly named η_ℓ and η_s, which is suggestive of how the pions and kaons do not mix with the η or η' in nature.
- There is no reason, due to isospin, to assume the η_ℓ and η_s would not mix!

The last point is important for motivating $\eta - \eta'$ mixing, which we'll discuss next.

Reconciling $\eta - \eta'$ versus $\eta_\ell - \eta_s$

To reconcile the 8-fold way picture and the 2+1 picture, let us write the η, η', η_ℓ, and η_s states as matrices. Up to a normalization, we have from the 8-fold way:

$$\eta \approx \begin{pmatrix} 1 & 0 & 0 \\ 0 & 1 & 0 \\ 0 & 0 & -2 \end{pmatrix} \qquad \eta' \approx \begin{pmatrix} 1 & 0 & 0 \\ 0 & 1 & 0 \\ 0 & 0 & 1 \end{pmatrix}$$

We note that the η corresponds to λ_8, the eighth Gell-Mann matrix—more importantly, a full-rank Gell-Mann matrix with two blocks. The η', on the other hand, corresponds to the identity matrix, and as such is manifestly the singlet of $\mathbf{3} \otimes \bar{\mathbf{3}}$.

Next, up to normalization, we have from the 2+1 picture:

$$\eta_\ell \approx \begin{pmatrix} 1 & 0 & 0 \\ 0 & 1 & 0 \\ 0 & 0 & 0 \end{pmatrix} \qquad \eta_s \approx \begin{pmatrix} 0 & 0 & 0 \\ 0 & 0 & 0 \\ 0 & 0 & 1 \end{pmatrix}$$

We note that the η_ℓ is manifestly a singlet of the upper-left 2-by-2 sub-block, and the η_s is manifestly (and trivially) a singlet of the lower-right 1-by-1 sub-block.

More importantly, we see that *η and η' are a linear combination of η_ℓ and η_h*.

This paints a self-consistent picture: we argued when discussing the 2+1 picture, there's no reason to assume the η_ℓ and η_h do not mix because they transform under the same $SU(2)_I$ isospin representation. Since the η and η' are linear combinations of η_ℓ and η_h, by extension we assume η and η' mix. This argument will be critical when we jump to the 4+8 picture.

As a remark—because the η and η' are diagonal matrices (equivalently, the η_ℓ and η_s), they correspond to meson states with zero net hypercharge, regardless of how hypercharge is assigned to any fermion. This is why we could ignore any hypercharge assignment earlier.

B.3.2 The 4+8 Model

The 4+8 model is a mostly clean analogy to the 2+1 QCD case except there are now two non-Abelian isospin charges, an $SU(4)_L$ and an $SU(8)_H$, as opposed to just the one isospin ($SU(2)_I$) before because there was only a single strange quark. This leads to us having to hand-pick a certain basis of generalized Gell-Mann matrices for the full $SU(12)_F$ (which we are of course free to do) to make the mixing picture clear.

We will follow the same road map as before: first, we consider a full $SU(12)_F$ isospin, and then we will consider the split 4+8 case.

The 143-fold Way

In the case where all 12 fermions are mass-degenerate, we have the aforementioned $SU(12)_F$ isospin. We can predict the meson spectrum in the same way as before, except this time we are in the scalar, not the pseudoscalar channel.

$$\mathbf{12} \otimes \bar{\mathbf{12}} = \mathbf{143} \oplus \mathbf{1},$$

Where

- The **143** has $F = 1$ (143-tet, or adjoint of $SU(12)_F$). These are 143 a_0 particles, thought of as corresponding to the 143 generalized Gell-Mann matrices which generate $SU(12)_F$. Note that we are going to use some freedom to choose the diagonal generators, which we will discuss below.
- The **1** has $F = 0$ (singlet of $SU(12)_F$). This is the σ.

We need to specify a modified prescription for constructing the 143 generalized Gell-Mann matrices for the $SU(12)_F$, which will be important to simplify considering mixing later. The prescription is as follows:

- The 132 off-diagonal generators are constructed as normal.
- 3 of the 11 diagonal generators correspond to the 3 diagonal generators of $SU(4)$ in the upper 4-by-4 block, and all zeros in the lower 8-by-8 block.
- 7 of the 11 diagonal generators correspond to the 7 diagonal generators of $SU(8)$ in the lower 8-by-8 block, and all zeros in the upper 4-by-4 block.
- The remaining diagonal generator (which we'll call λ^{12}_{143}) is of the form, up to a rescaling,

  $$\text{diag}\,(8, 8, 8, 8, -4, -4, -4, -4, -4, -4, -4, -4)$$

  or 8 times the identity in the upper 4-by-4 block, and -4 times the identity in the lower 8-by-8 block.

The last diagonal generator (by construction, the only traceless full rank generator) corresponds to the specific a_0 that participates in mixing. We will suggestively denote it $a_{0,\eta}$.

Next, let's consider the completely split 4+8 case.

Fully split 4+8

In the case where where we have 4 degenerate light quarks and 8 degenerate heavy quarks, such that there is no mixing, we have an $SU(4)_L$ for the light quarks and an $SU(8)_H$ for the heavy quarks. Again, we can run through the group theory to predict the meson spectrum:

$$(\mathbf{4} \oplus \mathbf{8}) \otimes (\bar{\mathbf{4}} \oplus \bar{\mathbf{8}}) = (\mathbf{4} \otimes \bar{\mathbf{4}}) \oplus (\mathbf{4} \otimes \bar{\mathbf{8}}) \oplus (\mathbf{8} \otimes \bar{\mathbf{4}}) \oplus (\mathbf{8} \otimes \bar{\mathbf{8}}),$$

where each term on the right hand side corresponds to:

- The $(\mathbf{4} \otimes \bar{\mathbf{4}})$ breaks into a $\mathbf{15} \oplus \mathbf{1}$ of the $SU(4)_L$, both of which are a singlet of $SU(8)_H$, giving:
  - The $\mathbf{15}$ has $L = 1$, $H = 0$ (a 15-let or adjoint of $SU(4)_L$ and a singlet of $SU(8)_H$), which is 15 light-light a_0's (analogous to the 3 pions).
  - The $\mathbf{1}$ has $L = 0$, $H = 0$ (a singlet of $SU(4)_L$ and $SU(8)_H$), which we'll call a σ_L and discuss later!
- The $(\mathbf{4} \otimes \bar{\mathbf{8}}) \oplus (\mathbf{8} \otimes \bar{\mathbf{4}})$ has $L = 1/2$ and $H = 1/2$, which is 64 light-heavy a_0's (analogous to the 4 kaons).
- The $(\mathbf{8} \otimes \bar{\mathbf{8}})$ breaks into a $\mathbf{63} \oplus \mathbf{1}$ of the $SU(8)_H$, both of which are a singlet of $SU(4)_L$, giving:
  - The $\mathbf{63}$ has $L = 0$, $H = 1$ (a 63-let or adjoint of $SU(8)_H$ and a isosinglet of $SU(4)_L$), which is 63 heavy-heavy a_0's (which has no QCD analog because the strange is not degenerate with any other quark).
  - The $\mathbf{1}$ has $L = 0$, $H = 0$ (a singlet of $SU(4)_L$ and $SU(8)_H$), which we'll call a σ_H and discuss later!

For the same reasons as in the QCD case with the η_ℓ and η_s, we have no reason to expect the σ_L and σ_H to not mix.

Reconciling $a_{0,\eta} - \sigma$ versus $\sigma_L - \sigma_H$

To reconcile the 143-fold way picture and the 4+8 picture, let us write the $a_{0,\eta}$, σ, σ_L, and σ_H states as block-diagonal matrices. Up to a normalization, we have from the 143-fold way:

$$a_{0,\eta} \approx \begin{pmatrix} 8\mathbf{I}_4 & 0 \\ 0 & -4\mathbf{I}_8 \end{pmatrix} \qquad \sigma \approx \begin{pmatrix} \mathbf{I}_4 & 0 \\ 0 & \mathbf{I}_8 \end{pmatrix}$$

We explicitly point out again that the $a_{0,\eta}$ corresponds to λ_{143}^{12}, the custom generalized Gell-Mann matrix w defined, which is the full-rank generalized Gell-Mann matrix with two blocks. The σ, on the other hand, corresponds to the identity matrix, and as such is manifestly the singlet of $\mathbf{12} \otimes \bar{\mathbf{12}}$.

Next, up to normalization, we have from the 4+8 picture:

$$\sigma_L \approx \begin{pmatrix} \mathbf{I}_4 & 0 \\ 0 & \mathbf{0}_8 \end{pmatrix} \qquad \sigma_H \approx \begin{pmatrix} \mathbf{0}_4 & 0 \\ 0 & \mathbf{I}_8 \end{pmatrix}$$

We note that the σ_L is manifestly a singlet of the upper-left 4-by-4 sub-block, and the σ_H is manifestly a singlet of the lower-right 8-by-8 sub-block.

More importantly, and again, we see that *$a_{0,\eta}$ and σ are a linear combination of σ_L and σ_H*.

This paints a similar self-consistent picture as before: in the 4+8 picture, there's no isospin reason to assume the σ_L and σ_H should not mix. Since the $a_{0,\eta}$ and σ are linear combinations of σ_L and σ_H, by extension we assume $a_{0,\eta}$ and σ mix.

B.3.3 Operator Mixing

Dirac Fermion Case

For first consideration, we will assume we have continuum Dirac fermions. The operators which we measure are $\mathcal{O}_{0^{++}}$ and $\mathcal{O}_{0^{++},h}$ as given in Eqn. 3.47 and 3.57, respectively, corresponding to the light fermion and heavy fermion isosinglet scalar operator. For simplicity,

we will assume that these operators only couple to the lowest lying states, and we do not have to worry about excited or scattering states. We will also assume that we are working with vacuum subtracted operators, and leave the details of the vacuum subtraction for later.

We need to chose what basis to write down our correlator matrix in. To match the $\eta - \eta'$ literature, we start in the basis where, if there was no mixing, we would have the σ_L and the σ_H on the diagonal. For a general $N_\ell + N_h$ theory, we would write down the following correlator matrix:

$$\begin{pmatrix} N_\ell D_{\ell\ell}(t) - C_{\ell\ell}(t) & \sqrt{N_\ell N_h} D_{\ell h}(t) \\ \sqrt{N_\ell N_h} D_{h\ell}(t) & N_h D_{hh}(t) - C_{hh}(t) \end{pmatrix} \tag{B.25}$$

Where:

- $D_{\ell\ell}(t)$ is the disconnected light-light correlator.
- $C_{\ell\ell}(t)$ is the connected light-light correlator.
- $D_{\ell h}(t)$ and $D_{h\ell}(t)$ are equivalent and equal to the disconnected light-heavy correlator.
- $D_{hh}(t)$ is the disconnected heavy-heavy correlator.
- $C_{hh}(t)$ is the connected heavy-heavy correlator.

The placement of N_ℓ and N_h does coincide with the factors in the $\eta - \eta'$ mixing literature, but also connect to a consistency check one can do in the case where the light and heavy quarks are mass degenerate. In this case, the distinction between light (ℓ) and heavy (h) becomes irrelevant, and we have:

$$\begin{pmatrix} N_\ell D(t) - C(t) & \sqrt{N_\ell N_h} D(t) \\ \sqrt{N_\ell N_h} D(t) & N_h D(t) - C(t) \end{pmatrix} \tag{B.26}$$

If we diagonalize this matrix, we find the eigenvalues $-C(t)$ and $(N_\ell + N_h)D(t) - C(t)$. This makes sense: we started in the basis which is correct if there is no mixing between

the σ_L and σ_H, the fully mass-split case. We then assumed that we had degenerate light and heavy quarks. In this case, we saw before that we know we should have two states: the $a_{0,\eta}$ and the true σ. The eigenvalues confirm this: $-C(t)$ corresponds to the $a_{0,\eta}$ (as well as any other a_0, which is the scalar charged under the full $SU(N_\ell + N_h)$), and the $(N_\ell + N_h)D(t) - C(t)$ corresponds to the σ, with consistent normalization as we had for the σ_L (for the $SU(N_\ell)$) and the σ_H (for the $SU(N_h)$).

Staggered Fermions, Vacuum Subtracting

This process generalizes simply to staggered fermions. Because the staggered Dirac matrix corresponds to four fermions in the continuum, we simply need to replace the factors of N_ℓ and N_h with $N_\ell/4$ and $N_h/4$, respectively. In the 4+8 case, this means we need to construct the following correlator matrix:

$$\mathcal{C}(t) = \begin{pmatrix} D_{\ell\ell}(t) - C_{\ell\ell}(t) & \sqrt{2}D_{\ell h}(t) \\ \sqrt{2}D_{h\ell}(t) & 2D_{hh}(t) - C_{hh}(t) \end{pmatrix}. \tag{B.27}$$

The next issue is addressing the vacuum subtraction. Understanding why addressing the vacuum subtraction is important requires stepping back and understanding why the variational analysis works. If we assume that the chiral condensate operator we write down only couples to the σ and the $a_{0,\eta}$, and that we've perfectly subtracted the vacuum subtraction, one would have

$$D_{\ell\ell}(t) - C_{\ell\ell}(t) = (f_\sigma \sin\theta)(f_\sigma \sin\theta)\, e^{-m_\sigma t} + (f_{a_0}\cos\theta)(f_{a_0}\cos\theta)\, e^{-m_{a_0} t}, \tag{B.28}$$

$$\sqrt{2}D_{\ell h}(t) = -(f_\sigma \sin\theta)(f_\sigma \cos\theta)\, e^{-m_\sigma t} + (f_{a_0}\sin\theta)(f_{a_0}\cos\theta)\, e^{-m_{a_0} t}, \tag{B.29}$$

$$D_{\ell\ell}(t) - C_{\ell\ell}(t) = (f_\sigma \cos\theta)(f_\sigma \cos\theta)\, e^{-m_\sigma t} + (f_{a_0}\sin\theta)(f_{a_0}\sin\theta)\, e^{-m_{a_0} t}. \tag{B.30}$$

If we diagonalize this, as before, we find the eigenvalues and corresponding eigenvectors

$$f_\sigma^2 e^{-m_\sigma t}, \begin{pmatrix} -\sin\theta \\ \cos\theta \end{pmatrix}; \qquad f_{a_0}^2 e^{-m_{a_0} t}, \begin{pmatrix} \cos\theta \\ \sin\theta \end{pmatrix}, \tag{B.31}$$

which makes clear the idea that there's mixing involved. To avoid questions of operator normalization, however, normally a variational analysis is pursued where the matrix $\mathcal{C}^{-1}(t_0)\mathcal{C}(t_0+t)$, where t_0 is some reference time, is diagonalized instead of $\mathcal{C}(t)$. This procedure is documented in [102]. A calculation of the eigenvalues and eigenvectors of $\mathcal{C}^{-1}(t_0)\mathcal{C}(t_0+t)$ gives the result

$$e^{-m_\sigma t}, \begin{pmatrix} -\sin\theta \\ \cos\theta \end{pmatrix}; \qquad e^{-m_{a_0} t}, \begin{pmatrix} \cos\theta \\ \sin\theta \end{pmatrix}. \tag{B.32}$$

We see that this construction maintains the same eigenvectors, as well as the same eigenvalues, up to rescaling away of the f factors.

Unfortunately, in reality, there are excited states involved in the measurements of all correlators. To more reliably project onto the ground state, it can help to consider various fermion sources as discussed in section 4.7.

We can, however, avoid the issue of the vacuum subtraction by considering finite differences $\mathcal{C}'(t) \equiv \mathcal{C}(t) - \mathcal{C}(t+1)$. This removes the vacuum subtraction contribution entirely as noted in section 4.5, and only rescales the leading coefficients. The ability to extract a mass is unchanged.

C Analysis of Measurements

C.1 Generalized Effective Masses

The works of [103] and [104] provide a way to generalize effective masses to an arbitrary number of states. To begin this discussion, we start from Eqn. 3.4,

$$\begin{aligned} C_{\mathcal{O}}(t) &= \left(\sum_n a_n e^{-E_n^a t}\right) + \left(\sum_n b_n (-1)^t e^{-E_n^b t}\right) \\ &= \sum_k f_k \left(\pm e^{m_k}\right)^t . \end{aligned} \tag{C.1}$$

In going from the first to the second line, we combined the decaying and the oscillating terms into a single sum. To make a notational translation to the above cited literature, we note that we can write this in the form:

$$y_n = \sum_{k=1}^{K} a_k x_k^n, \tag{C.2}$$

Where we identify $n = t$, $y_n = C(t)$, $a_k = f_k$, and $x_k = \pm e^{m_k t}$. We also truncate the tower of states and assume there are only K states, a good assumption assuming some states are lost to noise. Our goal is to find the x_k's, because if we can find x_k we have found effective masses for the states in the correlator.

We make a remark that on physical lattices with finite size and periodic boundary conditions, assuming mesonic correlators, Eqn. C.1 takes the form:

$$C(t) = \sum_k f_k \sigma_k^t e^{-mT/2} \cosh(m_k(T/2 - t)), \tag{C.3}$$

where T is the spatial extent of the lattice, and $\sigma_k = \pm 1$, being general to oscillating states from staggered fermions. This is not in the form of Eqn. C.2, due to the time

dependence of the hyperbolic cosine. However, we can put it in the appropriate form of Eqn. C.2 by recalling the following identity for the hyperbolic cosine:

$$\cosh^n(x) = \frac{1}{2^n}\sum_j^n \binom{n}{j}\cosh((n-2j)x), \tag{C.4}$$

where:

$$\binom{n}{j} \equiv \frac{n!}{j!(n-j)!}. \tag{C.5}$$

This identity is not immediately useful because the hyperbolic cosine term in Eqn. C.3 is of the form

$$\cosh(m_k(T/2-t)) \equiv \cosh(nx+y),$$

where we identify $x \equiv m_k$, $n \equiv t$, and $y = m_k T/2$. In particular, the issue is the extra term y. This becomes useful after we generalize the identity in Eqn. C.4.

$$\begin{aligned}
&\frac{1}{2^n}\sum_{j=0}^n \binom{n}{j}\cosh((n-2j)x+y) \\
&= \frac{1}{2^n}\sum_{j=0}^n \binom{n}{j}\left[\cosh((n-2j)x)\cosh(y)+\sinh((n-2j)x)\sinh(y)\right] \\
&= \frac{1}{2^n}\left\{\sum_{j=0}^n \binom{n}{j}\left[\cosh((n-2j)x)\cosh(y)\right] + \sum_{j=0}^n \binom{n}{j}\left[\sinh((n-2j)x)\sinh(y)\right]\right\} \\
&= \frac{\cosh(y)}{2^n}\sum_{j=0}^n \binom{n}{j}\left[\cosh((n-2j)x)\right] \\
&= \cosh(y)\cosh^n(x).
\end{aligned} \tag{C.6}$$

We note that the hyperbolic sine terms will cancel: for even n, the $(n-2j)$ term cancels against the $(n-2(n-j))$ term, and for odd n, the extra term has $n-2j=0$, so it also

cancels out. This updated identity means we do not have to worry about the extra term y: we can handle it.

To put Eqn. C.3 into the form Eqn. C.2, we make the identifications:

$$y_n = \frac{1}{2^{n-1}} \sum_{j=0}^{n-1} \binom{n-1}{j} C(n-2j-1) \tag{C.7}$$

$$a_k = f_k e^{-m_k T/2} \tag{C.8}$$

$$x_k = \sigma_k \cosh m_k \tag{C.9}$$

We can now proceed with the method since we can write the problem in the form:

$$y_n = \sum_{k=1}^{K} a_k x_k^n,$$

where we note $n \geq 1$ due to the definition of y_n.

We have assumed that we want to fit K states, thus, we want to solve for k parameters x_k.

We define the polynomial $P(x)$ by:

$$P(x) = \prod_{k=1}^{K} (x - x_k) \tag{C.10}$$

$$\equiv x^k + \sum_{i=1}^{K} p_i x^{K-i}. \tag{C.11}$$

As a remark, Eqn. C.10 is a Vandermonde polynomial. The coefficients p_i are obtained by expanding the Vandermonde polynomial; the exact expression for them in terms of x_k's is not important for the following discussion. However, if we know the values of the coefficient p_i by some other method, we can find the x_k's. This hinges on the assumption that each x_k is a zero of $P(x)$.

Let us pursue this algebraically. By plugging in x_k and rearranging Eqn. C.11, we get the identity

$$x_k^K = -\sum_{i=1}^{K} p_i x_k^{K-i}, \tag{C.12}$$

and trivially, by multiplying this by x^{m-K}, integer m, we get more identities of the form

$$x_k^m = -\sum_{i=1}^{K} p_i x_k^{m-i}; \qquad m \geq K \tag{C.13}$$

We next note, plugging Eqn. C.13 into Eqn. C.2, where we have relabeled n to m,

$$\begin{aligned} y_m &= \sum_{k=1}^{K} a_k x_k^m \\ &= \sum_{k=1}^{K} a_k \left(-\sum_{i=1}^{K} p_i x_k^{m-i} \right) \\ &= -\sum_{i=1}^{K} p_i \sum_{k=1}^{K} a_k x_k^{m-i} \\ &= -\sum_{i=1}^{K} p_i y_{m-i}. \end{aligned} \tag{C.14}$$

We make a further convenient relabeling i to k for later note:

$$\rightarrow y_m = -\sum_{k=1}^{K} p_k y_{m-k}; \qquad m > K \tag{C.15}$$

We note that the constraint $m > K$ is imposed by the fact y_{m-k} is constrained by $m - k \geq 1, \forall k$.

We can write this in a matrix form:

$$(y_m) = \begin{pmatrix} y_{m-1} & y_{m-2} & \dots & y_{m-K} \end{pmatrix} \begin{pmatrix} p_1 \\ p_2 \\ \vdots \\ p_K \end{pmatrix} \tag{C.16}$$

In this form, we have an under-constrained matrix equation—there isn't enough information to uniquely determine the p_k's. We can generate more equations of the form Eqn. C.16, however, by noting the choice of m, so long as $m > K$, is arbitrary (up to the size of the lattice). We can expand this matrix equation:

$$\begin{pmatrix} y_M \\ y_{M+1} \\ \vdots \\ y_N \end{pmatrix} = \begin{pmatrix} y_{M-1} & y_{M-2} & \cdots & y_{M-K} \\ y_M & y_{M-1} & \cdots & y_{M-K+1} \\ \vdots & \vdots & \ddots & \vdots \\ y_{N-1} & y_{N-2} & \cdots & y_{N-K} \end{pmatrix} \begin{pmatrix} p_1 \\ p_2 \\ \vdots \\ p_K \end{pmatrix} \tag{C.17}$$

$$\mathbf{h} = \mathbf{H}\mathbf{p} \tag{C.18}$$

We have made some new implicit definitions. M is constrained such that $M > K$. We note that the matrix $\mathbf{H}$ has dimensions $(N - M + 1) \times K$. For this to be an exactly constrained equation with a unique solution, we need $N - M + 1 = K$. Excitingly, we can also make this an over-constrained system by instead having $N - M + 1 > K$. We remark that, in the case of a hyperbolic cosine correlator, it takes $N + 1$ values of $C(t)$ to construct each y_n.

To summarize the basic constraints in compact form:

$$M > K \tag{C.19}$$

$$N \geq M + K + 1 \tag{C.20}$$

$$N \leq T \tag{C.21}$$

We make the observation that keeping K constant, increasing M and N by 1, and shifting the correlator by 1, the matrix system remains the same. In some regards, M is redundant, and we will set:

$$M \equiv K + 1. \tag{C.22}$$

For the general exactly- or over- constrained system Eqn. C.26, we solve for $\mathbf{p}$ by minimizing:

$$f(\mathbf{p}) = ||\mathbf{Hp} - \mathbf{h}||_2 \tag{C.23}$$

We make two remarks on this:

1. Since the components of $\mathbf{H}$ and $\mathbf{h}$ are noisy and potentially correlated, care should be taken while performing this minimization (such as actually performing the minimization with the effects of a variance-covariance matrix). Since both $\mathbf{H}$ and $\mathbf{h}$ are dependent variables, it is not trivial to properly re-weight $f(\mathbf{p})$ with covariances, though it could be possible to derive it from [105]. For our purposes, this method is being used to get good initial guesses to properly correlated non-linear fits, so we will intentionally neglect correlations here.

2. It is noted in equation 23 of [104] that a singular value cut can be performed on $\mathbf{H}$ to effectively reduce K. The subsequent minimization of Eqn. C.23 can be interpreted as minimizing $\mathbf{p}$ in the subspace of the remaining singular values. Further details and references can be found in section 3.2 of [104].

Once we have solved for the components of $\mathbf{p}$, we can form the polynomial $P(x)$ as defined in Eqn. C.11. We recall, by construction, the roots of $P(x)$ are the x_k as defined in Eqn. C.9:

$$x_k = \sigma_k \cosh m_k$$

Of course, due to noise we may not resolve all roots, and we may find some x_k that are meaningless. In general, we save x_k satisfying $x_k > 1$ (and $x_k < 1$ in the context of the oscillating modes of staggered fermions), and discard the others as noise. We do note, however, that if a fit using $K = 5$, for example, only gives 2 legitimate solutions, it does

not mean that $K = 2$ will give the same two solutions. Tuning K and N is not necessarily a systematic task, and since the results are used as initial guesses to nonlinear fits, we are not concerned by this lack of a systematic approach.

For the sake of discussion, let us assume that we have resolved our x_k's. We can now use this data to find the amplitudes, a_k. We note, in analogy to Eqn. C.16, we can write Eqn. C.2 as a matrix equation as well:

$$(y_n) = \begin{pmatrix} x_1^n & x_2^n & \dots & x_K^n \end{pmatrix} \begin{pmatrix} a_1 \\ a_2 \\ \vdots \\ a_K \end{pmatrix} \tag{C.24}$$

Assuming we have chosen $M = K + 1$, we have computed y_n for all n s.t. $1 \leq n \leq N$. This allows us to write another over-constrained matrix equation for the coefficients a_k:

$$\begin{pmatrix} y_1 \\ y_2 \\ \vdots \\ y_N \end{pmatrix} = \begin{pmatrix} x_1 & x_2 & \dots & x_K \\ x_1^2 & x_2^2 & \dots & x_K^2 \\ \vdots & \vdots & \ddots & \vdots \\ x_1^N & x_2^N & \dots & x_K^N \end{pmatrix} \begin{pmatrix} a_1 \\ a_2 \\ \vdots \\ a_K \end{pmatrix} \tag{C.25}$$

$$\mathbf{y} = \mathbf{X}\mathbf{a} \tag{C.26}$$

We explicitly note that $\mathbf{X}$ is an $N \times K$ matrix, which is by construction over-constrained as $N \geq M + K + 1$. This can be solved in the same way as Eqn. C.23 for the amplitudes a_k. We decline to comment on performing SVD cuts on this over-constrained system, independent or dependent on performing singular value cuts in the matrix $\mathbf{H}$, for the time being.

For the sake of discussion, we have assumed that all x_k roots are resolved, in the sense that all $x_k > 1$ (or < -1 for staggered). We note that even if only a subset of these x_k have been resolved (say, 2 of 4), we use all of the x_k (resolved or otherwise) to find the a_k values. We find, in general, that the a_k's corresponding to the well-resolved x_k also tend to be well resolved, even though "poorly resolved" x_k's were also used in the computation.

We note that, in some regards, we have been lazy in our definition of a_k. Depending on which window the N (or $N+1$) values of $C(t)$ are picked from, the values of a_k may need to be multiplicatively normalized to compare them between different windows. In practice, for the hyperbolic cosine form, this multiplicative factor for a window centered at t is $\mathrm{sech}(T/2-t+1)$, where the $+1$ comes from our convention that we start at y_1, not y_0.

In any case—with the x_k's and a_k's, and multiplicative factors properly accounted for, we now have initial guesses for a non-linear fit to the form in Eqn. C.3. In general, these initial guesses come from looking at multiple values of K, N, and the individual possible windows of $C(t)$ to fit to.

One may attempt to perform a quick jackknife error analysis on these masses and amplitudes, but this is certainly non-trivial—the small fluctuations between the jackknife blocks and the full dataset are likely to be enough to change, in some cases, which x_k are resolved (in general, excited states are sensitive to this), making matching masses across different jackknife blocks difficult.

C.2 Folding, Parity Projections, Finite Differences

There are a handful of methods we have made reference to in previous sections of this chapter which can be used to attempt to improve the quality of a fit or analytically suppress parity partners when finding effective masses. We will define these methods here.

C.2.1 Folding

Recall the general form of a staggered meson correlator for an arbitrary number of direct and oscillating states:

$$\sum_{i=1}^{n} A_i \cosh\left(M_i^a\left(T/2-t\right)\right) + \sum_{j=1}^{m} B_j(-1)^t \cosh\left(M_j^b\left(T/2-t\right)\right), \tag{C.27}$$

This functional form has a symmetry around $t = T/2$ for the direct state and the oscillating state. To improve the quality of our measured data, y_t^i, we can impose this symmetry by the process of "folding." Folding is defined by

$$y_t^i \to y_t^{i'} = \frac{1}{2}\left(y_t^i + y_{T-t}^i\right), \tag{C.28}$$

where as needed we define $y_T^i = y_0^i$. We can then bin, form the mean and covariance of these folded y_t^i's, and perform fits to the data. As a remark, there is no benefit (nor is it numerically stable) to include two points that are symmetric under this interchange in a correlated fit.

C.2.2 Parity Projection

As we remarked when discussing staggered meson correlators in section 3.1, it is impossible to separate a direct state from its oscillating parity partner state. It is possible to algebraically suppress the effect of the oscillating state or of the direct state [106]. This process is known as positive (or negative) parity projection.

For simplicity, we consider a correlator with a single direct and a single oscillating state:

$$C(t) = A_1 \cosh\left(M_1^a\left(T/2 - t\right)\right) + B_1(-1)^t \cosh\left(M_1^b\left(T/2 - t\right)\right). \tag{C.29}$$

We define positive parity projection via

$$C^+(t) \equiv \frac{1}{4}\left(C(t-1) + 2C(t) + C(t+1)\right), \tag{C.30}$$

where the behavior at $t = 0$ is in general undefined, though we take the convention $C(0) = \frac{1}{4}\left(C(T-1) + 2C(0) + C(1)\right)$. In terms of $C(t)$, $C^+(t)$ is parameterized by

$$\begin{aligned} C^+(t) = A_1 \left(\frac{1 + \cosh(M_1^a)}{2}\right) \cosh\left(M_1^a\left(T/2 - t\right)\right) + \\ B_1 \left(\frac{1 - \cosh(M_1^b)}{2}\right) (-1)^t \cosh\left(M_1^b\left(T/2 - t\right)\right), \end{aligned} \tag{C.31}$$

where we see that the direct state has been amplified by an $\mathcal{O}(1)$ factor while the oscillating state has been suppressed by a factor of $\mathcal{O}\left(\left(M_1^b\right)^2\right)$. Thus, for small values of the masses, the direct state grows in amplitude, while the oscillating state is suppressed.

Positive parity projection can be applied to the measured correlator data y_t^i, and again we can subsequently compute the mean and covariance of the positive parity projected data. Projection may make it possible to perform fits to $\overline{y}_t^+$ with a single direct state or at minimum to find good quality initial guesses for the direct state via effective masses.

As a remark, it is possible to define a negative parity projection which amplifies the oscillating state. This can be defined via

$$C^-(t) \equiv \frac{(-1)^t}{4}\left(-C(t-1)+2C(t)-C(t+1)\right), \tag{C.32}$$

where as a convention the prefactor of $(-1)^t$ interchanges the original direct and oscillating states. Quick algebra shows

$$\begin{aligned} C^-(t) = B_1\left(\frac{1+\cosh(M_1^b)}{2}\right)\cosh\left(M_1^b\left(T/2-t\right)\right) + \\ A_1\left(\frac{1-\cosh(M_1^a)}{2}\right)(-1)^t\cosh\left(M_1^a\left(T/2-t\right)\right). \end{aligned} \tag{C.33}$$

This construction can be applied to the measured correlator data and be used similarly to positive parity projection.

As a remark, the label "projector" may be a bit misleading because these algebraic operations suppress oscillating or direct states as opposed to eliminating them. They are projectors in the linear algebra sense that

$$C(t) = C^+(t) + (-1)^t C^-(t), \tag{C.34}$$

showing that we can reconstruct the original data from the two projected sets.

C.2.3 Finite Differences

As an alternative analysis method, it can also be useful to look at finite differences of the correlators. This technique becomes especially useful when fitting the 0^{++} as we will discuss in section 4.5. Again, we will consider a correlator with a single direct and a single oscillating state:

$$C(t) = A_1 \cosh\left(M_1^a\left(T/2 - t\right)\right) + B_1(-1)^t \cosh\left(M_1^b\left(T/2 - t\right)\right). \tag{C.35}$$

We can define finite difference correlator for half-integer t by

$$C'(t) = C(t - \frac{1}{2}) - C(t + \frac{1}{2}), \tag{C.36}$$

In terms of $C(t)$, $C'(t)$ can be parameterized by

$$\begin{aligned} C'(t) = 2A_1 \sinh\left(\frac{M_1^a}{2}\right) \sinh\left(M_1^a\left(T/2 - t\right)\right) + \\ 2B_1\left(-1\right)^{t-\frac{1}{2}} \cosh\left(\frac{M_1^b}{2}\right) \cosh\left(M_1^b\left(T/2 - t\right)\right). \end{aligned} \tag{C.37}$$

We remark that the finite difference amplifies the oscillating state compared to the direct state.

As we will see when discussing the 0^{++}, there are some cases where we are interested in fitting a free constant in addition to a decaying state. We can prove that when performing fully correlated fits, it is equivalent to fit the finite differences instead. While the details of the proof of this statement are complicated and rather unilluminating, every detail is included in appendix C.3.

There are still benefits to the finite difference. In cases where a full covariance is not used, such as initial guesses, the amplifying features of finite differences can help. The equivalence between fits to functional forms with a free constant and to finite differences does not hold with uncorrelated fits, in which case an uncorrelated fit can benefit from the

finite difference. As we saw in section 4.5, we use uncorrelated fits with finite differences in extracting the mass of the 0^{++}.

C.3 Finite Difference Fit Equivalence

In this section consider fits to correlated data y_i to the functional form $f(\vec{\alpha}; t_i) + c$, where $\vec{\alpha}$ and c are free fit parameters and t_i are the independent variables of the fit. We make no assumption that the fit is linear in $\vec{\alpha}$. We will show that it is equivalent to fit to the finite differences of the data, that is, performing a fit of $y_{i+1} - y_i$ to the functional form $f(\vec{\alpha}; t_{i+1}) - f(\vec{\alpha}; t_i)$. Further, we show the correlated χ^2 function one can write down has the same minimum with respect to the parameters $\vec{\alpha}$, and even takes the same value there.

C.3.1 Definitions

Let us assume that we have a set of data $y_i, i = 1 \cdots N$, as a function of independent variables t_i with a covariance matrix $\sigma^2_{i,j}$. We will definite the inverse of the covariance, in an abuse of notation, as $\sigma^{-2}_{i,j}$. If we assume that the data can be described by a fit ansatz $y_i = f(\vec{\alpha}, t_i) + c$, where $\vec{\alpha}$ and c are fit parameters (where we do *not* assume f is linear in $\vec{\alpha}$), we can define a correlated non-linear least squares problem by minimizing the χ^2 function:

$$\chi^2(\vec{\alpha}, c) = \sum_{i=1}^{N} \sum_{j=1}^{N} (y_i - f(\vec{\alpha}, t_i) - c)\, \sigma^{-2}_{i,j}\, (y_j - f(\vec{\alpha}, t_j) - c) \tag{C.38}$$

Alternatively, we can consider the fits of the finite differences of the data, $\tilde{y}_i \equiv y_{i+1} - y_i, i = 1 \cdots N-1$, where we fit it to the form $\tilde{f}(\alpha; t_{i+1}, t_i) \equiv f(\alpha, t_{i+1}) - f(\alpha, t_i)$ (where we note that the parameter c cancels). The data $\tilde{y}_i$ has a covariance $\tilde{\sigma}^2_{ij}$, which one can show is a function of σ^2_{ij}. As before, we can define a non-linear least squares problem by minimizing the $\tilde{\chi}^2$ function:

$$\tilde{\chi}^2(\vec{\alpha}) = \sum_{i=1}^{N-1}\sum_{j=1}^{N-1}\left(\tilde{y}_i - \tilde{f}(\vec{\alpha};t_{i+1},t_i)\right)\tilde{\sigma}_{i,j}^{-2}\left(\tilde{y}_j - \tilde{f}(\vec{\alpha};t_{j+1},t_j)\right) \tag{C.39}$$

$$= \sum_{i=1}^{N-1}\sum_{j=1}^{N-1}\left(y_{i+1} - y_i - f(\vec{\alpha};t_{i+1}) + f(\vec{\alpha};t_i)\right)\tilde{\sigma}_{i,j}^{-2}\left(y_{j+1} - y_j - f(\vec{\alpha};t_{j+1}) + f(\vec{\alpha};t_j)\right) \tag{C.40}$$

To clarify, we will show that the minimum values of $\vec{\alpha}$ are equivalent for χ^2 and $\tilde{\chi}^2$. Further, once we know the minimum $\vec{\alpha}$, we can compute the minimum c, and from that show that both χ^2 and $\tilde{\chi}^2$ are equal at the minimum.

There is a certain amount of intuition to this: we conserve the number of degrees of freedom between the two fits. The finite difference fit has one less data point but also one less fit parameter, c. It would be inconsistent if the finite difference fit gave a more or less acceptable fit (with respect to a quantity such as a p-value, for example). As we will see quickly, though, the proof becomes nontrivial.

C.3.2 Naive Approach: Simplify $\tilde{\chi}^2$

To illuminate some of the issues, let us begin to simplify $\tilde{\chi}^2$ by breaking it into terms that "look" like χ^2.

$$\tilde{\chi}^2(\vec{\alpha}) \tag{C.41}$$

$$= \sum_{i=1}^{N-1}\sum_{j=1}^{N-1} \left(y_{i+1} - y_i - f(\vec{\alpha}; t_{i+1}) + f(\vec{\alpha}; t_i)\right) \tilde{\sigma}_{i,j}^{-2} \left(y_{j+1} - y_j - f(\vec{\alpha}; t_{j+1}) + f(\vec{\alpha}; t_j)\right) \tag{C.42}$$

$$= \sum_{i=1}^{N-1}\sum_{j=1}^{N-1} \Big[(y_{i+1} - f(\alpha, t_{i+1}))\tilde{\sigma}_{i,j}^{-2}(y_{j+1} - f(\alpha, t_{j+1})) \tag{C.43}$$

$$+ (y_i - f(\alpha, t_i))\tilde{\sigma}_{i,j}^{-2}(y_j - f(\alpha, t_j)) \tag{C.44}$$

$$- (y_{i+1} - f(\alpha, t_{i+1}))\tilde{\sigma}_{i,j}^{-2}(y_j - f(\alpha, t_j)) \tag{C.45}$$

$$- (y_i - f(\alpha, t_i))\tilde{\sigma}_{i,j}^{-2}(y_{j+1} - f(\alpha, t_{j+1}))\Big] \tag{C.46}$$

$$= \sum_{i=2}^{N}\sum_{j=2}^{N} \Big[(y_i - f(\alpha, t_i))\tilde{\sigma}_{i-1,j-1}^{-2}(y_j - f(\alpha, t_j))\Big] \tag{C.47}$$

$$+ \sum_{i=1}^{N-1}\sum_{j=1}^{N-1} \Big[(y_i - f(\alpha, t_i))\tilde{\sigma}_{i,j}^{-2}(y_j - f(\alpha, t_j))\Big] \tag{C.48}$$

$$- \sum_{i=2}^{N}\sum_{j=1}^{N-1} \Big[(y_i - f(\alpha, t_i))\tilde{\sigma}_{i-1,j}^{-2}(y_j - f(\alpha, t_j))\Big] \tag{C.49}$$

$$- \sum_{i=1}^{N-1}\sum_{j=2}^{N} \Big[(y_i - f(\alpha, t_i))\tilde{\sigma}_{i,j-1}^{-2}(y_j - f(\alpha, t_j))\Big] \tag{C.50}$$

It's here that we get stuck because we don't know what the inverse of the finite difference correlation function is.

One conceivable approach is to find the covariance matrix of the finite differences and then find a closed form expression for its inverse. This is entirely possible—closed form expressions for elements of an inverse exist, although in the form of a determinants of minors of the original matrix, which may make it difficult to simplify. Alternatively, we will motivate a trick below to directly compute the elements of the inverse. We will do the latter trick, but first it requires some motivation.

Inverse Finite Difference Covariance: Warm Up

As a warm up, we will consider two correlated Gaussian variables, x_1 and x_2 with zero mean and the covariance matrix:

$$\sigma_{ij}^2 = \begin{pmatrix} A & B \\ B & A \end{pmatrix},$$

which has an inverse:

$$\sigma_{ij}^{-2} = \frac{1}{A^2 - B^2} \begin{pmatrix} A & -B \\ -B & A \end{pmatrix}.$$

The variables x_1 and x_2 have a normalized probability distribution function:

$$P(x_1, x_2) = \frac{1}{\sqrt{4\pi^2 \det(\sigma^2)}} \exp\left(-\frac{1}{2}\sum_{i,j} x_i \sigma_{i,j}^{-2} x_j\right) \tag{C.51}$$

$$= \frac{1}{2\pi\sqrt{A^2 - B^2}} \exp\left(-\frac{Ax_1^2 - 2Bx_1x_2 + Ax_2^2}{2(A^2 - B^2)}\right) \tag{C.52}$$

One could ask the question: what is the probability distribution of the difference of x_1 and x_2? Obviously it has a mean of 0 since both x_1 and x_2 did, but we don't necessarily know what its variance is. We can use a trick to find the probability distribution of the difference $v \equiv x_2 - x_1$:

$$P(v) = \int_{-\infty}^{\infty} dx_1 \int_{-\infty}^{\infty} dx_2 P(x_1, x_2)\delta(v - (x_2 - x_1)) \tag{C.53}$$

$$= \int_{-\infty}^{\infty} dx_1 P(x_1, v + x_1) \tag{C.54}$$

$$= \int_{-\infty}^{\infty} dx_1 \frac{1}{2\pi\sqrt{A^2 - B^2}} \exp\left(-\frac{Ax_1^2 - 2Bx_1(v + x_1) + A(v + x_1)^2}{2(A^2 - B^2)}\right) \tag{C.55}$$

$$= \frac{1}{2\pi\sqrt{A^2 - B^2}} \int_{-\infty}^{\infty} dx_1 \exp\left(-\frac{x_1^2}{A + B} - \frac{vx_1}{A + B} - \frac{Av^2}{2(A^2 - B^2)}\right) \tag{C.56}$$

$$= \frac{1}{2\sqrt{\pi\,(A - B)}} \exp\left(-\frac{v^2}{4(A - B)}\right) \tag{C.57}$$

$$\tag{C.58}$$

We see that we have a properly normalized probability distribution function for v which consistently predicts a variance of $2(A - B)$. This δ-function trick we started from will be the cornerstone of deriving $\tilde{\sigma}^{-2}$.

As a remark, we note that even if the mean values of x_1, x_2 were non-zero, it would not effect the value of the variance. This follows by the definition of the variance—it is the deviation *around* the mean. As such, when we apply this trick to the set of data y_i, we will ignore the means of the data.

Inverse Finite Difference Covariance: The Real Deal

Following as before (and using the trick that the means do not effect the covariance), the probability distribution function for the full set of variables $y_i, i = 1 \cdots N$ with covariance σ_{ij}^2 is:

$$P(y_1, \cdots, y_N) = \frac{1}{\sqrt{(2\pi)^N \det(\sigma^2)}} \exp\left(-\frac{\sum_{i,j=1}^{N} y_i \sigma_{i,j}^{-2} y_j}{2}\right) \tag{C.59}$$

In the interest of notational conciseness (and sanity), we will drop the normalization on probability distribution functions from now on. We will now use the same δ-function trick to change variables to the finite differences: $\tilde{y}_i \equiv y_{i+1} - y_i, i = 1 \cdots N - 1$.

$$P(\tilde{y}_1, \cdots, \tilde{y}_{N-1}) = \int dy_1 \cdots dy_N P(y_1, \cdots, y_N) \prod_{i=1}^{N-1} \delta(\tilde{y}_i - y_{i+1} + y_i), \tag{C.60}$$

This chain of delta functions reduces to integrating over y_2 to y_N, with the substitution $y_i = y_1 + \sum_{j=1}^{i-1} \tilde{y}_j$ for all $i \geq 2$. This leaves a single variable to integrate over, y_1. We remark that we are going to drop the normalization constant from here on out: it does not help us find the covariance of the $\tilde{y}_i$, and as such its just a notational burden. We will use the symbol $\approx$ to indicate when we've dropped some normalization between lines.

$$P(\tilde{y}_1, \cdots, \tilde{y}_{N-1}) \tag{C.61}$$

$$= \int dy_1 \cdots dy_N P(y_1, \cdots, y_N) \prod_{i=1}^{N-1} \delta(\tilde{y}_i - y_{i+1} + y_i) \tag{C.62}$$

$$\approx \int_{-\infty}^{\infty} dy_1 \exp\left(- \frac{\sum_{i,j=1}^{N} (y_1 + \sum_{k=1}^{i-1} \tilde{y}_k) \sigma_{i,j}^{-2} (y_1 + \sum_{\ell=1}^{i-1} \tilde{y}_\ell)}{2} \right) \tag{C.63}$$

$$= \int_{-\infty}^{\infty} dy_1 \exp\left(- \frac{y_1^2 \left(\sum_{i,j=1}^{N} \sigma_{i,j}^{-2} \right) + 2 y_1 \sum_{i,j=1}^{N} \left(\sigma_{i,j}^{-2} \sum_{k=1}^{i-1} \tilde{y}_k \right) + \sum_{i,j=1}^{N} \left(\left(\sum_{k=1}^{i-1} \tilde{y}_k \right) \sigma_{i,j}^{-2} \left(\sum_{\ell=1}^{j-1} \tilde{y}_\ell \right) \right)}{2} \right) \tag{C.64}$$

$$\approx \exp\left(- \frac{\left[\sum_{i,j=1}^{N} \sigma_{i,j}^{-2} \right] \left[\sum_{i,j=1}^{N} \left(\left(\sum_{k=1}^{i-1} \tilde{y}_k \right) \sigma_{i,j}^{-2} \left(\sum_{\ell=1}^{j-1} \tilde{y}_\ell \right) \right) \right] - \left[\sum_{i,j=1}^{N} \sigma_{i,j}^{-2} \left(\sum_{\ell=1}^{j-1} \tilde{y}_\ell \right) \right]^2}{2 \sum_{i,j=1}^{N} \sigma_{i,j}^{-2}} \right) \tag{C.65}$$

To read off the inverse of the covariance matrix for the $\tilde{y}_i$'s, all we need to do is rewrite Eqn. C.65 as a quadratic form.

Let us first consider the term:

$$\sum_{i,j=1}^{N} \left(\left(\sum_{k=1}^{i-1} \tilde{y}_k \right) \sigma_{i,j}^{-2} \left(\sum_{\ell=1}^{j-1} \tilde{y}_\ell \right) \right). \tag{C.66}$$

Our trick will be to interchange the order of the summations, which is difficult because the inner sum is a function of the outer sum. Let us consider a fixed value for k and ℓ. In the sum over i and j, $\tilde{y}_k \tilde{y}_\ell$ only contributes if $k < i$ and $\ell < j$. We can use this observation to rewrite said term as:

$$\sum_{i,j=1}^{N}\left(\left(\sum_{k=1}^{i-1}\tilde{y}_k\right)\sigma_{i,j}^{-2}\left(\sum_{\ell=1}^{j-1}\tilde{y}_\ell\right)\right)=\sum_{k=1}^{N-1}\sum_{\ell=1}^{N-1}\tilde{y}_k\tilde{y}_\ell\left(\sum_{i=k+1}^{N}\sum_{j=\ell+1}^{N}\sigma_{i,j}^{-2}\right). \tag{C.67}$$

This is explicitly a quadratic form in $\tilde{y}_i$. Let us now consider the second (squared) term in Eqn. C.65.

$$\sum_{i,j=1}^{N}\sigma_{i,j}^{-2}\left(\sum_{\ell=1}^{j-1}\tilde{y}_\ell\right) \tag{C.68}$$

In the sum over i and j, the term $\tilde{y}_\ell$ contributes if $\ell < j$. We can use this to rewrite said term as:

$$\sum_{i,j=1}^{N}\sigma_{i,j}^{-2}\left(\sum_{\ell=1}^{j-1}\tilde{y}_\ell\right)=\sum_{\ell=1}^{N-1}\tilde{y}_\ell\left(\sum_{j=1}^{N}\sum_{i=\ell+1}^{N}\sigma_{i,j}^{-2}\right), \tag{C.69}$$

This is clearly a linear form in $\tilde{y}_i$ which is squared, giving a quadratic form. Now that we have rewritten all terms in Eqn. C.65 as a quadratic form, we can explicitly write it (using the liberty to relabel indices) to make the total quadratic form manifestly explicit.

$$P(\tilde{y_1},\cdots,\tilde{y}_{N-1}) \tag{C.70}$$

$$\approx \exp\left(-\frac{\sum_{k=1}^{N-1}\sum_{\ell=1}^{N-1}\tilde{y}_k\tilde{y}_\ell\left[\sum_{j=1}^{N}\sum_{a=1}^{N}\sum_{i=k+1}^{N}\sum_{b=\ell+1}^{N}\left(\sigma_{a,j}^{-2}\sigma_{b,i}^{-2}-\sigma_{i,j}^{-2}\sigma_{a,b}^{-2}\right)\right]}{2\sum_{c=1}^{N}\sum_{d=1}^{N}\sigma_{c,d}^{-2}}\right) \tag{C.71}$$

We can now read off the inverse of the covariance matrix for the finite difference variables, $\tilde{y}_i$ from Eqn. C.71:

$$\tilde{\sigma}_{k,\ell}^{-2}=\frac{\sum_{j=1}^{N}\sum_{a=1}^{N}\sum_{i=k+1}^{N}\sum_{b=\ell+1}^{N}\left(\sigma_{a,j}^{-2}\sigma_{b,i}^{-2}-\sigma_{i,j}^{-2}\sigma_{a,b}^{-2}\right)}{\sum_{c=1}^{N}\sum_{d=1}^{N}\sigma_{c,d}^{-2}} \tag{C.72}$$

Now that we have this closed form inverse, we can return to simplifying the finite difference $\tilde{\chi}^2$.

Continuing to simplify $\tilde{\chi}^2$

As we were, now that we can plug in the inverse of the finite difference covariance. As a note, for notational conciseness, we will be defining:

$$\epsilon_k \equiv y_k - f(\vec{\alpha}; t_k). \tag{C.73}$$

Pressing on:

$$\begin{aligned}
\tilde{\chi}^2(\vec{\alpha}) =& \sum_{k=2}^{N}\sum_{\ell=2}^{N}\Big[(y_k - f(\alpha,t_k))\tilde{\sigma}^{-2}_{k-1,\ell-1}(y_\ell - f(\alpha,t_\ell))\Big] && \text{(C.74)}\\
&+ \sum_{k=1}^{N-1}\sum_{\ell=1}^{N-1}\Big[(y_k - f(\alpha,t_k))\tilde{\sigma}^{-2}_{k,\ell}(y_\ell - f(\alpha,t_\ell))\Big] && \text{(C.75)}\\
&- \sum_{k=2}^{N}\sum_{\ell=1}^{N-1}\Big[(y_k - f(\alpha,t_k))\tilde{\sigma}^{-2}_{k-1,\ell}(y_\ell - f(\alpha,t_\ell))\Big] && \text{(C.76)}\\
&- \sum_{k=1}^{N-1}\sum_{\ell=2}^{N}\Big[(y_k - f(\alpha,t_k))\tilde{\sigma}^{-2}_{k,\ell-1}(y_\ell - f(\alpha,t_\ell))\Big] && \text{(C.77)}\\
=& \sum_{k=2}^{N}\sum_{\ell=2}^{N}\left[\epsilon_k\left[\frac{\sum_{j=1}^{N}\sum_{a=1}^{N}\sum_{i=k}^{N}\sum_{b=\ell}^{N}\left(\sigma^{-2}_{a,j}\sigma^{-2}_{b,i} - \sigma^{-2}_{i,j}\sigma^{-2}_{a,b}\right)}{\sum_{c=1}^{N}\sum_{d=1}^{N}\sigma^{-2}_{c,d}}\right]\epsilon_\ell\right] && \text{(C.78)}\\
&+ \sum_{k=1}^{N-1}\sum_{\ell=1}^{N-1}\left[\epsilon_k\left[\frac{\sum_{j=1}^{N}\sum_{a=1}^{N}\sum_{i=k+1}^{N}\sum_{b=\ell+1}^{N}\left(\sigma^{-2}_{a,j}\sigma^{-2}_{b,i} - \sigma^{-2}_{i,j}\sigma^{-2}_{a,b}\right)}{\sum_{c=1}^{N}\sum_{d=1}^{N}\sigma^{-2}_{c,d}}\right]\epsilon_\ell\right] && \text{(C.79)}\\
&- \sum_{k=2}^{N}\sum_{\ell=1}^{N-1}\left[\epsilon_k\left[\frac{\sum_{j=1}^{N}\sum_{a=1}^{N}\sum_{i=k}^{N}\sum_{b=\ell+1}^{N}\left(\sigma^{-2}_{a,j}\sigma^{-2}_{b,i} - \sigma^{-2}_{i,j}\sigma^{-2}_{a,b}\right)}{\sum_{c=1}^{N}\sum_{d=1}^{N}\sigma^{-2}_{c,d}}\right]\epsilon_\ell\right] && \text{(C.80)}\\
&- \sum_{k=1}^{N-1}\sum_{\ell=2}^{N}\left[\epsilon_k\left[\frac{\sum_{j=1}^{N}\sum_{a=1}^{N}\sum_{i=k+1}^{N}\sum_{b=\ell}^{N}\left(\sigma^{-2}_{a,j}\sigma^{-2}_{b,i} - \sigma^{-2}_{i,j}\sigma^{-2}_{a,b}\right)}{\sum_{c=1}^{N}\sum_{d=1}^{N}\sigma^{-2}_{c,d}}\right]\epsilon_\ell\right] && \text{(C.81)}
\end{aligned}$$

While this expression looks unmanageably complicated, we can systematically push through it to simplify it. These details are even more complicated and not very illuminating, and are left to section C.3.4. After all of the simplifications, we are left with the stunningly simple expression:

$$\tilde{\chi}^2(\vec{\alpha}) = \sum_{k=1}^{N}\sum_{\ell=1}^{N}\left[y_k - f(\vec{\alpha};t_k)\right]\sigma_{k,\ell}^{-2}\left[y_\ell - f(\vec{\alpha};t_\ell)\right] - \frac{\left(\sum_{j=1}^{N}\sum_{k=1}^{N}\left[y_k - f(\vec{\alpha};t_k)\right]\sigma_{k,j}^{-2}\right)^2}{\sum_{c=1}^{N}\sum_{d=1}^{N}\sigma_{c,d}^{-2}} \tag{C.82}$$

For reasons that'll be clear soon, we're going to make the following definition:

$$\mathcal{C}(\vec{\alpha}) \equiv \frac{\left(\sum_{j=1}^{N}\sum_{k=1}^{N}\left[y_k - f(\vec{\alpha};t_k)\right]\sigma_{k,j}^{-2}\right)}{\sum_{c=1}^{N}\sum_{d=1}^{N}\sigma_{c,d}^{-2}}, \tag{C.83}$$

such that

$$\tilde{\chi}^2(\vec{\alpha}) = \sum_{k=1}^{N}\sum_{\ell=1}^{N}\left[y_k - f(\vec{\alpha};t_k)\right]\sigma_{k,\ell}^{-2}\left[y_\ell - f(\vec{\alpha};t_\ell)\right] - \mathcal{C}(\vec{\alpha})^2\sum_{c=1}^{N}\sum_{d=1}^{N}\sigma_{c,d}^{-2} \tag{C.84}$$

Now we need to connect back to the non-finite difference χ^2!

Connecting Back: The Original χ^2

Recall the definition of χ^2 from Eqn. C.38, with convenient relabeling of variables that are summed over:

$$\chi^2(\vec{\alpha}, c) = \sum_{k=1}^{N}\sum_{\ell=1}^{N}\left(y_k - f(\vec{\alpha},t_k) - c\right)\sigma_{k,\ell}^{-2}\left(y_\ell - f(\vec{\alpha},t_\ell) - c\right) \tag{C.85}$$

We can ask the following question: at the minimum of this χ^2, what value does c take? We find:

$$\frac{\partial\chi^2}{\partial c} = 0 \approx \sum_{k=1}^{N}\sum_{\ell=1}^{N}\sigma_{k,\ell}^{-2}\left(y_\ell - f(\vec{\alpha};t_\ell) - c\right) \tag{C.86}$$

$$\rightarrow c = \frac{\sum_{k=1}^{N}\sum_{\ell=1}^{N}\sigma_{k,\ell}^{-2}\left(y_\ell - f(\vec{\alpha};t_\ell)\right)}{\sum_{k=1}^{N}\sum_{\ell=1}^{N}\sigma_{k,\ell}^{-2}} \tag{C.87}$$

We notice that *at the minimum of χ^2, the value for c coincides with the definition of $\mathcal{C}(\vec{\alpha})$ in* Eqn. C.83.

If we constrain ourself to talk about χ^2 at the minimum value for $c = \mathcal{C}(\vec{\alpha})$, we find:

$$\chi^2(\vec{\alpha}, \mathcal{C}(\vec{\alpha})) = \sum_{k=1}^{N}\sum_{\ell=1}^{N} \left(y_k - f(\vec{\alpha}, t_k) - \mathcal{C}(\vec{\alpha})\right) \sigma_{k,\ell}^{-2} \left(y_\ell - f(\vec{\alpha}, t_\ell) - \mathcal{C}(\vec{\alpha})\right) \tag{C.88}$$

$$= \sum_{k=1}^{N}\sum_{\ell=1}^{N} \Big[\left(y_k - f(\vec{\alpha}, t_k)\right) \sigma_{k,\ell}^{-2} \left(y_\ell - f(\vec{\alpha}, t_\ell)\right) - \mathcal{C}(\vec{\alpha}) \sigma_{k,\ell}^{-2} \left(y_\ell - f(\vec{\alpha}, t_\ell)\right) \tag{C.89}$$

$$- \left(y_k - f(\vec{\alpha}, t_k)\right) \sigma_{k,\ell}^{-2} \mathcal{C}(\vec{\alpha}) + \mathcal{C}(\vec{\alpha})^2 \sigma_{k,\ell}^{-2} \Big] \tag{C.90}$$

$$= \sum_{k=1}^{N}\sum_{\ell=1}^{N} \left[y_k - f(\vec{\alpha}, t_k)\right] \sigma_{k,\ell}^{-2} \left[y_\ell - f(\vec{\alpha}, t_\ell)\right] - \mathcal{C}(\vec{\alpha})^2 \sum_{k=1}^{N}\sum_{\ell=1}^{N} \sigma_{k,\ell}^{-2} \tag{C.91}$$

Which *exactly* coincides with our expression for $\tilde{\chi}^2$ in Eqn. C.84, proving our conjecture.

C.3.3 Overview

We started with a set of data $y_i, i = 1 \cdots N$, as a function of independent variables t_i with a covariance matrix $\sigma_{i,j}^2$, which we assume can be described by a fit function $y_i = f(\vec{\alpha}, t_i) + c$, where $\vec{\alpha}$ and c are fit parameters. We defined a correlated non-linear least squares problem by minimizing the χ^2 function defined in Eqn. C.38:

$$\chi^2(\vec{\alpha}, c) = \sum_{i=1}^{N}\sum_{j=1}^{N} \left(y_i - f(\vec{\alpha}, t_i) - c\right) \sigma_{i,j}^{-2} \left(y_j - f(\vec{\alpha}, t_j) - c\right) \tag{C.92}$$

We saw that at the minimum of this χ^2, the fit parameter c takes the value $\mathcal{C}(\alpha)$, defined in Eqn. C.84 by:

$$c_{min} \equiv \mathcal{C}(\vec{\alpha}) = \frac{\left(\sum_{j=1}^{N}\sum_{k=1}^{N} \left[y_k - f(\vec{\alpha}; t_k)\right] \sigma_{k,j}^{-2}\right)}{\sum_{c=1}^{N}\sum_{d=1}^{N} \sigma_{c,d}^{-2}}, \tag{C.93}$$

Which, when plugged back into χ^2, gives us Eqn. C.84:

$$\chi^2(\vec{\alpha}, \mathcal{C}(\vec{\alpha})) = \sum_{k=1}^{N}\sum_{\ell=1}^{N} \left[y_k - f(\vec{\alpha}, t_k)\right] \sigma_{k,\ell}^{-2} \left[y_\ell - f(\vec{\alpha}, t_\ell)\right] - \mathcal{C}(\vec{\alpha})^2 \sum_{k=1}^{N}\sum_{\ell=1}^{N} \sigma_{k,\ell}^{-2} \tag{C.94}$$

Alternatively, we considered the fits of the finite differences of the data, $\tilde{y}_i \equiv y_{i+1} - y_i, i = 1 \cdots N-1$, where we fit it to the form $\tilde{f}(\alpha; t_{i+1}, t_i) \equiv f(\alpha, t_{i+1}) - f(\alpha, t_i)$. The data $\tilde{y}_i$ has a covariance $\tilde{\sigma}_{ij}^2$ which is necessarily a function of σ_{ij}^2. We defined the non-linear least squares problem for the finite differences by minimizing the $\tilde{\chi}^2$ function defined in Eqn. C.39:

$$\tilde{\chi}^2(\vec{\alpha}) = \sum_{i=1}^{N-1} \sum_{j=1}^{N-1} \left(\tilde{y}_i - \tilde{f}(\vec{\alpha}; t_{i+1}, t_i) \right) \tilde{\sigma}_{i,j}^{-2} \left(\tilde{y}_j - \tilde{f}(\vec{\alpha}; t_{j+1}, t_j) \right), \tag{C.95}$$

$$\tag{C.96}$$

which over the course of a long derivation we showed is *exactly* equal to Eqn. C.84, notated $\chi^2(\vec{\alpha}, \mathcal{C}(\vec{\alpha}))$. As a key part of this derivation, we computed the inverse of the covariance matrix of the finite differences as a function of the original covariance matrix given in Eqn. C.72 as:

$$\tilde{\sigma}_{k,\ell}^{-2} = \frac{\sum_{j=1}^{N} \sum_{a=1}^{N} \sum_{i=k+1}^{N} \sum_{b=\ell+1}^{N} \left(\sigma_{a,j}^{-2} \sigma_{b,i}^{-2} - \sigma_{i,j}^{-2} \sigma_{a,b}^{-2} \right)}{\sum_{c=1}^{N} \sum_{d=1}^{N} \sigma_{c,d}^{-2}} \tag{C.97}$$

In short, we showed that it is equivalent, even with correlated variables, to perform a non-linear fit of the original data to a function with a free constant, or to perform a non-linear fit of the finite difference data to the finite difference of the function, so long as the respective covariance matrices are properly defined.

This mathematically confirms what intuition told us early on: since both fits have the same number of degrees of freedom and ask essentially the same question about the parameters $\vec{\alpha}$, both should give the same minimum and should provide an equal fit confidence.

C.3.4 Details of the $\tilde{\chi}^2$ Simplification

.

We start from Eqn. C.74:

$$\tilde{\chi}^2(\vec{\alpha}) = \sum_{k=2}^{N}\sum_{\ell=2}^{N}\Big[(y_k - f(\alpha,t_k))\tilde{\sigma}^{-2}_{k-1,\ell-1}(y_\ell - f(\alpha,t_\ell))\Big] \tag{C.98}$$

$$+ \sum_{k=1}^{N-1}\sum_{\ell=1}^{N-1}\Big[(y_k - f(\alpha,t_k))\tilde{\sigma}^{-2}_{k,\ell}(y_\ell - f(\alpha,t_\ell))\Big] \tag{C.99}$$

$$- \sum_{k=2}^{N}\sum_{\ell=1}^{N-1}\Big[(y_k - f(\alpha,t_k))\tilde{\sigma}^{-2}_{k-1,\ell}(y_\ell - f(\alpha,t_\ell))\Big] \tag{C.100}$$

$$- \sum_{k=1}^{N-1}\sum_{\ell=2}^{N}\Big[(y_k - f(\alpha,t_k))\tilde{\sigma}^{-2}_{k,\ell-1}(y_\ell - f(\alpha,t_\ell))\Big] \tag{C.101}$$

$$= \sum_{k=2}^{N}\sum_{\ell=2}^{N}\left[\epsilon_k\left[\frac{\sum_{j=1}^{N}\sum_{a=1}^{N}\sum_{i=k}^{N}\sum_{b=\ell}^{N}\left(\sigma^{-2}_{a,j}\sigma^{-2}_{b,i} - \sigma^{-2}_{i,j}\sigma^{-2}_{a,b}\right)}{\sum_{c=1}^{N}\sum_{d=1}^{N}\sigma^{-2}_{c,d}}\right]\epsilon_\ell\right] \tag{C.102}$$

$$+ \sum_{k=1}^{N-1}\sum_{\ell=1}^{N-1}\left[\epsilon_k\left[\frac{\sum_{j=1}^{N}\sum_{a=1}^{N}\sum_{i=k+1}^{N}\sum_{b=\ell+1}^{N}\left(\sigma^{-2}_{a,j}\sigma^{-2}_{b,i} - \sigma^{-2}_{i,j}\sigma^{-2}_{a,b}\right)}{\sum_{c=1}^{N}\sum_{d=1}^{N}\sigma^{-2}_{c,d}}\right]\epsilon_\ell\right] \tag{C.103}$$

$$- \sum_{k=2}^{N}\sum_{\ell=1}^{N-1}\left[\epsilon_k\left[\frac{\sum_{j=1}^{N}\sum_{a=1}^{N}\sum_{i=k}^{N}\sum_{b=\ell+1}^{N}\left(\sigma^{-2}_{a,j}\sigma^{-2}_{b,i} - \sigma^{-2}_{i,j}\sigma^{-2}_{a,b}\right)}{\sum_{c=1}^{N}\sum_{d=1}^{N}\sigma^{-2}_{c,d}}\right]\epsilon_\ell\right] \tag{C.104}$$

$$- \sum_{k=1}^{N-1}\sum_{\ell=2}^{N}\left[\epsilon_k\left[\frac{\sum_{j=1}^{N}\sum_{a=1}^{N}\sum_{i=k+1}^{N}\sum_{b=\ell}^{N}\left(\sigma^{-2}_{a,j}\sigma^{-2}_{b,i} - \sigma^{-2}_{i,j}\sigma^{-2}_{a,b}\right)}{\sum_{c=1}^{N}\sum_{d=1}^{N}\sigma^{-2}_{c,d}}\right]\epsilon_\ell\right] \tag{C.105}$$

$$\tag{C.106}$$

We can now rearrange this sum to uncover the issues we need to fix. In all four lines, there is a common sum over j and over a, which we will pull out. Additionally, we will pull out the common denominator.

$$\tilde{\chi}^2(\vec{\alpha}) = \frac{1}{\sum_{c=1}^{N}\sum_{d=1}^{N}\sigma_{c,d}^{-2}}\sum_{j=1}^{N}\sum_{a=1}^{N}\left\{\sum_{k=2}^{N}\sum_{\ell=2}^{N}\left[\epsilon_k\epsilon_\ell\sum_{i=k}^{N}\sum_{b=\ell}^{N}\left(\sigma_{a,j}^{-2}\sigma_{b,i}^{-2}-\sigma_{i,j}^{-2}\sigma_{a,b}^{-2}\right)\right]\right. \tag{C.107}$$

$$+\sum_{k=1}^{N-1}\sum_{\ell=1}^{N-1}\left[\epsilon_k\epsilon_\ell\sum_{i=k+1}^{N}\sum_{b=\ell+1}^{N}\left(\sigma_{a,j}^{-2}\sigma_{b,i}^{-2}-\sigma_{i,j}^{-2}\sigma_{a,b}^{-2}\right)\right] \tag{C.108}$$

$$-\sum_{k=2}^{N}\sum_{\ell=1}^{N-1}\left[\epsilon_k\epsilon_\ell\sum_{i=k}^{N}\sum_{b=\ell+1}^{N}\left(\sigma_{a,j}^{-2}\sigma_{b,i}^{-2}-\sigma_{i,j}^{-2}\sigma_{a,b}^{-2}\right)\right] \tag{C.109}$$

$$\left.-\sum_{k=1}^{N-1}\sum_{\ell=2}^{N}\left[\epsilon_k\epsilon_\ell\sum_{i=k+1}^{N}\sum_{b=\ell}^{N}\left(\sigma_{a,j}^{-2}\sigma_{b,i}^{-2}-\sigma_{i,j}^{-2}\sigma_{a,b}^{-2}\right)\right]\right\} \tag{C.110}$$

We now begin the arduous process of simplifying this. First, we simplify the sums over k by splitting them into the part from 2 to N, and the leftover.

$$\tilde{\chi}^2(\vec{\alpha}) = \frac{1}{\sum_{c=1}^{N}\sum_{d=1}^{N}\sigma_{c,d}^{-2}}\sum_{j=1}^{N}\sum_{a=1}^{N} \tag{C.111}$$

$$\left\{\sum_{k=2}^{N-1}\sum_{\ell=2}^{N}\left[\epsilon_k\epsilon_\ell\sum_{i=k}^{N}\sum_{b=\ell}^{N}\left(\sigma_{a,j}^{-2}\sigma_{b,i}^{-2}-\sigma_{i,j}^{-2}\sigma_{a,b}^{-2}\right)\right]+\sum_{\ell=2}^{N}\left[\epsilon_N\epsilon_\ell\sum_{i=N}^{N}\sum_{b=\ell}^{N}\left(\sigma_{a,j}^{-2}\sigma_{b,i}^{-2}-\sigma_{i,j}^{-2}\sigma_{a,b}^{-2}\right)\right]\right. \tag{C.112}$$

$$+\sum_{k=2}^{N-1}\sum_{\ell=1}^{N-1}\left[\epsilon_k\epsilon_\ell\sum_{i=k+1}^{N}\sum_{b=\ell+1}^{N}\left(\sigma_{a,j}^{-2}\sigma_{b,i}^{-2}-\sigma_{i,j}^{-2}\sigma_{a,b}^{-2}\right)\right]+\sum_{\ell=1}^{N-1}\left[\epsilon_1\epsilon_\ell\sum_{i=2}^{N}\sum_{b=\ell+1}^{N}\left(\sigma_{a,j}^{-2}\sigma_{b,i}^{-2}-\sigma_{i,j}^{-2}\sigma_{a,b}^{-2}\right)\right] \tag{C.113}$$

$$-\sum_{k=2}^{N-1}\sum_{\ell=1}^{N-1}\left[\epsilon_k\epsilon_\ell\sum_{i=k}^{N}\sum_{b=\ell+1}^{N}\left(\sigma_{a,j}^{-2}\sigma_{b,i}^{-2}-\sigma_{i,j}^{-2}\sigma_{a,b}^{-2}\right)\right]-\sum_{\ell=1}^{N-1}\left[\epsilon_N\epsilon_\ell\sum_{i=N}^{N}\sum_{b=\ell+1}^{N}\left(\sigma_{a,j}^{-2}\sigma_{b,i}^{-2}-\sigma_{i,j}^{-2}\sigma_{a,b}^{-2}\right)\right] \tag{C.114}$$

$$\left.-\sum_{k=2}^{N-1}\sum_{\ell=2}^{N}\left[\epsilon_k\epsilon_\ell\sum_{i=k+1}^{N}\sum_{b=\ell}^{N}\left(\sigma_{a,j}^{-2}\sigma_{b,i}^{-2}-\sigma_{i,j}^{-2}\sigma_{a,b}^{-2}\right)\right]-\sum_{\ell=2}^{N}\left[\epsilon_1\epsilon_\ell\sum_{i=2}^{N}\sum_{b=\ell}^{N}\left(\sigma_{a,j}^{-2}\sigma_{b,i}^{-2}-\sigma_{i,j}^{-2}\sigma_{a,b}^{-2}\right)\right]\right\} \tag{C.115}$$

We can do the same with ℓ.

$$\tilde{\chi}^2(\vec{\alpha}) = \frac{1}{\sum_{c=1}^{N}\sum_{d=1}^{N}\sigma_{c,d}^{-2}}\sum_{j=1}^{N}\sum_{a=1}^{N}\{ \tag{C.116}$$

$$\sum_{k=2}^{N-1}\sum_{\ell=2}^{N-1}\left[\epsilon_k\epsilon_\ell\sum_{i=k}^{N}\sum_{b=\ell}^{N}\left(\sigma_{a,j}^{-2}\sigma_{b,i}^{-2}-\sigma_{i,j}^{-2}\sigma_{a,b}^{-2}\right)\right]+\sum_{\ell=2}^{N-1}\left[\epsilon_N\epsilon_\ell\sum_{i=N}^{N}\sum_{b=\ell}^{N}\left(\sigma_{a,j}^{-2}\sigma_{b,i}^{-2}-\sigma_{i,j}^{-2}\sigma_{a,b}^{-2}\right)\right] \tag{C.117}$$

$$+\sum_{k=2}^{N-1}\left[\epsilon_k\epsilon_N\sum_{i=k}^{N}\sum_{b=N}^{N}\left(\sigma_{a,j}^{-2}\sigma_{b,i}^{-2}-\sigma_{i,j}^{-2}\sigma_{a,b}^{-2}\right)\right]+\left[\epsilon_N\epsilon_N\sum_{i=N}^{N}\sum_{b=N}^{N}\left(\sigma_{a,j}^{-2}\sigma_{b,i}^{-2}-\sigma_{i,j}^{-2}\sigma_{a,b}^{-2}\right)\right] \tag{C.118}$$

$$+\sum_{k=2}^{N-1}\sum_{\ell=2}^{N-1}\left[\epsilon_k\epsilon_\ell\sum_{i=k+1}^{N}\sum_{b=\ell+1}^{N}\left(\sigma_{a,j}^{-2}\sigma_{b,i}^{-2}-\sigma_{i,j}^{-2}\sigma_{a,b}^{-2}\right)\right]+\sum_{\ell=2}^{N-1}\left[\epsilon_1\epsilon_\ell\sum_{i=2}^{N}\sum_{b=\ell+1}^{N}\left(\sigma_{a,j}^{-2}\sigma_{b,i}^{-2}-\sigma_{i,j}^{-2}\sigma_{a,b}^{-2}\right)\right] \tag{C.119}$$

$$+\sum_{k=2}^{N-1}\left[\epsilon_k\epsilon_1\sum_{i=k+1}^{N}\sum_{b=2}^{N}\left(\sigma_{a,j}^{-2}\sigma_{b,i}^{-2}-\sigma_{i,j}^{-2}\sigma_{a,b}^{-2}\right)\right]+\left[\epsilon_1\epsilon_1\sum_{i=2}^{N}\sum_{b=2}^{N}\left(\sigma_{a,j}^{-2}\sigma_{b,i}^{-2}-\sigma_{i,j}^{-2}\sigma_{a,b}^{-2}\right)\right] \tag{C.120}$$

$$-\sum_{k=2}^{N-1}\sum_{\ell=2}^{N-1}\left[\epsilon_k\epsilon_\ell\sum_{i=k}^{N}\sum_{b=\ell+1}^{N}\left(\sigma_{a,j}^{-2}\sigma_{b,i}^{-2}-\sigma_{i,j}^{-2}\sigma_{a,b}^{-2}\right)\right]-\sum_{\ell=2}^{N-1}\left[\epsilon_N\epsilon_\ell\sum_{i=N}^{N}\sum_{b=\ell+1}^{N}\left(\sigma_{a,j}^{-2}\sigma_{b,i}^{-2}-\sigma_{i,j}^{-2}\sigma_{a,b}^{-2}\right)\right] \tag{C.121}$$

$$-\sum_{k=2}^{N-1}\left[\epsilon_k\epsilon_1\sum_{i=k}^{N}\sum_{b=2}^{N}\left(\sigma_{a,j}^{-2}\sigma_{b,i}^{-2}-\sigma_{i,j}^{-2}\sigma_{a,b}^{-2}\right)\right]-\left[\epsilon_N\epsilon_1\sum_{i=N}^{N}\sum_{b=2}^{N}\left(\sigma_{a,j}^{-2}\sigma_{b,i}^{-2}-\sigma_{i,j}^{-2}\sigma_{a,b}^{-2}\right)\right] \tag{C.122}$$

$$-\sum_{k=2}^{N-1}\sum_{\ell=2}^{N-1}\left[\epsilon_k\epsilon_\ell\sum_{i=k+1}^{N}\sum_{b=\ell}^{N}\left(\sigma_{a,j}^{-2}\sigma_{b,i}^{-2}-\sigma_{i,j}^{-2}\sigma_{a,b}^{-2}\right)\right]-\sum_{\ell=2}^{N-1}\left[\epsilon_1\epsilon_\ell\sum_{i=2}^{N}\sum_{b=\ell}^{N}\left(\sigma_{a,j}^{-2}\sigma_{b,i}^{-2}-\sigma_{i,j}^{-2}\sigma_{a,b}^{-2}\right)\right] \tag{C.123}$$

$$-\sum_{k=2}^{N-1}\left[\epsilon_k\epsilon_N\sum_{i=k+1}^{N}\sum_{b=N}^{N}\left(\sigma_{a,j}^{-2}\sigma_{b,i}^{-2}-\sigma_{i,j}^{-2}\sigma_{a,b}^{-2}\right)\right]-\left[\epsilon_1\epsilon_N\sum_{i=2}^{N}\sum_{b=N}^{N}\left(\sigma_{a,j}^{-2}\sigma_{b,i}^{-2}-\sigma_{i,j}^{-2}\sigma_{a,b}^{-2}\right)\right]\Bigg\} \tag{C.124}$$

We can now begin to do some pairwise cancellations, since sums over k and ℓ are universal. For example, the first term of the first line (Eqn. C.117) and the first term of the fifth line (Eqn. C.121) almost perfectly cancel, except for the difference in the sum over b. These observations allow us to make some great simplifications. We will leave some trivial sums in (for example, like the sums from N to N) to make it easier to compare steps, and we will simplify them later.

$$\tilde{\chi}^2(\vec{\alpha}) = \frac{1}{\sum_{c=1}^{N}\sum_{d=1}^{N}\sigma_{c,d}^{-2}}\sum_{j=1}^{N}\sum_{a=1}^{N}\{ \tag{C.125}$$

$$\sum_{k=2}^{N-1}\sum_{\ell=2}^{N-1}\left[\epsilon_k\epsilon_\ell\sum_{i=k}^{k}\sum_{b=\ell}^{\ell}\left(\sigma_{a,j}^{-2}\sigma_{b,i}^{-2}-\sigma_{i,j}^{-2}\sigma_{a,b}^{-2}\right)\right]+\sum_{\ell=2}^{N-1}\left[\epsilon_N\epsilon_\ell\sum_{i=N}^{N}\sum_{b=\ell}^{\ell}\left(\sigma_{a,j}^{-2}\sigma_{b,i}^{-2}-\sigma_{i,j}^{-2}\sigma_{a,b}^{-2}\right)\right] \tag{C.126}$$

$$+\sum_{k=2}^{N-1}\left[\epsilon_k\epsilon_N\sum_{i=N}^{N}\sum_{b=N}^{N}\left(\sigma_{a,j}^{-2}\sigma_{b,i}^{-2}-\sigma_{i,j}^{-2}\sigma_{a,b}^{-2}\right)\right]+\left[\epsilon_N\epsilon_N\sum_{i=N}^{N}\sum_{b=N}^{N}\left(\sigma_{a,j}^{-2}\sigma_{b,i}^{-2}-\sigma_{i,j}^{-2}\sigma_{a,b}^{-2}\right)\right] \tag{C.127}$$

$$-\sum_{\ell=2}^{N-1}\left[\epsilon_1\epsilon_\ell\sum_{i=2}^{N}\sum_{b=\ell}^{\ell}\left(\sigma_{a,j}^{-2}\sigma_{b,i}^{-2}-\sigma_{i,j}^{-2}\sigma_{a,b}^{-2}\right)\right] \tag{C.128}$$

$$-\sum_{k=2}^{N-1}\left[\epsilon_k\epsilon_1\sum_{i=k}^{k}\sum_{b=2}^{N}\left(\sigma_{a,j}^{-2}\sigma_{b,i}^{-2}-\sigma_{i,j}^{-2}\sigma_{a,b}^{-2}\right)\right]+\left[\epsilon_1\epsilon_1\sum_{i=2}^{N}\sum_{b=2}^{N}\left(\sigma_{a,j}^{-2}\sigma_{b,i}^{-2}-\sigma_{i,j}^{-2}\sigma_{a,b}^{-2}\right)\right] \tag{C.129}$$

$$-\left[\epsilon_N\epsilon_1\sum_{i=N}^{N}\sum_{b=2}^{N}\left(\sigma_{a,j}^{-2}\sigma_{b,i}^{-2}-\sigma_{i,j}^{-2}\sigma_{a,b}^{-2}\right)\right] \tag{C.130}$$

$$-\left[\epsilon_1\epsilon_N\sum_{i=2}^{N}\sum_{b=N}^{N}\left(\sigma_{a,j}^{-2}\sigma_{b,i}^{-2}-\sigma_{i,j}^{-2}\sigma_{a,b}^{-2}\right)\right]\Bigg\} \tag{C.131}$$

We can now begin recombining terms. For example, we can combine the two terms in the first row (Eqn. C.126) and expand the k sum to be from 2 to N. We can combine the two terms in the second row (Eqn. C.127) to also expand the sum over k from 2 to N, and then combine all these terms to expand the ℓ sum from 2 to N.

$$\tilde{\chi}^2(\vec{\alpha}) = \frac{1}{\sum_{c=1}^{N}\sum_{d=1}^{N}\sigma_{c,d}^{-2}}\sum_{j=1}^{N}\sum_{a=1}^{N}\{ \tag{C.132}$$

$$\sum_{k=2}^{N}\sum_{\ell=2}^{N}\left[\epsilon_k\epsilon_\ell\sum_{i=k}^{k}\sum_{b=\ell}^{\ell}\left(\sigma_{a,j}^{-2}\sigma_{b,i}^{-2}-\sigma_{i,j}^{-2}\sigma_{a,b}^{-2}\right)\right] \tag{C.133}$$

$$-\sum_{\ell=2}^{N}\left[\epsilon_1\epsilon_\ell\sum_{i=2}^{N}\sum_{b=\ell}^{\ell}\left(\sigma_{a,j}^{-2}\sigma_{b,i}^{-2}-\sigma_{i,j}^{-2}\sigma_{a,b}^{-2}\right)\right] \tag{C.134}$$

$$-\sum_{k=2}^{N}\left[\epsilon_k\epsilon_1\sum_{i=k}^{k}\sum_{b=2}^{N}\left(\sigma_{a,j}^{-2}\sigma_{b,i}^{-2}-\sigma_{i,j}^{-2}\sigma_{a,b}^{-2}\right)\right]+\left[\epsilon_1\epsilon_1\sum_{i=2}^{N}\sum_{b=2}^{N}\left(\sigma_{a,j}^{-2}\sigma_{b,i}^{-2}-\sigma_{i,j}^{-2}\sigma_{a,b}^{-2}\right)\right]\Bigg\} \tag{C.135}$$

The first row (Eqn. C.133) is a term we want, except we need to expand the sums over k and ℓ to go from 1, not 2. Let us add and subtract what we need to get there, first with k.

$$\tilde{\chi}^2(\vec{\alpha}) = \frac{1}{\sum_{c=1}^{N}\sum_{d=1}^{N}\sigma_{c,d}^{-2}}\sum_{j=1}^{N}\sum_{a=1}^{N}\{ \tag{C.136}$$

$$\sum_{k=1}^{N}\sum_{\ell=2}^{N}\left[\epsilon_k\epsilon_\ell\sum_{i=k}^{k}\sum_{b=\ell}^{\ell}\left(\sigma_{a,j}^{-2}\sigma_{b,i}^{-2}-\sigma_{i,j}^{-2}\sigma_{a,b}^{-2}\right)\right]-\sum_{\ell=2}^{N}\left[\epsilon_1\epsilon_\ell\sum_{i=1}^{1}\sum_{b=\ell}^{\ell}\left(\sigma_{a,j}^{-2}\sigma_{b,i}^{-2}-\sigma_{i,j}^{-2}\sigma_{a,b}^{-2}\right)\right] \tag{C.137}$$

$$-\sum_{\ell=2}^{N}\left[\epsilon_1\epsilon_\ell\sum_{i=2}^{N}\sum_{b=\ell}^{\ell}\left(\sigma_{a,j}^{-2}\sigma_{b,i}^{-2}-\sigma_{i,j}^{-2}\sigma_{a,b}^{-2}\right)\right] \tag{C.138}$$

$$-\sum_{k=2}^{N}\left[\epsilon_k\epsilon_1\sum_{i=k}^{k}\sum_{b=2}^{N}\left(\sigma_{a,j}^{-2}\sigma_{b,i}^{-2}-\sigma_{i,j}^{-2}\sigma_{a,b}^{-2}\right)\right]+\left[\epsilon_1\epsilon_1\sum_{i=2}^{N}\sum_{b=2}^{N}\left(\sigma_{a,j}^{-2}\sigma_{b,i}^{-2}-\sigma_{i,j}^{-2}\sigma_{a,b}^{-2}\right)\right]\Bigg\} \tag{C.139}$$

We see this residual subtraction on the first row (Eqn. C.137) combines with the second row (Eqn. C.138), expanding the sum over i to go from 1 to N.

$$\tilde{\chi}^2(\vec{\alpha}) = \frac{1}{\sum_{c=1}^{N}\sum_{d=1}^{N}\sigma_{c,d}^{-2}}\sum_{j=1}^{N}\sum_{a=1}^{N}\{ \tag{C.140}$$

$$\sum_{k=1}^{N}\sum_{\ell=2}^{N}\left[\epsilon_k\epsilon_\ell\sum_{i=k}^{k}\sum_{b=\ell}^{\ell}\left(\sigma_{a,j}^{-2}\sigma_{b,i}^{-2}-\sigma_{i,j}^{-2}\sigma_{a,b}^{-2}\right)\right] \tag{C.141}$$

$$-\sum_{\ell=2}^{N}\left[\epsilon_1\epsilon_\ell\sum_{i=1}^{N}\sum_{b=\ell}^{\ell}\left(\sigma_{a,j}^{-2}\sigma_{b,i}^{-2}-\sigma_{i,j}^{-2}\sigma_{a,b}^{-2}\right)\right] \tag{C.142}$$

$$-\sum_{k=2}^{N}\left[\epsilon_k\epsilon_1\sum_{i=k}^{k}\sum_{b=2}^{N}\left(\sigma_{a,j}^{-2}\sigma_{b,i}^{-2}-\sigma_{i,j}^{-2}\sigma_{a,b}^{-2}\right)\right]+\left[\epsilon_1\epsilon_1\sum_{i=2}^{N}\sum_{b=2}^{N}\left(\sigma_{a,j}^{-2}\sigma_{b,i}^{-2}-\sigma_{i,j}^{-2}\sigma_{a,b}^{-2}\right)\right]\Bigg\} \tag{C.143}$$

We will take the hint and also expand the k sum in the bottom row (Eqn. C.143). We see the residual addition (since the term we are expanding comes in with a minus sign) can be combined with the sum over i in the second term in the same row (Eqn. C.143) to go from 1 to N.

$$\tilde{\chi}^2(\vec{\alpha}) = \frac{1}{\sum_{c=1}^{N}\sum_{d=1}^{N}\sigma_{c,d}^{-2}}\sum_{j=1}^{N}\sum_{a=1}^{N}\{ \tag{C.144}$$

$$\sum_{k=1}^{N}\sum_{\ell=2}^{N}\left[\epsilon_k\epsilon_\ell\sum_{i=k}^{k}\sum_{b=\ell}^{\ell}\left(\sigma_{a,j}^{-2}\sigma_{b,i}^{-2}-\sigma_{i,j}^{-2}\sigma_{a,b}^{-2}\right)\right] \tag{C.145}$$

$$-\sum_{\ell=2}^{N}\left[\epsilon_1\epsilon_\ell\sum_{i=1}^{N}\sum_{b=\ell}^{\ell}\left(\sigma_{a,j}^{-2}\sigma_{b,i}^{-2}-\sigma_{i,j}^{-2}\sigma_{a,b}^{-2}\right)\right] \tag{C.146}$$

$$-\sum_{k=1}^{N}\left[\epsilon_k\epsilon_1\sum_{i=k}^{k}\sum_{b=2}^{N}\left(\sigma_{a,j}^{-2}\sigma_{b,i}^{-2}-\sigma_{i,j}^{-2}\sigma_{a,b}^{-2}\right)\right]+\left[\epsilon_1\epsilon_1\sum_{i=1}^{N}\sum_{b=2}^{N}\left(\sigma_{a,j}^{-2}\sigma_{b,i}^{-2}-\sigma_{i,j}^{-2}\sigma_{a,b}^{-2}\right)\right]\Bigg\} \tag{C.147}$$

Let us now expand the sum over ℓ in the same way, first in the top row (Eqn. C.145)

$$\tilde{\chi}^2(\vec{\alpha}) = \frac{1}{\sum_{c=1}^{N}\sum_{d=1}^{N}\sigma_{c,d}^{-2}}\sum_{j=1}^{N}\sum_{a=1}^{N}\{ \tag{C.148}$$

$$\sum_{k=1}^{N}\sum_{\ell=1}^{N}\left[\epsilon_k\epsilon_\ell\sum_{i=k}^{k}\sum_{b=\ell}^{\ell}\left(\sigma_{a,j}^{-2}\sigma_{b,i}^{-2}-\sigma_{i,j}^{-2}\sigma_{a,b}^{-2}\right)\right]-\sum_{k=1}^{N}\left[\epsilon_k\epsilon_1\sum_{i=k}^{k}\sum_{b=1}^{1}\left(\sigma_{a,j}^{-2}\sigma_{b,i}^{-2}-\sigma_{i,j}^{-2}\sigma_{a,b}^{-2}\right)\right] \tag{C.149}$$

$$-\sum_{\ell=2}^{N}\left[\epsilon_1\epsilon_\ell\sum_{i=1}^{N}\sum_{b=\ell}^{\ell}\left(\sigma_{a,j}^{-2}\sigma_{b,i}^{-2}-\sigma_{i,j}^{-2}\sigma_{a,b}^{-2}\right)\right] \tag{C.150}$$

$$-\sum_{k=1}^{N}\left[\epsilon_k\epsilon_1\sum_{i=k}^{k}\sum_{b=2}^{N}\left(\sigma_{a,j}^{-2}\sigma_{b,i}^{-2}-\sigma_{i,j}^{-2}\sigma_{a,b}^{-2}\right)\right]+\left[\epsilon_1\epsilon_1\sum_{i=1}^{N}\sum_{b=2}^{N}\left(\sigma_{a,j}^{-2}\sigma_{b,i}^{-2}-\sigma_{i,j}^{-2}\sigma_{a,b}^{-2}\right)\right]\Bigg\} \tag{C.151}$$

This new term in the first row (Eqn. C.149) combines with the first term in the third row (Eqn. C.151) to expand the sum over b to go from 1 to N.

$$\tilde{\chi}^2(\vec{\alpha}) = \frac{1}{\sum_{c=1}^{N}\sum_{d=1}^{N}\sigma_{c,d}^{-2}}\sum_{j=1}^{N}\sum_{a=1}^{N}\{ \tag{C.152}$$

$$\sum_{k=1}^{N}\sum_{\ell=1}^{N}\left[\epsilon_k\epsilon_\ell\sum_{i=k}^{k}\sum_{b=\ell}^{\ell}\left(\sigma_{a,j}^{-2}\sigma_{b,i}^{-2}-\sigma_{i,j}^{-2}\sigma_{a,b}^{-2}\right)\right] \tag{C.153}$$

$$-\sum_{\ell=2}^{N}\left[\epsilon_1\epsilon_\ell\sum_{i=1}^{N}\sum_{b=\ell}^{\ell}\left(\sigma_{a,j}^{-2}\sigma_{b,i}^{-2}-\sigma_{i,j}^{-2}\sigma_{a,b}^{-2}\right)\right] \tag{C.154}$$

$$-\sum_{k=1}^{N}\left[\epsilon_k\epsilon_1\sum_{i=k}^{k}\sum_{b=1}^{N}\left(\sigma_{a,j}^{-2}\sigma_{b,i}^{-2}-\sigma_{i,j}^{-2}\sigma_{a,b}^{-2}\right)\right]+\left[\epsilon_1\epsilon_1\sum_{i=1}^{N}\sum_{b=2}^{N}\left(\sigma_{a,j}^{-2}\sigma_{b,i}^{-2}-\sigma_{i,j}^{-2}\sigma_{a,b}^{-2}\right)\right]\Bigg\} \tag{C.155}$$

We're so close! Let's expand the last remaining ℓ sum in the second row (Eqn. C.154) the same way.

$$\tilde{\chi}^2(\vec{\alpha}) = \frac{1}{\sum_{c=1}^{N}\sum_{d=1}^{N}\sigma_{c,d}^{-2}}\sum_{j=1}^{N}\sum_{a=1}^{N}\{ \tag{C.156}$$

$$\sum_{k=1}^{N}\sum_{\ell=1}^{N}\left[\epsilon_k\epsilon_\ell\sum_{i=k}^{k}\sum_{b=\ell}^{\ell}\left(\sigma_{a,j}^{-2}\sigma_{b,i}^{-2}-\sigma_{i,j}^{-2}\sigma_{a,b}^{-2}\right)\right] \tag{C.157}$$

$$-\sum_{\ell=1}^{N}\left[\epsilon_1\epsilon_\ell\sum_{i=1}^{N}\sum_{b=\ell}^{\ell}\left(\sigma_{a,j}^{-2}\sigma_{b,i}^{-2}-\sigma_{i,j}^{-2}\sigma_{a,b}^{-2}\right)\right]+\left[\epsilon_1\epsilon_1\sum_{i=1}^{N}\sum_{b=1}^{1}\left(\sigma_{a,j}^{-2}\sigma_{b,i}^{-2}-\sigma_{i,j}^{-2}\sigma_{a,b}^{-2}\right)\right] \tag{C.158}$$

$$-\sum_{k=1}^{N}\left[\epsilon_k\epsilon_1\sum_{i=k}^{k}\sum_{b=1}^{N}\left(\sigma_{a,j}^{-2}\sigma_{b,i}^{-2}-\sigma_{i,j}^{-2}\sigma_{a,b}^{-2}\right)\right]+\left[\epsilon_1\epsilon_1\sum_{i=1}^{N}\sum_{b=2}^{N}\left(\sigma_{a,j}^{-2}\sigma_{b,i}^{-2}-\sigma_{i,j}^{-2}\sigma_{a,b}^{-2}\right)\right]\Bigg\} \tag{C.159}$$

This new term, the second term in the second row (Eqn. C.158) combines with the second term in the third row (Eqn. C.159) to expand the sum over b to go from 1 to N.

$$\tilde{\chi}^2(\vec{\alpha}) = \frac{1}{\sum_{c=1}^{N}\sum_{d=1}^{N}\sigma_{c,d}^{-2}}\sum_{j=1}^{N}\sum_{a=1}^{N}\{ \tag{C.160}$$

$$\sum_{k=1}^{N}\sum_{\ell=1}^{N}\left[\epsilon_k\epsilon_\ell\sum_{i=k}^{k}\sum_{b=\ell}^{\ell}\left(\sigma_{a,j}^{-2}\sigma_{b,i}^{-2}-\sigma_{i,j}^{-2}\sigma_{a,b}^{-2}\right)\right] \tag{C.161}$$

$$-\sum_{\ell=1}^{N}\left[\epsilon_1\epsilon_\ell\sum_{i=1}^{N}\sum_{b=\ell}^{\ell}\left(\sigma_{a,j}^{-2}\sigma_{b,i}^{-2}-\sigma_{i,j}^{-2}\sigma_{a,b}^{-2}\right)\right] \tag{C.162}$$

$$-\sum_{k=1}^{N}\left[\epsilon_k\epsilon_1\sum_{i=k}^{k}\sum_{b=1}^{N}\left(\sigma_{a,j}^{-2}\sigma_{b,i}^{-2}-\sigma_{i,j}^{-2}\sigma_{a,b}^{-2}\right)\right]+\left[\epsilon_1\epsilon_1\sum_{i=1}^{N}\sum_{b=1}^{N}\left(\sigma_{a,j}^{-2}\sigma_{b,i}^{-2}-\sigma_{i,j}^{-2}\sigma_{a,b}^{-2}\right)\right]\Bigg\} \tag{C.163}$$

At this point, we'll find it instructive to simplify all the "trivial" sums, for example, the sum $\sum_{i=k}^{k}$ in the first row (Eqn. C.161).

$$\tilde{\chi}^2(\vec{\alpha}) = \frac{1}{\sum_{c=1}^{N}\sum_{d=1}^{N}\sigma_{c,d}^{-2}}\sum_{j=1}^{N}\sum_{a=1}^{N}\{ \tag{C.164}$$

$$\sum_{k=1}^{N}\sum_{\ell=1}^{N}\left[\epsilon_k\epsilon_\ell\left(\sigma_{a,j}^{-2}\sigma_{\ell,k}^{-2}-\sigma_{k,j}^{-2}\sigma_{a,\ell}^{-2}\right)\right] \tag{C.165}$$

$$-\sum_{\ell=1}^{N}\left[\epsilon_1\epsilon_\ell\sum_{i=1}^{N}\left(\sigma_{a,j}^{-2}\sigma_{\ell,i}^{-2}-\sigma_{i,j}^{-2}\sigma_{a,\ell}^{-2}\right)\right] \tag{C.166}$$

$$-\sum_{k=1}^{N}\left[\epsilon_k\epsilon_1\sum_{b=1}^{N}\left(\sigma_{a,j}^{-2}\sigma_{b,k}^{-2}-\sigma_{k,j}^{-2}\sigma_{a,b}^{-2}\right)\right]+\left[\epsilon_1\epsilon_1\sum_{i=1}^{N}\sum_{b=1}^{N}\left(\sigma_{a,j}^{-2}\sigma_{b,i}^{-2}-\sigma_{i,j}^{-2}\sigma_{a,b}^{-2}\right)\right]\Bigg\} \tag{C.167}$$

We're now at a point where splitting and recombining terms won't make a difference anymore. However, we can demonstrate that some terms vanish. Let us take a moment to pull out all of the summation signs.

$$\tilde{\chi}^2(\vec{\alpha}) = \frac{1}{\sum_{c=1}^{N}\sum_{d=1}^{N}\sigma_{c,d}^{-2}}\left\{\sum_{j=1}^{N}\sum_{a=1}^{N}\sum_{k=1}^{N}\sum_{\ell=1}^{N}\left[\epsilon_k\epsilon_\ell\left(\sigma_{a,j}^{-2}\sigma_{\ell,k}^{-2}-\sigma_{k,j}^{-2}\sigma_{a,\ell}^{-2}\right)\right]\right. \tag{C.168}$$

$$-\sum_{j=1}^{N}\sum_{a=1}^{N}\sum_{\ell=1}^{N}\sum_{i=1}^{N}\left[\epsilon_1\epsilon_\ell\left(\sigma_{a,j}^{-2}\sigma_{\ell,i}^{-2}-\sigma_{i,j}^{-2}\sigma_{a,\ell}^{-2}\right)\right] \tag{C.169}$$

$$-\sum_{j=1}^{N}\sum_{a=1}^{N}\sum_{b=1}^{N}\sum_{k=1}^{N}\left[\epsilon_k\epsilon_1\left(\sigma_{a,j}^{-2}\sigma_{b,k}^{-2}-\sigma_{k,j}^{-2}\sigma_{a,b}^{-2}\right)\right] \tag{C.170}$$

$$\left.+\sum_{j=1}^{N}\sum_{a=1}^{N}\sum_{i=1}^{N}\sum_{b=1}^{N}\left[\epsilon_1\epsilon_1\left(\sigma_{a,j}^{-2}\sigma_{b,i}^{-2}-\sigma_{i,j}^{-2}\sigma_{a,b}^{-2}\right)\right]\right\} \tag{C.171}$$

Since all sums go from 1 to N, we have the freedom to relabel indices as so desired to show terms cancel. For example, on the second term of row 2 (Eqn. C.169) inside the square brackets, we can interchange i and a and see the two terms cancel. Likewise, on the second term of row 3 (Eqn. C.170), we can interchange j and b. On row 4 (Eqn. C.171) , we can interchange a and i. We see, from this argument, that all but the first row (Eqn. C.168) cancels, giving us (finally!) a sane expression.

$$\tilde{\chi}^2(\vec{\alpha}) = \frac{1}{\sum_{c=1}^{N}\sum_{d=1}^{N}\sigma_{c,d}^{-2}}\sum_{j=1}^{N}\sum_{a=1}^{N}\sum_{k=1}^{N}\sum_{\ell=1}^{N}\left[\epsilon_k\epsilon_\ell\left(\sigma_{a,j}^{-2}\sigma_{\ell,k}^{-2}-\sigma_{k,j}^{-2}\sigma_{a,\ell}^{-2}\right)\right] \tag{C.172}$$

To further simplify this expression, we need to distribute the sums over the innermost terms of Eqn. C.172.

$$\tilde{\chi}^2(\vec{\alpha}) = \frac{\sum_{j=1}^{N}\sum_{a=1}^{N}\sum_{k=1}^{N}\sum_{\ell=1}^{N}\left(\epsilon_k\epsilon_\ell\sigma_{a,j}^{-2}\sigma_{\ell,k}^{-2}\right) - \sum_{j=1}^{N}\sum_{a=1}^{N}\sum_{k=1}^{N}\sum_{\ell=1}^{N}\left(\epsilon_k\epsilon_\ell\sigma_{k,j}^{-2}\sigma_{a,\ell}^{-2}\right)}{\sum_{c=1}^{N}\sum_{d=1}^{N}\sigma_{c,d}^{-2}} \tag{C.173}$$

$$= \frac{\left(\sum_{j=1}^{N}\sum_{a=1}^{N}\sigma_{a,j}^{-2}\right)\left(\sum_{k=1}^{N}\sum_{\ell=1}^{N}\epsilon_k\epsilon_\ell\sigma_{\ell,k}^{-2}\right) - \left(\sum_{j=1}^{N}\sum_{k=1}^{N}\epsilon_k\sigma_{k,j}^{-2}\right)^2}{\sum_{c=1}^{N}\sum_{d=1}^{N}\sigma_{c,d}^{-2}} \tag{C.174}$$

$$= \sum_{k=1}^{N}\sum_{\ell=1}^{N}\epsilon_k\epsilon_\ell\sigma_{\ell,k}^{-2} - \frac{\left(\sum_{j=1}^{N}\sum_{k=1}^{N}\epsilon_k\sigma_{k,j}^{-2}\right)^2}{\sum_{c=1}^{N}\sum_{d=1}^{N}\sigma_{c,d}^{-2}} \tag{C.175}$$

$$= \sum_{k=1}^{N}\sum_{\ell=1}^{N}\left[y_k - f(\vec{\alpha};t_k)\right]\sigma_{k,\ell}^{-2}\left[y_\ell - f(\vec{\alpha};t_\ell)\right] - \frac{\left(\sum_{j=1}^{N}\sum_{k=1}^{N}\left[y_k - f(\vec{\alpha};t_k)\right]\sigma_{k,j}^{-2}\right)^2}{\sum_{c=1}^{N}\sum_{d=1}^{N}\sigma_{c,d}^{-2}} \tag{C.176}$$

Where on the last line we have reproduced Eqn. C.82.

Bibliography

List of Abbreviated Journal Titles

AIP Conf.Proc.	AIP Conference Proceedings
Ann.Rev.Nucl.Part.Sci.	Annual Review of Nuclear and Particle Science
Annals Phys.	Annals of Physics
Commun.Math.Phys.	Communications in Mathematical Physics
Comput.Phys.Commun.	Computer Physics Communications
Eur.Phys.J.	European Physical Journal
Int.J.Mod.Phys.	International Journal of Modern Physics
JHEP	Journal of High Energy Physics
N J.Phys.	New Journal of Physics
Nucl.Phys.	Nuclear Physics
Phys.Lett.	Physics Letters
Phys.Rept.	Physics Reports
Phys.Rev.	Physical Review Letters
PoS	Proceedings of Science
Rev.Math.Phys.	Reviews in Mathematical Physics
Rev.Mod.Phys	Reviews of Modern Physics

[1] G. Aad *et al.* (ATLAS Collaboration), Phys.Lett. **B716**, 1 (2012), arXiv:1207.7214 [hep-ex] .

[2] S. Chatrchyan *et al.* (CMS Collaboration), Phys.Lett. **B716**, 30 (2012), arXiv:1207.7235 [hep-ex] .

[3] L. Canetti, M. Drewes, and M. Shaposhnikov, New J.Phys. **14**, 095012 (2012), arXiv:1204.4186 [hep-ph] .

[4] M. Frasca, Int.J.Mod.Phys. **A22**, 2433 (2007), arXiv:hep-th/0611276 [hep-th] .

[5] H. Neuberger, U. M. Heller, M. Klomfass, and P. M. Vranas, AIP Conf.Proc. **272**, 1360 (1992), arXiv:hep-lat/9208017 [hep-lat] .

[6] J.-L. Gervais and B. Sakita, Nucl.Phys. **B34**, 632 (1971).

[7] J. Wess and B. Zumino, Nucl.Phys. **B70**, 39 (1974).

[8] N. Arkani-Hamed, A. G. Cohen, and H. Georgi, Phys.Lett. **B513**, 232 (2001), arXiv:hep-ph/0105239 [hep-ph] .

[9] N. Arkani-Hamed, A. Cohen, E. Katz, and A. Nelson, JHEP **0207**, 034 (2002), arXiv:hep-ph/0206021 [hep-ph] .

[10] M. Schmaltz and D. Tucker-Smith, Ann.Rev.Nucl.Part.Sci. **55**, 229 (2005), arXiv:hep-ph/0502182 [hep-ph] .

[11] J. Bardeen, L. N. Cooper, and J. R. Schrieffer, Phys. Rev. **106**, 162 (1957).

[12] K. G. Wilson, Phys.Rev. **D10**, 2445 (1974).

[13] S. Weinberg, Phys.Rev. **D19**, 1277 (1979).

[14] L. Susskind, Phys.Rev. **D20**, 2619 (1979).

[15] S. Dimopoulos and L. Susskind, Nucl.Phys. **B155**, 237 (1979).

[16] E. Eichten and K. D. Lane, Phys.Lett. **B90**, 125 (1980).

[17] I. Caprini, G. Colangelo, and H. Leutwyler, Phys.Rev.Lett. **96**, 132001 (2006), arXiv:hep-ph/0512364 [hep-ph] .

[18] K. Yamawaki, M. Bando, and K.-i. Matumoto, Phys. Rev. Lett. **56**, 1335 (1986).

[19] T. Appelquist, J. Terning, and L. C. R. Wijewardhana, Phys. Rev. D **44**, 871 (1991).

[20] C. T. Hill and E. H. Simmons, Phys.Rept. **381**, 235 (2003), arXiv:hep-ph/0203079 [hep-ph] .

[21] W. E. Caswell, Phys.Rev.Lett. **33**, 244 (1974).

[22] T. Banks and A. Zaks, Nucl.Phys. **B196**, 189 (1982).

[23] Z. Fodor and C. Hoelbling, Rev.Mod.Phys. **84**, 449 (2012), arXiv:1203.4789 [hep-lat] .

[24] T. DeGrand, Y. Shamir, and B. Svetitsky, PoS **LATTICE2008**, 063 (2008), arXiv:0809.2953 [hep-lat] .

[25] T. DeGrand, Y. Shamir, and B. Svetitsky, Phys.Rev. **D83**, 074507 (2011), arXiv:1102.2843 [hep-lat] .

[26] L. Del Debbio, B. Lucini, C. Pica, A. Patella, A. Rago, *et al.*, (2013), arXiv:1311.5597 [hep-lat] .

[27] A. Hasenfratz, A. Cheng, G. Petropoulos, and D. Schaich, (2013), arXiv:1303.7129 [hep-lat] .

[28] T. Appelquist, G. Fleming, M. Lin, E. Neil, and D. Schaich, Phys.Rev. **D84**, 054501 (2011), arXiv:1106.2148 [hep-lat] .

[29] A. Hasenfratz, Phys.Rev.Lett. **108**, 061601 (2012), arXiv:1106.5293 [hep-lat] .

[30] Y. Aoki, T. Aoyama, M. Kurachi, T. Maskawa, K.-i. Nagai, *et al.*, Phys.Rev. **D86**, 054506 (2012), arXiv:1207.3060 [hep-lat] .

[31] T. DeGrand, Phys.Rev. **D84**, 116901 (2011), arXiv:1109.1237 [hep-lat] .

[32] A. Cheng, A. Hasenfratz, Y. Liu, G. Petropoulos, and D. Schaich, Phys.Rev. **D90**, 014509 (2014), arXiv:1401.0195 [hep-lat] .

[33] A. Cheng, A. Hasenfratz, Y. Liu, G. Petropoulos, and D. Schaich, JHEP **1405**, 137 (2014), arXiv:1404.0984 [hep-lat] .

[34] M. Lombardo, K. Miura, T. J. N. da Silva, and E. Pallante, (2014), arXiv:1410.0298 [hep-lat] .

[35] Y. Aoki, T. Aoyama, M. Kurachi, T. Maskawa, K.-i. Nagai, *et al.*, Phys.Rev.Lett. **111**, 162001 (2013), arXiv:1305.6006 [hep-lat] .

[36] Y. Aoki *et al.* (the LatKMI Collaboration), Phys.Rev. **D89**, 111502 (2014), arXiv:1403.5000 [hep-lat] .

[37] Z. Fodor, K. Holland, J. Kuti, D. Nogradi, and C. H. Wong, PoS **LATTICE2013**, 062 (2014), arXiv:1401.2176 [hep-lat] .

[38] J. Giedt and E. Weinberg, Phys.Rev. **D84**, 074501 (2011), arXiv:1105.0607 [hep-lat] .

[39] J. Rantaharju, PoS **Lattice2013**, 084 (2014), arXiv:1311.3719 [hep-lat] .

[40] J. Giedt and E. Weinberg, Phys.Rev. **D85**, 097503 (2012), arXiv:1201.6262 [hep-lat]

.

[41] F. Sannino and K. Tuominen, Phys.Rev. **D71**, 051901 (2005), arXiv:hep-ph/0405209 [hep-ph] .

[42] T. Appelquist *et al.*, Phys. Rev. Lett. **112**, 111601 (2014), arXiv:1311.4889 [hep-ph] .

[43] R. Brower *et al.* (LSD), Phys.Rev. **D90**, 014503 (2014), arXiv:1403.2761 [hep-lat] .

[44] T. Appelquist *et al.* (LSD), Phys.Rev. **D90**, 114502 (2014), arXiv:1405.4752 [hep-lat] .

[45] R. D. Ball and R. S. Thorne, Annals Phys. **241**, 368 (1995), arXiv:hep-th/9404156 [hep-th] .

[46] A. Grozin, Int.J.Mod.Phys. **A28**, 1350015 (2013), arXiv:1212.5144 [hep-ph] .

[47] A. Cheng, A. Hasenfratz, G. Petropoulos, and D. Schaich, JHEP **1307**, 061 (2013), arXiv:1301.1355 [hep-lat] .

[48] M. E. Peskin and T. Takeuchi, Phys.Rev.Lett. **65**, 964 (1990).

[49] F. Dyson, Phys.Rev. **75**, 1736 (1949).

[50] G. C. Wick, Phys. Rev. **96**, 1124 (1954).

[51] D. Schlingemann, Rev.Math.Phys. **11**, 1151 (1999), arXiv:hep-th/9802035 [hep-th] .

[52] M. Hasenbusch and S. Necco, JHEP **0408**, 005 (2004), arXiv:hep-lat/0405012 [hep-lat] .

[53] A. Cheng, A. Hasenfratz, G. Petropoulos, and D. Schaich, PoS **LATTICE2013**, 088 (2013), arXiv:1311.1287 [hep-lat] .

[54] H. B. Nielsen and M. Ninomiya, Phys.Lett. **B105**, 219 (1981).

[55] D. B. Kaplan, Phys.Lett. **B288**, 342 (1992), arXiv:hep-lat/9206013 [hep-lat] .

[56] H. Neuberger, Phys.Lett. **B417**, 141 (1998), arXiv:hep-lat/9707022 [hep-lat] .

[57] P. H. Ginsparg and K. G. Wilson, Phys.Rev. **D25**, 2649 (1982).

[58] S. Chandrasekharan, Phys.Rev. **D60**, 074503 (1999), arXiv:hep-lat/9805015 [hep-lat] .

[59] J. B. Kogut and L. Susskind, Phys.Rev. **D11**, 395 (1975).

[60] A. Hasenfratz, R. Hoffmann, and S. Schaefer, JHEP **0705**, 029 (2007), arXiv:hep-

lat/0702028 [hep-lat] .

[61] S. Duane, A. Kennedy, B. Pendleton, and D. Roweth, Phys.Lett. **B195**, 216 (1987).

[62] J. Osborn *et al.*, "Framework for unified evolution of lattices (FUEL)," .

[63] A. Pochinsky *et al.*, "Qlua," .

[64] R. Sommer, Nucl.Phys. **B411**, 839 (1994), arXiv:hep-lat/9310022 [hep-lat] .

[65] A. Gonzalez-Arroyo and M. Okawa, Phys.Lett. **B718**, 1524 (2013), arXiv:1206.0049 [hep-th] .

[66] M. Lüscher, JHEP **1008**, 071 (2010), arXiv:1006.4518 [hep-lat] .

[67] A. Ramos, (2015), arXiv:1506.00118 [hep-lat] .

[68] M. C, C. Consonni, G. P. Engel, and L. Giusti, (2015), arXiv:1506.06052 [hep-lat] .

[69] R. Narayanan and H. Neuberger, JHEP **0603**, 064 (2006), arXiv:hep-th/0601210 [hep-th] .

[70] M. Lüscher, Commun.Math.Phys. **293**, 899 (2010), arXiv:0907.5491 [hep-lat] .

[71] Z. Fodor, K. Holland, J. Kuti, D. Nogradi, and C. H. Wong, JHEP **1211**, 007 (2012), arXiv:1208.1051 [hep-lat] .

[72] R. Brower, A. Hasenfratz, C. Rebbi, E. Weinberg, and O. Witzel, (2014), arXiv:1411.3243 [hep-lat] .

[73] A. Hasenfratz, PoS **LATTICE2014**, 257 (2015), arXiv:1501.07848 [hep-lat] .

[74] A. Bazavov *et al.* (MILC), PoS **LATTICE2013**, 269 (2014), arXiv:1311.1474 [hep-lat] .

[75] R. Sommer, PoS **LATTICE2013**, 015 (2014), arXiv:1401.3270 [hep-lat] .

[76] S. Bethke, Eur.Phys.J. **C64**, 689 (2009), arXiv:0908.1135 [hep-ph] .

[77] M. Atiyah, N. J. Hitchin, V. Drinfeld, and Y. Manin, Phys.Lett. **A65**, 185 (1978).

[78] M. Atiyah and I. Singer, Annals Math. **93**, 139 (1971).

[79] A. S. Schwarz, Phys.Lett. **B67**, 172 (1977).

[80] R. Narayanan and H. Neuberger, Nucl.Phys. **B443**, 305 (1995), arXiv:hep-th/9411108 [hep-th] .

[81] M. Garcia Perez, O. Philipsen, and I.-O. Stamatescu, Nucl.Phys. **B551**, 293 (1999),

arXiv:hep-lat/9812006 [hep-lat] .

[82] M. Mller-Preussker, PoS **LATTICE2014**, 003 (2015), arXiv:1503.01254 [hep-lat] .

[83] S. O. Bilson-Thompson, D. B. Leinweber, and A. G. Williams, Annals Phys. **304**, 1 (2003), arXiv:hep-lat/0203008 [hep-lat] .

[84] G. Kilcup and S. R. Sharpe, Nucl.Phys. **B283**, 493 (1987).

[85] M. Peardon *et al.* (Hadron Spectrum), Phys.Rev. **D80**, 054506 (2009), arXiv:0905.2160 [hep-lat] .

[86] R. Gupta, G. Guralnik, G. W. Kilcup, and S. R. Sharpe, Phys.Rev. **D43**, 2003 (1991).

[87] M. Gell-Mann, R. Oakes, and B. Renner, Phys.Rev. **175**, 2195 (1968).

[88] T. Appelquist *et al.* (LSD), Phys.Rev.Lett. **104**, 071601 (2010), arXiv:0910.2224 [hep-ph] .

[89] J. Giedt and D. Howarth, (2014), arXiv:1405.4524 [hep-lat] .

[90] D. Schaich, A. Hasenfratz, and E. Rinaldi (LSD), (2015), arXiv:1506.08791 [hep-lat] .

[91] J. Foley, K. Jimmy Juge, A. O'Cais, M. Peardon, S. M. Ryan, *et al.*, Comput.Phys.Commun. **172**, 145 (2005), arXiv:hep-lat/0505023 [hep-lat] .

[92] M. E. Peskin and D. V. Schroeder, *An Introduction To Quantum Field Theory*, reprint ed. (Westview Press, 1995).

[93] U. Wolff (ALPHA), Comput.Phys.Commun. **156**, 143 (2004), arXiv:hep-lat/0306017 [hep-lat] .

[94] C. DeTar, "Physics 6730 Jackknife Error Estimates," .

[95] J. C. Lagarias, J. A. Reeds, M. H. Wright, and P. E. Wright, SIAM Journal of Optimization **9**, 112 (1998).

[96] Y. Aoki *et al.* (LatKMI), PoS **LATTICE2013**, 077 (2014), arXiv:1311.6885 [hep-lat] .

[97] O. Antipin, J. Krog, E. Mlgaard, and F. Sannino, JHEP **1309**, 122 (2013), arXiv:1303.7213 [hep-ph] .

[98] T. Appelquist *et al.* (LSD Collaboration), Phys.Rev.Lett. **106**, 231601 (2011),

arXiv:1009.5967 [hep-ph] .

[99] T. Appelquist *et al.*, (2015), arXiv:1503.04203 [hep-ph] .

[100] B. B. Brandt, A. Jttner, and H. Wittig, JHEP **1311**, 034 (2013), arXiv:1306.2916 [hep-lat] .

[101] M. F. Golterman and J. Smit, Nucl.Phys. **B255**, 328 (1985).

[102] C. J. Morningstar and M. J. Peardon, Phys.Rev. **D60**, 034509 (1999), arXiv:hep-lat/9901004 [hep-lat] .

[103] G. T. Fleming, , 143 (2004), arXiv:hep-lat/0403023 [hep-lat] .

[104] G. T. Fleming, S. D. Cohen, H.-W. Lin, and V. Pereyra, Phys.Rev. **D80**, 074506 (2009), arXiv:0903.2314 [hep-lat] .

[105] C. Heiles, "Least-Squares and Chi-Square for the budding aficionado: art and practice," .

[106] Y. Aoki, T. Aoyama, M. Kurachi, T. Maskawa, K.-i. Nagai, *et al.*, (2013), 10.1142/97898145662540009, arXiv:1302.4577 [hep-lat]

Evan Weinberg